StratoMAV

Final Report

DSE Group 11

H.R.J.W.M. Arts	1515381	A.A. Habiboella	4032845		
C.A. Broek	4017595	D.K. Konijnenberg	4004450	T. de Morée	4047338
T. Dikici	4018680	W. Koomen	4013083	N. Tanouti	4043561
K. de Groot	1306073	K. Lamers	1507338		

Design Synthesis Exercise

TU Delft Delft University of Technology

Faculty of Aerospace Engineering

Preface

This report is the final deliverable of the Design Synthesis Exercise of group 11: StratoMAV. The Design Synthesis Exercise is the final project of the bachelor of Aerospace Engineering at Delft University of Technology. During this project, the acquired knowledge of the bachelor programme has to be applied. The project objective is to design a Micro Aerial Vehicle (MAV), which is able to fly in the stratosphere with an extremely long duration. The UAV has to investigate the climate effects of aircraft contrails. Ten students have been working on this project for ten weeks in total.

As a first step of this exercise, a Project Plan was developed in which systems engineering tools were used to determine the required method for designing the UAV. The second step was to generate concepts for the UAV, which is described in the Baseline Report. Hereafter, the best concepts were further examined, to determine the best option for the mission. Also, an initial design of the most important subsystems was made to perform the mission. This can be found in the Midterm Report. The current report covers the final phase of the design, in which the final concept and all the subsystems are designed in more detail.

The report starts with the background research and preliminary analysis. The design of the aircraft with the aerodynamics and flight dynamics analysis are discussed in chapter 4. The structural analysis of StratoMAV is in chapter 5. Analysis and design of the payload to investigate contrails can be found in chapter 8. This chapter elaborates on how the contrails are measured and which sensors are needed. In chapter 7 is described how a lightweight power system is designed which can keep StratoMAV flying for a year. Finally, the support systems, such as the autopilot, telemetry and thermal control, can be found in chapter 10.

We would like to express our gratitude to our supervisor and coaches for assisting us throughout the project: Dr. Ir. C.C. de Visser, M. Percin, MSc and G. Tescione, MSc. We would also like to thank Prof. Dr. M. Menenti, Ir. H.M. Ruijsink, Dr. T. Vlemmix and Ir. B.T.C. Zandbergen for their valuable advice during the detailed design of the subsystems.

Abstract

Looking at the expected growth of global air traffic in the coming decades, there is an urgency to investigate the climate effects of aircraft contrails. With this knowledge effective environmental policies can be developed. For this mission, continuous local measurements on contrail light reflecting properties is required to compare with data from satellites, in situ measurements and lab experiments. The ever increasing capabilities of UAVs, their low cost, fast development times and flexible application possibilities make them an ideal platform to perform such scientific research.

The purpose of this project is to develop an eternal Micro Aerial Vehicle (MAV) that is able to perform stratospheric research on the regional influence of contrails on the ground surface temperature. By remaining airborne for a year, StratoMAV is able to take regular measurements on contrails. The collected data is downlinked in near real-time. StratoMAV is constrained to have a total mass of at most 5 kg, a lifetime of at least 5 years and a maximum unit price of €50,000.

The result is a low weight UAV with a high aspect ratio wing of 7 m span, which enables a low cruise speed of 18 m/s. A twin boom inverted V-tail is selected. A highly cambered, thin airfoil has been chosen to generate sufficient lift, as the air density is low in the stratosphere. The airframe mass is 16% of the total aircraft mass. A D-box is placed in the front 25% of the wing. It contains a single spar and is made out of composites to provide high stiffness resulting in a small deflection: a maximum vertical tip deflection of 0.35 m is reached during strong gusts. The aft section of the wing is composed of balsa wood ribs and the wing is covered in lightweight, transparent foil to fix the airfoil shape.

A single high efficiency custom tractor propeller (low rpm, fixed pitch) was chosen to operate in the low density conditions. It has a diameter of 0.87 m, is located mid-wing and is foldable to improve the gliding performance. A custom two-stage gearbox with aluminium spur gears with a ratio of 13.8 : 1 enables a low rpm. The required output power of the propulsion system during cruise is 35.8 W. Power is supplied by thin film solar cells and state-of-the-art lithium ion batteries with a specific energy density of 400 $\frac{Wh}{kg}$. Instead of sizing the batteries for the worst case scenario, the flight route was optimized by flying at different latitudes. As a result the batteries take up 44% of the total mass. The capacity of the battery decreases with increasing number of cycles performed by the battery. To ensure that this loss coincides with a month where less battery capacity is required to fly, the launch date is set in September at the equator.

A Paparazzi autopilot system is used, together with a modem and a 900 MHz patch antenna. A combination of active and passive thermal control is applied. The carried payload consists of four spectrometers, one thermal camera and a processor. Contrail detection is achieved by a pattern recognition algorithm on the data from the thermal camera. The radiation flux of contrails is determined by measuring the terrestrial radiation and radiation reflected by the contrails during day, and the terrestrial radiation during night. This measurements will be compared with irradiation data from the sun that is readily available, to investigate the effect on the ground temperature by the contrails.

Table of Contents

List of Symbols

List of Latin Symbols

Symbol	Description	Unit
A (Aircraft Design)	Aspect Ratio	-
A (Payload)	Area	sr
A_h	Aspect Ratio of Horizontal Tail	-
b	Wing Span	m
b_h	Horizontal Tail Span	m
BW	Bandwidth	Hz
c	Climb Rate	m/s
$\bar{c}$	Mean Aerodynamic Chord	m
C_{D_0}	Zero Lift Drag Coefficient	-
C_{L_α}	Lift Gradient	$1/rad$
$C_{L_{\alpha_h}}$	Lift gradient of Horizontal Tail	$1/rad$
$C_{L_{des}}$	Design Lift Coefficient	-
$C_{l_{max}}$	Maximum 2D Lift Coefficient	-
$C_{L_{max}}$	Maximum 3D Lift Coefficient	-
C_d	Drag Coefficient	-
C_l	2D Lift Coefficient	-
C_L	3D Lift Coefficient	-
c_{max}	Maximum Chord of Propeller Blade	m
c_r	Root Chord	m
c_t	Tip Chord	m
c_T	Thrust Coefficient	-
$\frac{c}{V}$	Climb Gradient	-
D (Aircraft Design)	Drag Force	N
D (Propulsion)	Propeller Diameter	m
d	Range	m
D_{ao}	Application Overhead Data	bit
D_{gr}	Ground Antenna Diameter	m
D_{pl}	Payload Data	bit

Symbol	Description	Unit
D_{ro}	Radio Overhead Data	bit
e (Aircraft Design)	Oswald Factor	-
e (Telemetry)	Relative Transmit Pointing Error	-
E (Power)	Energy	Wh
E (Structure)	Young's modulus	Pa
f	Frequency	Hz
G_r	Receiver Antenna Gain	dBi
G_t	Transmitter Antenna Gain	dBi
I	Section Moment of Inertia	m^4
I_{CC}	Core Current	A
I_{CCIO}	I/O Current	A
J	Advance Ratio	-
L (Aircraft Design)	Lift Force	N
L (Structure)	Buckling Column Length	m
L_{lr}	Receiver Cable Loss	dB
L_{lt}	Transmitter Cable Loss	dB
L_{pr}	Receiver Pointing Loss	dB
L_{pt}	Transmitter Pointing Loss	dB
L_a	Attenuation Loss	dB
l_h	Distance from Wing a.c.to Horizontal Tail a.c.	m
L_s	Free-space loss	dB
M	Mach number	-
m	Mass	kg
MAC	Mean Aerodynamic Chord	m
n	Rotational Speed	s^-1
p	Roll Rate	rad
P	Power	W
P (Propulsion)	Propeller Pitch	m
P (Telemetry)	Transmitter Power	W
q	Pitch Rate	rad
r (Aircraft Design)	Yaw Rate	rad
R (Propulsion)	Propeller Radius	m
r	Current Radial Position	m
rt	Retry Percentage	%
R (Payload)	Radius	rad
R (Telemetry)	Data Rate	$Kbps$
Re	Reynolds Number	-
S	Wing Surface Area	m^2
s_{land}	Landing Distance	m
S_h	Horizontal Tail Surface	m^2
S_v	Vertical Tail Surface	m^2
SNR	Signal to Noise Ratio	-
T	Thrust	N
T_s	System Noise Temperature	K
V_∞	Free Stream Velocity	m/s
V_a	Landing Speed	m/s
V_{CC}	Core Voltage	V

Symbol	Description	Unit
V_{CCIO}	I/O Voltage	V
V_{cruise}	Cruise Speed	m/s
V_s	Stall Speed	m/s
W	Weight	kg
x_{cg}	Center of Gravity	m
x_{np}	Neutral Point	m

List of Greek Symbols

Symbol	Description	Unit
α	Angle of Attack	rad
β (Aircraft Design)	Prandtl-Glauert Factor	-
β (Aircraft Design)	The angle of sideslip	rad
β (Power)	Inclination Angle	$^\circ$
Γ	Dihedral Angle	rad
γ	Azimuth Angle	$^\circ$
δ	Declination Angle	$^\circ$
ϵ	Wing Twist Angle	rad
$\frac{d\epsilon}{d\alpha}$	Downwash Gradient	-
η	Efficiency	-
η_p	Propeller Efficiency	-
θ (Aircraft Design)	Pitch Angle	rad
θ (Payload)	Half Angle	rad
θ (Power)	Solar Incidence Angle	$^\circ$
Λ	Sweep Angle	rad
λ	Taper Ratio	-
μ_∞	Absolute Viscosity Coefficient	Ns/m
ρ	Air Density	kg/m^3
ϕ (Aircraft Design)	Roll angle	rad
ϕ (Power)	Latitude	$^\circ$
ω (Payload)	Solid Angle	sr
ω (Power)	Hour Angle	$^\circ$

Chapter 1

Introduction

For years, one of the most important issues in science has been global warming. Researchers all over the world are trying to find out which phenomena cause global warming, and to which extent they do so [1]. Like every industrial sector that influences the climate, the aviation sector is a target of the global warming discussion [2]. When the terrorist attacks in the USA took place in 2001, commercial aviation was temporarily prohibited [44]. This created research possibilities, after which contradicting hypotheses about the influence of aviation started to emerge amongst climate researchers [45]. Some studies suggest that during these days, due to the absence of aviation and therefore aircraft contrails, surface temperatures at ground level fell. However, others stated that the temperature at ground level rose due to the absence of aircraft [3]. Ever since, the contrail influence on the climate has been a subject of discussion. Clarity on this subject is necessary, to check whether these effects can be used as a global climate control system or whether contrail coverage has to be prevented to reduce the effects of global warming.

The purpose of this report is to present the development of a Micro Aerial Vehicle (MAV) enabling stratospheric research on aircraft contrail influence on ground surface temperatures. The product should enable researchers to gather relevant scientific data and should continuously remain airborne in the stratosphere for at least a year. The product is constrained to have a mass of five kilograms maximum, have a lifetime of at least five years, and the unit cost price may not exceed €50,000.

The structure of the report is as follows. Chapter 2 discusses the background research, which is needed to fully understand what has to be measured. The preliminary analysis is described in chapter 3. Chapter 4 shows the design of the aircraft and discusses the stability, controllability and performance characteristics. Hereafter the payload design follows, described in chapter 8. The structure of the aircraft is elaborated upon in chapter 5. In chapter 6, the propulsion system is designed. Hereafter, the power system of the aircraft is described in chapter 7. The support systems of the aircraft are described in chapter 9, which are telemetry, autopilot, thermal control, ascend system and landing system. In chapter 10, the system overview is given. Finally, the design implementations are elaborated upon in chapter 11.

Chapter 2

Background Research

This chapter describes the environment in which StratoMAV will operate. The stratospheric properties are discussed and a short summary about contrails is given.

2.1 Stratosphere

One of the given requirements is that StratoMAV should fly at an altitude of at least 15 km, then it will be above commercial airspace. The stratosphere is situated between 15 km and 50 km. The conditions of the air in the stratosphere, compared to normal flight conditions, are unusual. The VITO (Flemish Institute for Technological Research) mentions that:

> The stratosphere is characterized by an almost complete lack of water vapour, relatively low wind speeds (10 m/s on average), only limited turbulence and low temperatures (-50 to $-70°C$). Air traffic is controlled up to 14 km altitude [4].

Additionally, it is mentioned that:

> The air in the stratosphere is very dry, generally having less than 0.05% of the maximum amount of water vapour found near the ground. Peak ozone concentration is found at about 25 km [46].

Stratospheric data have been used in the calculations throughout the design of StratoMAV. The highest wind speeds occur between 5 and 14 km, where the jet streams are present. At 15 km the average wind speed is 10 m/s [4] and the maximum wind speed about 30 m/s. Maximum gusts speed are 3.7 m/s at 15 km [5]. At the lower part of the stratosphere the air density is about a tenth of the ground level air density. At 15 km the air density is 0.192 kg/m^3. As expected, the solar irradiance is the highest in the summer months, which makes these months the best time to measure. In the summer the maximum solar energy in the Netherlands is about 5000 $Wh/m^2/day$ [4]. The temperature does not change a lot between 10 and 30 km from the average value of $-50°C$, but at night the temperature can drop to $-80°C$ around 15 km.

2.2 Contrails

Contrails are condensation trails consisting of ice particles. These ice particles and the contrails they form can be created in two ways, as described below. The difference lies in the origin of the water vapour, which turns into ice particles. [6]

- The first process starts when water vapour, present in the exhaust gases of aircraft and in the atmosphere, reaches the saturation point of the humidity of the air. The water vapour then condensates on the surrounding particles and turns into liquid drops. These drops rapidly freeze and form ice particles. The formation of liquid droplets and ice crystals, which become contrails, depends on the humidity, temperature and pressure of the surrounding air. Contrails evaporate quickly if the humidity is low, and are persistent if the humidity is high; they might even grow as surrounding water vapour freezes onto the ice particles. Furthermore, the contrails can spread out because of air turbulence and wind streams. They can have a height of 200 m to 400 m [6] and grow in width from 100 m to several kilometers [6] with spreading rates of $18 - 140$ m/min [7]. They can be as long as several dozen kilometres and persist for several hours. [6]
- The second process is caused by the pressure drop from an engine propeller or a wing. The pressure drop causes water vapour to condensate, freeze and turn into a contrail. The water vapour in this process consists only of atmospheric water. This means that these contrails only occur when the temperature is not too low and the humidity is high. These contrails are short trails, which disappear quickly. Because of meteorological variations, the temperature and humidity is not always right to form this kind of contrails. [6]

Contrails often evolve into cirrus clouds, especially the ones created by process 1, as they tend to evaporate less quickly. These cirrus clouds cannot be easily distinguished from naturally formed cirrus clouds. Natural cirrus clouds are thin clouds occurring typically above $6,000$ m [47]. F. Schroder [8] discusses the transition of contrails into cirrus clouds. The way to distinguish contrail cirrus clouds from natural cirrus clouds is explained in this paper. Contrails contain higher concentrations of near spherical ice crystals, with smaller mean diameters than the ice crystals found in natural cirrus clouds [8]. Over time, the ice crystals of persistent spreading contrails diffuse, such that they resemble natural cirrus clouds. Aside from containing different shaped ice crystals, contrails also contain aerosols (the most important ones being those composed of sulphate and soot [9]), compared to natural cirrus clouds.

The influence of aviation on the Earth's climate has been estimated to account for 3.5% of all human activities. This influence includes all factors of aviation, including contrails. Persistent line-shaped contrails were estimated to cover, on average, about 0.1% of the Earth's surface in 1992. [6] As these percentages are quite high, it seems worthwhile to investigate the relation between contrails and the temperature on Earth.

It can be concluded that contrails mainly exist out of ice particles, but also contain aerosols. In addition, the persistent contrails are of greater importance for the science mission than the short lived contrails. Induced cirrus clouds are also of importance, seeing that they evolve from persistent contrails. To ensure that StratoMAV is measuring the correct cirrus clouds, the induced cirrus cloud needs to be distinguished from natural cirrus clouds. Natural cirrus clouds can be distinguished from induced clouds based on their composition, size and shape of the ice particles present in the clouds.

Chapter 3

Preliminary Analysis

3.1 Functional Analysis

To perform its mission, StratoMAV must be able to fulfil certain functions. These functions must be described, before the design process can be started. Therefore, a functional analysis is carried out. Functional analysis is a crucial part of the systems engineering process since it is one of the primary techniques for establishing the completeness of all requirements. It is visualised using a Functional Breakdown Structure and a Functional Flow Diagram, which are discussed in this section.

3.1.1 Functional Breakdown Structure

The Functional Breakdown Structure (FBS) gives an overview of all the functions that need to be performed by the system. The FBS for StratoMAV is shown in appendix B.

To perform the mission, several sub-functions need to be fulfilled: Provide Electrical Power, Operations, Perform Flight, Navigation, Contrail Measurements and Provide Structural Integrity. These are described below.

- The UAV needs to provide **electrical power** to all subsystems. In order to do that, the electrical power must first be accumulated. The power then needs to be regulated and distributed. If necessary, excess generated power needs to be stored.
- StratoMAV needs to be externally accesible to its users using a **telemetry subsytem**. This is done by downlinking the science data and uplinking commands. Additionally, the system location and subsystems status (system health) needs to be monitored and communicated to the ground system, to verify whether the (sub)systems are still working properly.
- During the mission, the UAV should be able to perform **flight** segments of the mission profile. To satisfy this function, lift and thrust need to be generated. Furthermore, to perform manoeuvres, control surfaces need to generate lateral forces. Finally, the UAV should be dynamically stable to recover from any disturbances in the atmosphere.
- Measurements need to be taken at designated locations. This requires the ability to **navigate**. Navigation involves knowledge about the system's current location, altitude, speed and the mission destination. Once these are known, an optimal route in terms of energy can be calculated. The calculated route is communicated to the control system which then performs the flight towards the destination.

- The purpose of the mission is to take **measurements on contrails**. In order to do this, the system must be able to distinguish contrails from natural clouds, and find and track these contrails. Then, the radiation flux received from the Sun and the Earth can be measured. These measurements need to be processed and stored.
- The UAV should provide **structural integrity** to the (sub)systems. It also needs to be able to cope with external and internal loads to prevent subsystem damage. During flight, vibrations can occur which can influence the measurements taken by the sensors. Precautions should be taken to avoid this. Finally, thermal control and protection from the environment must be provided.
- The system should be able to house the **payload**. The structure should protect the payload from environmental influences, such as radiation. Each (sub)system works optimally at a certain temperature which thus needs to be regulated.

3.1.2 Functional Flow Diagram

A Functional Flow Diagram (FFD) describes the logical order of the functions a system must have. It shows all functions in blocks, connected by arrows. If functions are performed in parallel, an AND junction is shown; if only one of them is performed, an OR junction is drawn. The diagram is shown in appendix A, and is divided into two sections. The upper part shows the non-detailed mission profile. Everything below this part presents detailed descriptions of all the phases. Below, the different blocks in the diagram are discussed.

Pre-operational Inspection
The FFD starts with the mission profile (figure A.1), which shows the main tasks of the UAV. The diagram starts with the *Pre-operational Inspection*, in which first the systems are turned on. Next, the energy level is checked; if it is not sufficient, the UAV needs to accumulate energy, which can be done by the operators. If the energy level is sufficient, it is checked if all the subsystems are working properly. If not, they are repaired. When the subsystems are all working, the communication link with the ground station is checked. If it is broken, it will be repaired, and if it is working, the *Pre-operational Inspection* is nearly finished. In order to save energy, the payload is switched off at the end of the process, as they are not needed until the loiter phase.

Transport
In the next phase, the actual operations start. The first part of the operations phase is *Transport*. This only involves moving the UAV from its current location to the take-off position by another vehicle. During the entire operational phase, the UAV is required to receive and process uplink data. Hence, an AND junction is shown in the mission profile of the FFD (figure A.1).

Take-off
The next phase is *Take-off* (figure A.1). As the UAV is carried to cruise altitude by a balloon, take-off is defined as the moment it is disconnected from the balloon. Simultaneously, the propulsion system is initiated, and the control surfaces are checked and set to the take-off position. Next, the take-off procedures are started, the UAV detaches from the balloon, and finally it flies on its own.

Ascent
During the mission, the vehicle will need to ascend, which can occur many times (figure A.1). At the same moment, altitude, location and attitude are checked and transmitted to the ground station. Next, the energy level is checked; if not sufficient, the UAV goes into *Power Saving Mode*, which is described later on. If there is enough energy available, the UAV increases altitude. Hereafter, the process starts over.

Cruise
Again, like in the *Ascent* phase, the altitude, location and attitude are checked and transmitted. After

this, the energy level is checked and the UAV goes into *Power Saving Mode* if the energy level is not sufficient. When enough energy is stored, the UAV changes its location to the mission area. This is called *Cruise* (figure A.2), and it must be noted that the measurement systems will not be turned on during this phase. When needed and/or possible, the UAV accumulates energy during cruise. After the change of location, the three checks are performed again, in order to see if the UAV has reached its desired location.

Loiter
During the *Loiter* phase (figure A.2), the UAV collects its data. It first checks its energy level and if not sufficient, the UAV goes into *Power Saving Mode*. If the energy level is sufficient to perform the mission, it switches on its payload. Hereafter, the altitude, attitude and location are checked and transmitted. If the altitude or location are not in range, the payload is switched off and the UAV continues to the ascend, descend or cruise phase to go the preferred measurement area. If the attitude does not meet the requirements, the UAV changes attitude and performs checks. If all checks are performed correctly, the measurements are taken and the altitude and location data are logged. This data is communicated to the ground station and if necessary is stored.

Descend
The first part of the *Descent* phase is the same as in the *Ascent* phase. The difference is that after the energy check, there is a possibility to choose between further decreasing altitude or receiving clearance for landing, after which the UAV will prepare for landing.

Land
After the preparations for landing are completed in the descent phase, the UAV starts its *Land* phase (figure A.2). In this phase the control surfaces are set to the landing position, after which it lands at the desired location.

Maintenance
During the *Maintenance* phase (figure A.2), the UAV is serviced. This means that it needs to allow easy access to critical components.

Power Saving Mode
Power Saving Mode (figure A.2) is a phase that is needed during the mission, since the required flight time of 365 days is extremely long for a UAV. This phase is run by the navigation system. Firstly, the altitude, location and attitude are checked simultaneously and transmitted to the ground station. Next, the UAV changes to the most efficient flight path and flies along this path. During the flight, the UAV acquires energy from its power source. Next, the energy level is checked. If not sufficient, the same process is repeated. If the energy level is considered high enough, the UAV proceeds with its mission.

3.2 Sensitivity Analysis

In this section the Sensitivity Analysis of the StratoMAV mission is discussed. Firstly, the strategy for the analysis is unveiled (subsection 3.2.1). Next, the design space (subsection 3.2.2) listing the some important assumptions and important variables is given. Then some interesting results will be shown in subsection 3.2.3. Finally, conclusions are drawn in subsection 3.2.4.

3.2.1 Sensitivity Analysis Strategy

The design of StratoMAV revolves around keeping the weight as low as possible. The sensitivity analysis starts by estimating the lift, such that in the end the weight can be determined. The lift is calculated

using a combination of surface area, lift coefficient, aspect ratio and cruise speed (which will be varied in the analysis in section 3.2.2). From these parameters, the drag is deduced. After multiplying the drag by the flight speed, one obtains the cruise power requirement. Adding the estimated power need for other subsystems gives the total power requirement.

Now the total power need is known, the date and location of the mission can be determined. The date and location influence the total power available as they influence the number of daylight hours during which the energy of the sun can be harvested. The duration of the night indirectly dictates the amount of energy that has to be stored, such that a the aircraft can sustain flight when no solar power is available. Next, the required solar array area (and thus weight (W_{sa})) and battery weight (W_{bat}) can be determined.

The parameters that influence the lift, together with a load case, can be used to determine the airframe weight (W_{af}). A statistical relation for this is used, based on aspect ratio and surface area (equation 3.2). When the payload weight (W_{pay}) and all other weight components are added, the total weight (W_{tot}) can be derived (equation 3.1). If weight does not equal lift, the next iteration can be performed.

$$W_{tot} = W_{sa} + W_{bat} + W_{af} + W_{pay} \tag{3.1}$$

Figure 3.1 illustrates the relationships between the parameters. The analysis starts at the lift (indicated in green) and gives an initial estimate of the weight.

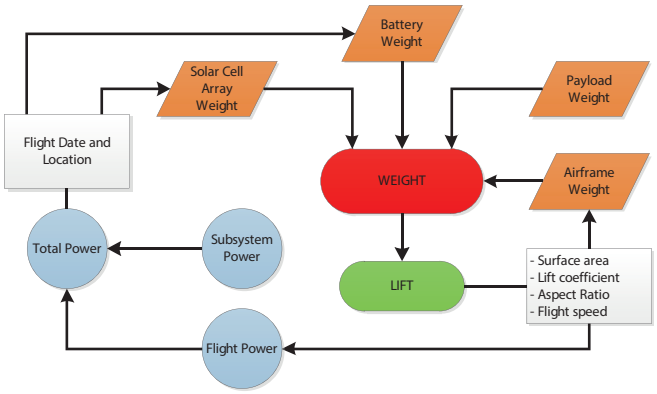

Figure 3.1: Correlation of the different parameters in the analysis

An important consideration for StratoMAV is the mission altitude, which is 15 km (see section 4.1). The density at this altitude is significantly lower than at sea-level; therefore, the amount of lift that can be generated will be lower. The drag will be lower as well. When StratoMAV has to land after one year, it will encounter different conditions which have to be considered in the aircraft design.

In the next section (section 3.2.2) the assumptions and results of the calculations are presented.

3.2.2 Design Space

The impact of the parameters is studied in order to understand the impact of certain design choices. Before the analysis can be performed, certain assumptions have to be made. These are the following.

- The solar cell efficiency is estimated at 17% [48], which corresponds to a top range thin-film solar cell.

- The solar cell mass per square meter including encapsulation is set at 0.54 kg/m^2 [10].
- The energy density for the batteries is assumed to be 400 Wh/kg, which is again for top range battery cells.
- The zero lift drag (C_{D_0}) is assumed to be 0.013 [10].
- A flight altitude of 15 km is assumed; the corresponding air density is 0.193 kg/m^3.

Now it is time to start varying the important parameters to visualise the impact of the parameters.

- The aspect ratio is varied from 12 to 24 in steps of 4. The parameters that are influenced are W_{af} (equation 3.2) and induced drag (equation 3.3). In equation 3.2, S is the wing surface area and A the aspect ratio. Coefficients 6.3 and 0.35 are based on a statistical relationship [10]. In equation 3.3 the Oswald factor (e) is set to 0.85 [10].
- The wing area is varied from 0.6 to 2.8 with a step size of 0.1. Equation 3.2 indicates the influence of S on the airframe weight. S influences the airspeed (V) when the lift coefficient (C_l) is fixed via the relation in equation 3.4.
- The lift coefficient is varied from 0.6 to 1.2 in steps of 0.2. It influences V when S is kept constant. The induced drag is influenced as well (equation 3.3).
- Two days are chosen at which the analysis will be performed, namely June 21^{st} and December 21^{st}. These days correspond to the longest and shortest day of the year. For the shortest day, the declination angle of the sun and the number of daylight hours are minimum, while for the longest day this is opposite. This makes for an interesting comparison.

$$W_{af} = 6.3 \cdot S + 0.35 \cdot A \quad (3.2) \qquad D_i = {C_l}^2/(\pi \cdot A \cdot e) \quad (3.3) \qquad V = \sqrt{W_{tot} \cdot 2/(\rho \cdot C_l \cdot S)} \quad (3.4)$$

3.2.3 Results of the Analysis

To show the effect of the aspect ratio, the plots in figure 3.3 and 3.2 are created. They depict the aircraft weight versus power need for different aspect ratios, at a fixed C_L of 1, at a latitude of 40° in the northern hemisphere, and for the shortest and longest day of the year. This latitude is chosen such that the difference between the shortest and longest day can be observed.

One can see that a slender wing (high aspect ratio) is preferable in terms of power and weight. Furthermore, the figure illustrates that in winter an aspect ratio of 12 requires much more power and weight than all other aspect ratios.

Fgure 3.3 shows that during summer, increasing the aspect ratio is favourable for the power need, but slightly increases the weight. The relation between the airframe weight and aspect ratio is given in equation 3.2.

Figures 3.4 and 3.5 depict the effect of C_L on the aircraft weight for different aspect ratios. For a larger C_L, the aircraft weight is lower. Again, looking at the blue line at the 21^{st} of December (the wing with $A = 12$), it can be seen that the overall weight is for higher for every value of C_L. In winter, the aircraft would be 18% lighter if the required C_L would be 1.2 instead of 0.6. This is mainly because the increase in efficiency leads to a large decrease in battery weight, since the aircraft flies in the night for a long time.

It can be deducted that there is a large difference between the longest and shortest day of the year. The sensitivity analysis is very useful for determining where StratoMAV has to fly, in order to be able to fly one year continuously while meeting all requirements. Section 7.2 elaborates on this topic.

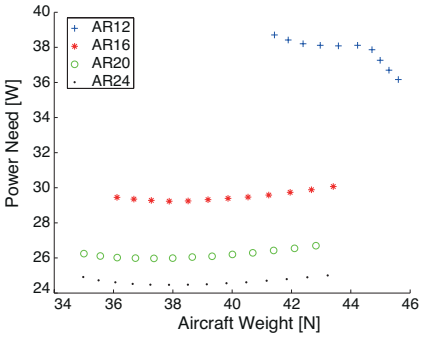

Figure 3.2: Aircraft Weight versus Power Need for a C_L of 1 and different aspect ratios on the 21^{st} of December at a latitude of $40°$

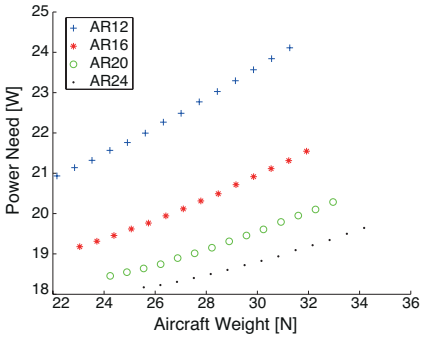

Figure 3.3: Aircraft Weight versus Power Need for a C_L of 1 and different aspect ratios on the 21^{st} of June at a latitude of $40°$

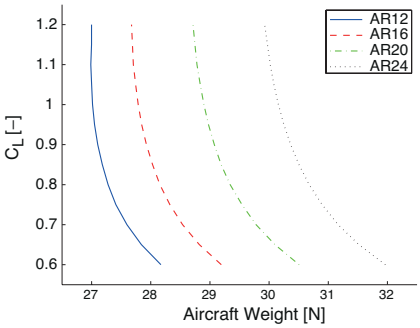

Figure 3.4: Aircraft weight versus C_l for different aspect ratios at the 21^{st} of June at a latitude of $40°$

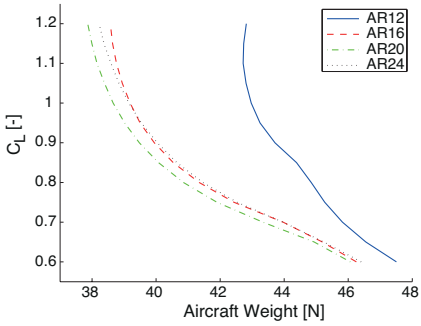

Figure 3.5: Aircraft weight versus C_l for different aspect ratios at the 21^{st} of December at a latitude of $40°$

3.2.4 Conclusion

StratoMAV should be fitted with high aspect ratio wings with an airfoil that has a large maximum lift coefficient. This is needed to be able to pass the mass requirement of 5 kg. Furthermore, by fitting these high aspect ratio wings the drag can be limited. This limits the required power which makes the aircraft more efficient and limits the battery mass. To conclude, one can say that the sensitivity analysis proved to be very useful in determining the main parameters and its influences. For StratoMAV it became clear quite quickly, that the mission location and time of the year could make or break the mission. Hence, the sensitivity analysis impelled more careful study on this topic.

Chapter 4

Aircraft Design, Stability and Control

This chapter discusses the design of the StratoMAV vehicle, its stability and control characteristics and its performance characteristics. The preliminary sizing is carried out as discussed in section 4.1. The base of the wing design is determined and some aircraft performance characteristics are discussed. After this, the wing geometric parameters are determined in more detail and an airfoil is chosen, as described in section 4.2. Next, section 4.3 discusses the final step, the stability and control requirements for StratoMAV and tail design. This preliminary design is validated using XFLR5, as can be read in section 4.4. In section 4.5 the control surfaces are designed. Hereafter is continued with the StratoMAV flight dynamics in section 4.6. Finally, some important performance characteristics are defined in section 4.7.

4.1 Preliminary Sizing and Performance

This section describes how the preliminary design of the UAV is carried out. After this, a design point can be chosen, which is used for the more detail design and describes the performance characteristics of the aircraft.

4.1.1 The W/P - W/S Diagram

To start the preliminary sizing, the weight of the UAV must be known, which is 5 kg. The sizing is done using a $W/P - W/S$ diagram. From this diagram, a first design point can be chosen, which determines the maximum lift coefficient for the airfoil selection. This is an iterative process. The right design has the lowest wing area (low mass), and the lowest required power possible. The $W/P - W/S$ diagram is made by designing for stall speed, landing and climb. The cruise speed is determined such that the power required is low but the lift suffices.

After implementing the design requirements, it was found that StratoMAV must fly at an altitude of 15 km. A higher altitude is not possible, as the UAV cannot generate enough lift. The optimal cruise speed was determined to be 18 m/s.

4.1.2 Sizing for Stall Speed

Sizing for stall speed is done using equation 4.1. The air density (at 15 km) is 0.192 kg/m^3 [11]. This is relatively low, which means that the stall speed at this altitude is critical instead of in landing

configuration (see section 9.5). The optimal stall speed (V_s) is determined to be 12 m/s. At a lower speed, the required wing surface becomes too large. The maximum lift coefficient ($C_{l_{max}}$) is set at 1.5. No high lift devices are needed, which reduces the weight of the aircraft. The wing loading becomes 20.74 N/m^2. This is a constant value with respect to the power ratio, hence a vertical line in the $W/P - W/S$ diagram is drawn in figure 4.1.

4.1.3 Sizing for Landing

The second step is to size the UAV for landing. As described in section 9.5, it is chosen not to use a landing system, which means that the approach speed should be low. This minimizes the damage caused by a belly landing. The wing loading in landing condition is given in equation 4.2 [12]. The same $C_{l_{max}}$ is used for landing as for cruise: 1.5. With the air density at sea level of 1.225 kg/m^3 [11], equation 4.1 gives a stall speed of 2.89 m/s. To make sure the aircraft does not stall, the landing speed or approach speed V_{land} is taken as 5 m/s. The landing distance s_{land} can be determined using equation 4.3 [12], which is based on statistics, and becomes 14.8 m. This equation is based on a runway and an aircraft with a landing gear. Hence, as the UAV does a belly landing, the landing distance will be lower due to the higher friction force. In equation 4.2, f is the ratio of take-off and landing weight, which is 1. Now, the wing loading becomes 22.97 N/m^2. The wing loading in landing configuration can be drawn in figure 4.1, from which can be seen that the wing loading in stall configuration is more important for sizing the aircraft.

$$\frac{W}{S} = \frac{1}{2}\rho {V_s}^2 C_{L_{max}} \qquad (4.1) \qquad \frac{W}{S} = \frac{C_{L_{max}} \rho \frac{s_{land}}{0.5915}}{2f} \qquad (4.2) \qquad s_l = 0.5915 V_{land}^2 \qquad (4.3)$$

4.1.4 Sizing for Climb

After sizing for stall and landing, the UAV is sized for climb. First, climb rate is considered using equation 4.5 [12]. In this equation, W/S is used as a variable to calculate W/P. The propeller efficiency (η_p) is estimated at 0.8 (see chapter 6). The zero lift drag coefficient (C_{D_0}) is determined after selecting the airfoil, which is done in section 4.2, and equals 0.0137. The climb rate (c) is set at 0.1 m/s at the altitude of 15 km. A higher climb rate would require more power. This induces a higher, undesirable battery weight. The climb rate is quite low with respect to other UAVs, but it does not have to change altitude fast. The Oswald factor e is estimated to be 0.8 based on reference aircraft. As described in section 3.2, the aspect ratio should be as large as possible. To prevent the structure from becoming too heavy, a moderately large aspect ratio of 20 is chosen. Equation 4.5 can now be used to plot this configuration in the $W/P - W/S$ diagram in figure 4.1.

The final step in this sizing process uses the climb gradient ($\frac{c}{V}$). The climb gradient can be determined using cruise speed and climb rate (0.1 m/s). The climb drag coefficient can be determined using equation 4.4. Since the aircraft cannot climb in stall condition (where $C_l = 1.5$), a margin of 0.2 is taken: C_l is assumed to be 1.3. The air density at 15 km altitude is used. With all the values known, the sizing for climb gradient can be calculated using equation 4.6 and plotted in the $W/P - W/S$ diagram in figure 4.1.

$$C_D = C_{d_0} + \frac{C_l^2}{\pi A e} \qquad (4.4) \qquad \frac{W}{P} = \frac{\eta_p}{c + \frac{\sqrt{\frac{W}{S}}\sqrt{\frac{2}{\rho}}}{1.345 \frac{(Ae)^{3/4}}{C_{D0}^{1/4}}}} \qquad (4.5) \qquad \frac{W}{P} = \frac{\eta_p}{\sqrt{\frac{W}{S}}(\frac{c}{V} + \frac{C_D}{C_L})\sqrt{\frac{2}{\rho}\frac{1}{C_L}}} \qquad (4.6)$$

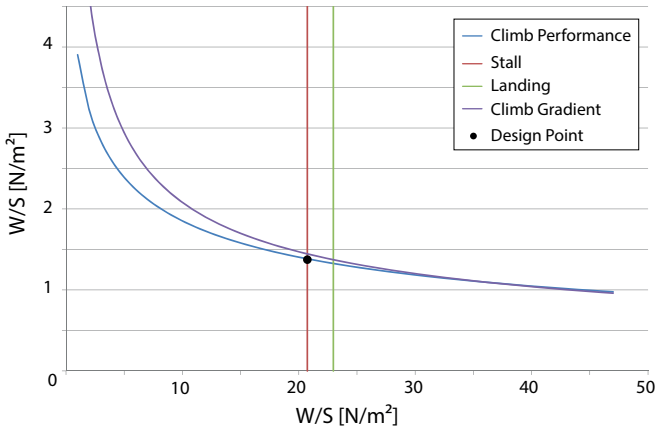

Figure 4.1: W/S - W/P diagram

4.1.5 Choosing the Design Point

It is desired to have the highest wing loading and power to weight ratio possible. This will give the smallest wing area possible, which is favourable in terms of weight and drag. Due to the requirements set by the $W/P - W/S$ diagram, the design point must be chosen in the left lower corner of the diagram, where the graphs intersect. As can be seen in figure 4.1, the optimal first design point is at a wing loading of 20.7 N/m^2. Hence, the limiting factor is the stall condition. W/S is determined to be 1.4 N/W. With this design point chosen, the first wing parameters can be determined, as well as the first flight parameters. These parameters are summarized in table 4.1.

Table 4.1: Important initial wing and flight parameters

	Parameter	**Value**	**Unit**
Aspect Ratio	A	20	[-]
Wing Surface Area	S	2.37	$[m^2]$
Span Width	b	6.88	$[m]$
Maximum Lift Coefficient	$C_{L_{max}}$	1.5	[-]
Cruise Speed	V_{cruise}	18	$[m/s]$
Stall Speed	V_{stall}	12	$[m/s]$
Approach Speed	V_a	5	$[m/s]$
Climb Rate	c	0.1	$[m/s]$
Climb Gradient	$\frac{c}{V}$	0.0056	$[-]$
Landing Distance	s_{land}	14.79	$[m]$

4.2 Wing Sizing and Aerodynamics

First, more geometric parameters for the wing are determined. Next, the basic aerodynamics of the wing are analysed. Finally, an appropriate airfoil can be chosen.

4.2.1 Geometric Wing Parameters

More geometric wing parameters like the sweep angle Λ, the taper ratio λ, the mean aerodynamic chord, the dihedral angle Γ and the wing twist angle ϵ are to be determined.

Wing sweep is only beneficial in case of high Mach numbers, and is therefore not applied. It would increase the structural weight, as a longer wing is required. Moreover, wing sweep decreases the lift coefficient by a factor $cos^2\Lambda$, which is undesirable [13]. Therefore, a sweep angle of 0° will be used.

A high taper ratio increases the structural weight and induces more drag [13]. Therefore, a moderate taper ratio of 0.5 is chosen. The root and tip chord can then be calculated using equation 4.7 and 4.8 and become 0.459 m and 0.229 m, respectively.

$$c_r = \frac{2b}{A(1+\lambda)} \qquad (4.7) \qquad c_t = \lambda c_r \qquad (4.8) \qquad \bar{c} = \frac{2C_r}{3}\frac{1+\lambda+\lambda^2}{(1+\lambda)} \qquad (4.9)$$

Now that the taper ratio has been selected, the mean aerodynamic chord is determined using equation 4.9. The mean aerodynamic chord is needed to calculate the aerodynamic centre and evaluate the stability and controllability of the aircraft (section 4.3).

The dihedral angle is set at 3°. The flight dynamics analysis (section 4.6) showed that some dihedral is favourable for the lateral stability of the aircraft. A larger angle makes the aircraft too stable, and therefore hard to manoeuvre.

The twist angle will be 0°. A twist angle has a small positive influence on the lateral stability of the aircraft. A flight dynamics analysis (as described in section 4.6) demonstrated that a twist angle makes the lateral oscillations more stable, but also decreases the damping. As the latter is not desirable, a twist angle will not be used.

4.2.2 Aerodynamics

After determining the geometric parameters, the aerodynamics of the wing must be analysed, and in particular the required lift coefficient. In loiter condition, the required lift must be equal to the total weight. As it is uncertain in this stage whether or not a tail will be used, the wing design will take this possibility into account. Consequently, the negative lift contribution of the tail has to be considered. It is therefore assumed that the required lift is 10% larger than the aircraft weight, to have a safety margin. Hence, $L = W_{total} \cdot 1.1$.

Next, the design wing lift coefficient $C_{L_{des}}$ has to be determined. This can be done using equation 4.10, where q is given in equation 4.11. $\frac{W}{S}$ is already determined in the preliminary design, $V = 18\ m/s$ and $\rho = 0.192\ kg/m^3$, which are the values for loiter. $C_{L_{des}}$ can now be determined to be 0.733.

Since the UAV is flying at a high altitude, the air density is low and thus the Reynolds number will be low. This may have an important effect on the design. The Reynolds number can be calculated using equation 4.12. In this equation, V_∞ is the free stream velocity, x is the chord length at a certain position and μ_∞ is the absolute viscosity coefficient of $1.421 \cdot 10{-}5\ Ns/m^2$ [49]. The Reynolds numbers at the tip, root and mean aerodynamic chord are 50,000, 150,000 and 100,000 respectively.

$$C_{L_{des}} = 1.1\frac{1}{q}\left(\frac{W}{S}\right) \qquad (4.10) \qquad q = \frac{1}{2}\rho V_\infty^2 \qquad (4.11) \qquad Re_x = \frac{\rho_\infty V_\infty x}{\mu_\infty} \qquad (4.12)$$

4.2.3 Airfoil Selection

The fact that StratoMAV is flying at a relatively low Reynolds (around 100,000) must be taken into consideration. For a given airfoil, the lift gradient decreases as the Reynolds number decreases. Therefore, the angle of attack for stall decreases. A thin airfoil with a high camber can generate a high lift gradient, even at the low Reynolds number at which StratoMAV must fly. Therefore, this type of airfoil will be used for StratoMAV [14] [15] [16].

After some research on high camber, thin airfoils, the MID 106 airfoil was found. This airfoil, with a thickness of 7.5% and a camber of 4.4%, is designed for a lower lift coefficient than the one required for StratoMAV. Therefore, the airfoil is modified to have a higher camber of 6%, which increases the lift coefficient to 1.5. This is shown in figure 4.2.

Moreover, the boundary layer of the original airfoil is tripped to a turbulent flow on the upper side at 60% from the leading edge. This tripping is beneficial, as an XFOIL analysis showed that the laminar boundary will otherwise separate after 60% of the chord. Making the flow turbulent before it separates causes the boundary layer to stay attached longer, which increases the lift coefficient. Figure 4.4 shows the effect of a turbulator at several locations from the leading edge (LE). This effect is explained in more detail in appendix E. To make sure the flow is fully turbulent before 60% from the LE, as is the case in the XFOIL analysis, the actual turbulator will be placed at 50% from the LE.

Hereafter, this airfoil with a camber of 6% and a turbulator, is referred to as MID 106 7.5%-6%. Its $C_l - C_d$ diagram as obtained from XFOIL is shown in figure 4.5. The lowest drag coefficient is achieved at a lift coefficient of 0.75, which is the $C_{L_{des}}$ of the UAV. The zero-lift drag coefficient, C_{d_0}, equals 0.0137. The maximum lift coefficient of the airfoil is 1.5, which is equal to the required $C_{L_{max}}$. However, it is only valid for a two-dimensional airfoil. When corrected for 3D effects, the lift coefficient decreases so that $C_{L_{max}}$ can only be reached by using high lift devices. The difference between the required $C_{L_{max}}$ and the $C_{l_{max}}$ of the airfoil is small, as determined in section 4.1, so it can be quite easily corrected with ailerons.

The $C_l - \alpha$ curve of the airfoil can be compared with the $C_L - \alpha$ curve of the wing. The data for the $C_l - \alpha$ curve (obtained using XFOIL) are shown in the left graph of figure 4.3. The curve for the wing can be obtained using equation 4.13 [12]. From statistical data, it can be estimated that $\frac{C_{L_{max}}}{C_{l_{max}}}$ ratio is 0.9 [12]. The $\Delta C_{L_{max}}$ term can be neglected because of to the low Mach number. The $C_L - \alpha$ curve of the wing can be found in the right graph of figure 4.3. As can be seen, the maximum lift coefficient for the wing is 1.3, which is lower than the required lift coefficient of 1.5. Therefore, ailerons will have to act as flaps to increase the lift coefficient to 1.5.

$$C_{L_{max}} = \frac{C_{L_{max}}}{C_{l_{max}}} C_{l_{max}} + \Delta C_{L_{max}} \tag{4.13}$$

4.3 Tail Design, Stability and Control

This section describes the design of the tail, which is needed to accomplish stability and control for the UAV. The most attention is paid to longitudinal stability and trimmability, as these are the most important aspects if one wants the UAV to stay in the air. First, a trade-off is made to decide whether a tailplane is needed at all for stability. After this, the stability and controllability of the aircraft are discussed. This leads to the sizing of the horizontal tailplane. Next, the allowed range of the centre of gravity is presented. Finally, the tail configuration is chosen and the vertical tailplane sizing is presented.

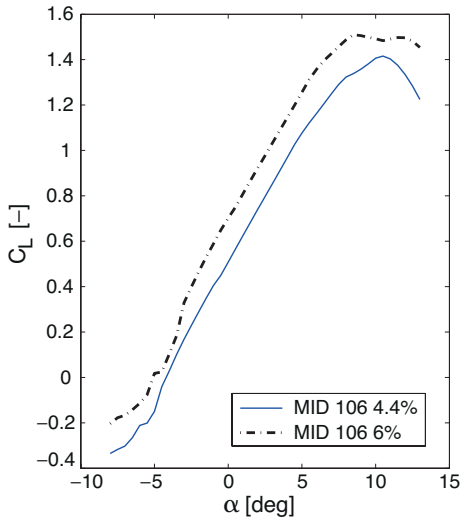

Figure 4.2: $C_l - \alpha$ curves for MID 106 airfoil with original 4.4% and adjusted 6% camber, both with turbulator at 60% from LE. Results from XFOIL, $Re = 100,000$.

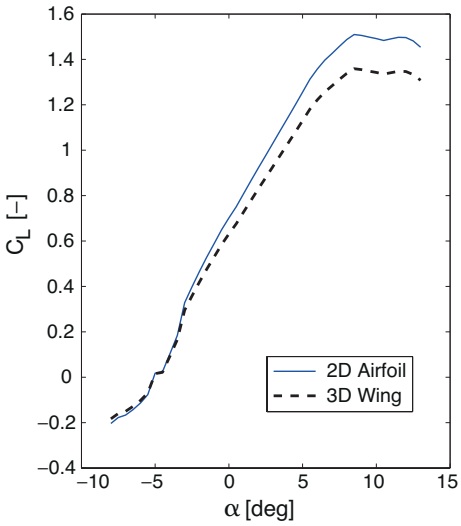

Figure 4.3: $C_l - \alpha$ and $C_L - \alpha$ curve for the MID 106 7.5%-6% airfoil and wing. Results from XFOIL, $Re = 100,000$.

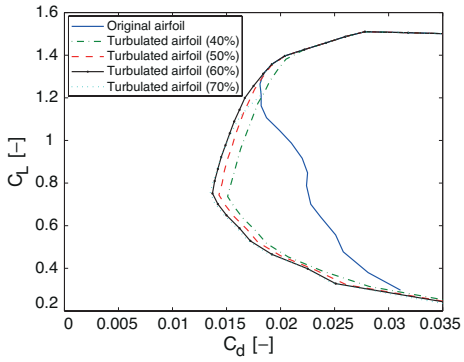

Figure 4.4: $C_l - C_d$ curves for MID 106 profile with original 4.4% camber for various turbulators. Results from XFOIL, $Re = 100,000$.

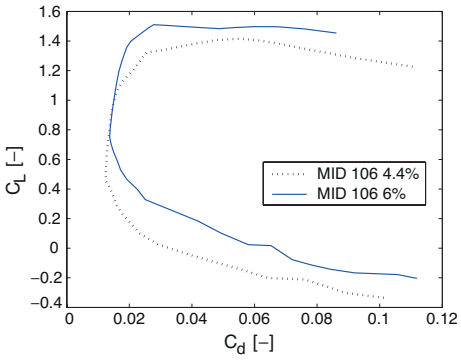

Figure 4.5: $C_l - C_d$ curves of MID 106 7.5%-6% airfoil and original 4.4% camber airfoil, both with turbulator at 60% from LE. Results from XFOIL, $Re = 100,000$.

4.3.1 Flying Wing versus Conventional Lay-out

To determine which of the two remaining concepts is preferable, a more detailed analysis about the aerodynamics is carried out.

Conventional Configuration

For the conventional configuration the MID 106 airfoil is used. At the design lift coefficient of 0.74, the drag coefficient of this profile C_{d_0} equals 0.0137. Equation 4.14 can then be used to determine C_D for the wing. With the aspect ratio $A = 20$ and the Oswald factor $e = 0.8$, C_D turns out to be 0.0249. Using equation 4.15, the drag of the wing can be calculated. With $\rho = 0.192\ kg/m^3$, $V = 18\ m/s$ and$S = 2.37\ m^2$, it is found that the drag D equals 1.83 N. To fly at an airspeed of 18 m/s, a power $P = V \cdot D = 18 \cdot 1.83 = 32.9\ W$ is required for the wing only.

The same analysis can be carried out for the horizontal tailplane. As the design lift coefficient of the tailplane is -0.75, the inverse of $C_{L_{des}}$ of the wing, it is chosen to use the MID 106 profile for the tailplane as well. The same equations as before can be used to calculate the drag caused by the tailplane. The airspeed at the tail is estimated at $V_h = 0.95 \cdot V = 0.95 \cdot 18 = 17.1\ m/s$ and $S = 0.24\ m^2$; all other parameters remain the same. This gives a drag of 0.1674 N and a required power of 2.86 W for the horizontal tailplane.

$$C_D = C_{D_0} + \frac{C_{L_{des}}^2}{\pi A e} \tag{4.14}$$

$$D = \frac{1}{2}\rho V^2 S C_D \tag{4.15}$$

From the calculations above, the drag of the wing-tail combination is estimated at 2.00 N and the power at 35.78 W. Of course, the drag and power will increase somewhat due to the tailbooms and the fact that the entire tail will be somewhat larger than the horizontal tailplane only. However, it is expected that the increase will be minor.

Flying Wing

As for the flying wing concept no wing has been designed, it is decided to analyse the relationship between S and D, and between S and C_L. This will show what the optimum wing surface is with respect to drag performance, and which maximum lift coefficient is required in that case. This analysis is set up as follows.

First, equation 4.16 is used to determine the required wing surfaces for various $C_{L_{max}}$, which is varied from 0.2 to 2.0. W is the weight (49.05 N) and V_s the stall speed (12 m/s). Then, equation 4.17 calculates all design lift coefficients for all values of S, where q is the dynamic pressure, calculated by $q = \frac{1}{2}\rho V^2$. The values for $C_{L_{des}}$ are put in equation 4.14 to calculate the drag coefficient of the flying wing. C_{D_0} is estimated at 0.014, which is the lowest value found for these type of airfoils. It is expected that this value will increase with $C_{L_{max}}$, but no exact values could be found. Estimating it at 0.014 will thus lead to an optimistic result for the drag. With C_D known, the drag is calculated by equation 4.15.

$$S = \frac{2W}{\rho (V_s)^2 C_{L_{max}}} \tag{4.16}$$

$$C_{L_{des}} = 1.1 \frac{1}{q} \frac{W}{S} \tag{4.17}$$

Now, D versus S and $C_{L_{max}}$ versus S can be plotted. These plots are shown in figures 4.6 and 4.7. It can be seen in figure 4.6 that the optimum wing surface is 1.94 m^2, which corresponds to a $C_{L_{max}}$ of 1.85. To check whether this is possible for a flying wing with a reflex airfoil, a comparison is made between StratoMAV and two other high altitude flying wings: Pathfinder plus and Helios. Data for these UAVs is shown in table 4.2 [88] [50]. Moreover, research was performed on the airfoils used for Pathfinder plus and Helios, which both use the S6078 airfoil. The maximum lift coefficients for the

S6077 and S6079 profiles at $Re = 200,000$, which are very similar to the S6078 profile, are found to be 1.05 and 1.15, respectively [18].As these profiles are representative for airfoils used on high altitude flying wings, it is assumed that it is not possible to reach a $C_{L_{max}}$ of 1.85.

Furthermore, it must be noted that the Reynolds number used for finding $C_{L_{max}}$ for the S6077 and S6079 profile is higher than the Reynolds number for StratoMAV, which is on average 100,000. This means that the lift coefficients found will be lower for the StratoMAV flight conditions [19]. How much lower exactly must be determined from experiments. However, if $C_{L_{max}}$ for S6078 is estimated at 1.1 for $Re = 200,000$, the value for $C_{L_{max}}$ at $Re = 100,000$ can be estimated to be 1.0.

With this restriction on $C_{L_{max}}$, another look must be taken at figures 4.6 and 4.7. Figure 4.7 shows that for $C_{L_{max}} = 1.0$, $S = 3.59$. From figure 4.6, it can be seen that this wing surface corresponds with a drag of 2.29 N. With a cruise speed of 18 m/s, this yields a required power of 41.22 W.

Table 4.2: Pathfinder Plus and Helios parameters

	Pathfinder Plus	**Helios**
Wing Chord $[m]$	2.44	2.44
Airspeed (Low Altitude) $[km/h]$	27	31
Airspeed (High Altitude) $[km/h]$	27	274
Maximum Altitude $[m]$	25,000	30,500
Reynolds Number (High Altitude) [-]	200,000	750,000
Reynolds Number (Low Altitude) [-]	4,700,000	5,300,000

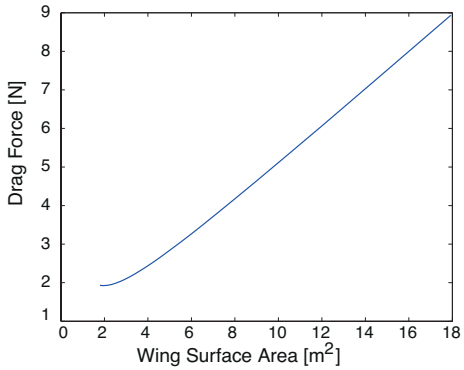

Figure 4.6: Drag versus wing surface for a flying wing

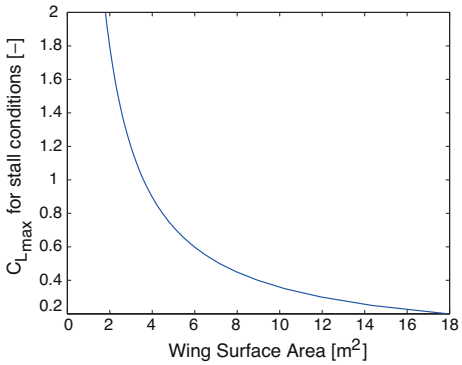

Figure 4.7: Maximum lift coefficient versus wing surface for a flying wing

Trade-off

Combining the results from subsections 4.3.1 and 4.3.1, it can be seen that the drag of the conventional configuration is lower than for a flying wing (2.00 N vs 2.29 N) and thus the required power is also lower (35.78 W vs 41.22 W). A lower required power means that a smaller and lighter battery is required. The total surface of the conventional configuration equals $2.37 + 0.24 = 2.61$ m^2 (the surface of the wing plus the surface of the horizontal tailplane), whereas the total surface of the flying wing equals 3.59 m^2. This will result in a higher structural weight for the flying wing.

It can be concluded that the conventional configuration should be chosen over the flying wing. The

conventional configuration has a better aerodynamic performance, requires less power and thus a smaller battery, and has a lighter structure.

A final note must be made about the comparison between StratoMAV on the one side, and Pathfinder plus and Helios on the other side. The reason that it is possible to use a flying wing for Pathfinder plus, is that is has a large root chord (see table 4.2). Therefore, the Reynolds number is higher than for StratoMAV, although the airspeed is lower. For Helios, both the airspeed and the root chord are larger than for StratoMAV, from which follows that the Reynolds number is higher. As a higher Reynolds number allows for more lift, both Pathfinder plus and Helios can fly using a flying wing, whereas StratoMAV cannot.

4.3.2 Design for Stability

For an aircraft with a regular camber airfoil to be statically stable, it must be able to counter a positive, pitch-up moment with a negative, pitch-down moment. A pitch-up moment is created by an increase in lift on the wing, when the angle of attack (α) increases. Therefore, an increase in α must cause a negative moment for the aircraft to be stable. This means that the moment must decrease when α increases, as described in equation 4.18.

As stated above, the centre of gravity must lie aft of the aerodynamic centre for longitudinal stability. Another requirement on the position of the centre of gravity can be found in equation 4.19.

$$\frac{dC_m}{d\alpha} < 0 \tag{4.18}$$

$$x_{cg} < x_{np} \tag{4.19}$$

$$\bar{x}_{np} = \bar{x}_{ac} + \frac{C_{L_{\alpha_h}}}{C_{L_\alpha}} \left(1 - \frac{d\epsilon}{d\alpha}\right) \frac{S_h l_h}{S\bar{c}} \left(\frac{V_h}{V}\right)^2 \tag{4.20}$$

In equation 4.19, x_{np} is the position of the neutral point. The neutral point is defined as the point where the resultants of force variations due to perturbations are applied. Its location can be calculated by using equation 4.20. In this equation, $\bar{x}_{ac}$ is the longitudinal position of the aerodynamic centre of the aircraft without the tail. The horizontal tail coefficient is given by $C_{L_{\alpha_h}}$, calculated by equation 4.21. C_{L_α} is the aircraft lift gradient, given by equation 4.22. $\frac{d\epsilon}{d\alpha}$ is the downwash gradient, given by equation 4.23. $\frac{S_h}{S}$ is the ratio of the tailplane area and used as an input for the design tool. l_h is the distance between x_{ac} of the wing and x_{ac} of the tailplane, which can be adjusted for stability. Finally, $\frac{V_h}{V}$ is the ratio of the airspeed at the tailplane and the wing. If the centre of gravity is located in front of the neutral point position found from this equation, the aircraft possesses *stick-fixed static stability* [20].

$$C_{L_{\alpha_h}} = \frac{2\pi A_h}{2 + \sqrt{4 + \left(\frac{A_h \beta}{\eta}\right)^2 \left(1 + \frac{\tan^2 \Lambda_{0.5c_h}}{\beta^2}\right)}} \tag{4.21}$$

In equation 4.21, the aspect ratio of the horizontal tail plane is given by A_h. The Prandtl-Glauert factor is given by β. The Mach number for StratoMAV is very small, so this factor has minor influence. η is the airfoil efficiency coefficient, which is assumed constant at 0.95. $\Lambda_{0.5c_h}$ is the sweep angle at 0.5c of the tail.

$$C_{L_\alpha} = C_{L_{\alpha_{A-h}}} + C_{L_{\alpha_h}} \frac{S_h}{S} \left(1 - \frac{d\epsilon}{d\alpha}\right) \left(\frac{V_h}{V}\right)^2 \tag{4.22}$$

In equation 4.22 $C_{L_{\alpha_{A-h}}}$ is the lift gradient of the aircraft without the tailplane. This can be estimated from the $C_L - \alpha$ curve of the airfoil used for the wing. This estimation is valid, because no fuselage of a significant size will be used, and thus only the wing affects $C_{L_{\alpha_{A-h}}}$.

$$\frac{d\epsilon}{d\alpha} = \frac{K_{\epsilon_\Lambda}}{K_{\epsilon_{\Lambda=0}}} \left(\frac{r}{r^2 + {m_{tv}}^2} \frac{0.4876}{\sqrt{r^2 + 0.6319 + {m_{tv}}^2}} + \left[1 + \left(\frac{r^2}{r^2 + 0.7915 + 5.0734 {m_{tv}}^2} \right)^{0.3113} \right] \left\{ 1 - \sqrt{\frac{{m_{tv}}^2}{1 + {m_{tv}}^2}} \right\} \right) \frac{C_{L_{\alpha_w}}}{\pi A} \tag{4.23}$$

In equation 4.23 r is the horizontal distance between the a.c. of the wing and the a.c. of the tailplane, divided by the wingspan and multiplied by 2. m_{tv} is the vertical distance between the wing a.c. and the tailplane a.c., divided by the wingspan and multiplied by 2. K_{ϵ_Λ} and $K_{\epsilon_{\Lambda=0}}$ are constants that account for the wing sweep angle. For zero sweep, their ratio equals 1. $C_{L_{\alpha_w}}$ is the lift gradient of the wing, obtained from the $C_L - \alpha$ curve of the airfoil.

Using the equations described above, the requirement for x_{cg} to achieve stick-fixed static stability can be found. By adjusting the size of the tailplane, the distance between the tail and the wing, the horizontal tail plane aspect ratio and the tail sweep angle, the neutral point can be moved more forward or more aft. The vertical location of the tail with respect to the wing, represented by m_{tv}, also has an influence. A neutral point that lies more aft allows for a larger x_{cg} range, as the centre of gravity must lie behind the aerodynamic centre but in front of the neutral point. Of course, a safety margin (S.M.) needs to be taken into account, to make sure the centre of gravity does not travel aft of the neutral point during flight. For StratoMAV, this margin is small: it is unlikely that payload will shift during the mission. So now, the first requirement for x_{cg} has been established.

4.3.3 Design for Controllability

Next to longitudinal stability, it is very important that StratoMAV is controllable in longitudinal direction. This also poses a requirement on the position of the centre of gravity, which can be adjusted by changing the tail design. The following section describes how to find the requirement for x_{cg} to achieve controllability.

If the aircraft must be controllable, it needs to be trimmable. This means that it must be possible to have a certain combination of wing lift and tail lift coefficients, such that the total moment coefficient of the aircraft is zero. The aircraft is said to be trimmed when $C_m = 0$. Equation 4.24 calculates the moment coefficient for an aircraft; when rearranged such as in equation 4.25, the requirement for trimmability is set.

$$C_m = C_{m_{ac}} + C_{L_{A-h}} \left(\frac{x_{cg} - x_{ac}}{\bar{c}} \right) - \frac{C_{L_h} S_h l_h}{S\bar{c}} \left(\frac{V_h}{V} \right)^2 \tag{4.24}$$

$$C_{m_{ac}} + C_{L_{A-h}} \left(\frac{x_{cg} - x_{ac}}{\bar{c}} \right) = \frac{C_{L_h} S_h l_h}{S\bar{c}} \left(\frac{V_h}{V} \right)^2 \tag{4.25}$$

where $C_{m_{ac}}$ is the moment about the aerodynamic centre of the aircraft (calculated by equation 4.26), and $C_{L_{A-h}}$ and C_{L_h} are the lift coefficients of the wing and the tailplane, respectively. For the aircraft

to be controllable, the centre of gravity must lie *behind* the value found from equation 4.25. It can be seen from equation 4.25 that the location of the centre of gravity can be compensated for by changing the lift coefficient of the tail, the size of the tail and the distance between the wing and the tail. The layout of the wing and its lift coefficient are kept constant in this design phase.

$$C_{m_{ac}} = C_{m_{ac_w}} + \Delta_f C_{m_{ac}} + \Delta_{fus} C_{m_{ac}} + \Delta_{nac} C_{m_{ac}} \tag{4.26}$$

where the terms represent the influence on $C_{m_{ac}}$ of the wing, the flaps, the fuselage and the nacelles, respectively. As no flaps, a fuselage or nacelles are used the current design, their influence is zero. $C_{m_{ac}}$ of the wing can be found from analysis of the airfoil.

It is desirable to be able to trim the aircraft at a small angle of attack. In that case, a small amount of lift is required from the tail to compensate the moment caused by the wing. Less lift also means less drag, which is always preferable. Thus, the tail must be designed in such a way that the aircraft is trimmed at a small α.

Furthermore, it is important that the aircraft is controllable in every flight condition. The most critical condition for StratoMAV is cruise, as the air density is very low and the aircraft stalls earlier. Therefore, designing for controllability is done for the cruise speed and cruise C_L.

4.3.4 Horizontal Tailplane Design

With the equations described above, the horizontal tailplane can be sized. For the design of the tailplane, some decisions had to be made considering the layout of the tail. Together with the chosen tail design parameters, they are presented in table 4.3. The choice for a fin mounted tail is based on the tail configuration chosen later on in subsection 4.3.6, as well as the choice for a fixed tail. Also, the motor is fixed to the wings, as no fuselage is used. All other choices are explained in the table.

4.3.5 Centre of Gravity Range

Now that the requirements on x_{cg} for both stability and controllability have been found, they can be combined to find the range for the location of the centre of gravity. The subsystems of the aircraft must be distributed in such a way that the centre of gravity lies in this range.

With the values for wing area, aspect ratio, cruise speed etcetera as described in section 4.1, with the airfoil described in section 4.2 and the tail design described above, the centre of gravity range can be calculated. To recapture: for stability, the x_{cg} must lie aft of x_{ac} and in front of x_{np}, and for controllability, x_{cg} must lie behind the value calculated in subsection 4.3.3. The required locations are given in table 4.4.

4.3.6 Tail Configuration and Sizing

Now that the size of the horizontal tail has been determined, a configuration for the tail and the size the vertical tailplane must be chosen. As can be found in the Midterm Report[21], an inverted V-tail has been chosen for the tail configuration. Now, the size of the inverted V-tail can be determined. To ensure that the same control and stability authority is preserved, the total area of the horizontal and vertical tailplane must be equal to the total area of the V-tail. Thus, the area of the V-tail can be calculated by equation 4.27. The required size of the vertical tailplane is found from the flight dynamics analysis as presented in section 4.6, and is equal to $0.06 \cdot S = 0.142\ m/2^2$. With the horizontal tail

Table 4.3: Tail design parameters

Parameter	Value	Comment
x_{ac}	$1/4c_r$	Estimate
V_h/V	0.95	Value for a fin mounted tail
M	0.061	Calculated using the speed of sound at 15 km altitude and a cruise speed of 18 m/s
r	$l_h/b * 2$	Depends fully on l_h
m_{tv}	0.25 m	Based on tail configuration
$\Delta_{nac}C_{m_{ac}}$	-0.05	Value for wing mounted motors
C_{L_h}	$0.35{A_h}^{1/3}$	Approximation valid for a fixed tail
S.M.	1%	Unlikely that the centre of gravity will shift during the mission
S_h/S	0.1	
S_h	0.24 m^2	
C_{L_h}	-0.75	
Λ_h	0 deg	No sweep needed, low Mach number
A_h	10	
b_h	1.54 m	
l_h	1.5 m	
λ	1	Rectangular tailplane

Table 4.4: Requirements on x_{cg}

Stability		Controllability	Centre of gravity range
$x_{ac} = 0.115\ m$	$x_{np} = 0.192\ m$	$x_{cg} > 0.153\ m$	$0.153\ m < x_{cg} < 0.192\ m$ range

surface area from subsection 4.3.4, the size of the V-tail can be calculated. By putting these values in equation 4.27, a surface area for the inverted V-tail of 0.378 m^2 is found.

Finally, the aspect ratio of the V-tail and the angle under which the planes are set must be determined. This angle is defined as the angle between the horizontal plane and the V-tail plane. From the flight dynamics analysis of section 4.6, which uses separate horizontal and vertical tail surfaces for the simulation, it is found that an aspect ratio for the horizontal tail surface of 10 is required. To make a separate vertical tailplane fit to this horizontal surface, they must have the same chord length. Therefore, an aspect ratio of 6 is required, as the vertical surface is 60% of the horizontal surface.

The aspect ratio of the V-tail and its angles must be chosen such that the projected horizontal and vertical tailplane surfaces are at least the required horizontal and vertical tailplane surface. Equations 4.28 and 4.29 are used to check the size of the horizontal and vertical tailplane. The projected span of the tailplanes, $b_{h,proj}$ and $b_{v,proj}$ are calculated from the size of the V-tail and the V-tail angle.

$$S_{vt} = S_v + S_h \qquad (4.27)$$

$$S_{h,proj} = \frac{{b_{h,proj}}^2}{A_{vt}} > 0.24\ m^2 \qquad (4.28)$$

$$S_{v,proj} = \frac{{v_{v,proj}}^2}{A_{vt}} > 0.14\ m^2 \qquad (4.29)$$

From these equations, it is found that an angle of 37.8° and an aspect ratio $A_{vt} = 10$ is needed. Furthermore, the projected width (Y-direction) is 1.54 m and the projected height (negative Z-direction)

0.60 m. The taper ratio of the V-tail is 1, which is the same as for the horizontal tailplane. This concludes the design of the inverted V-tail.

4.4 Validation of Preliminary Sizing and Aerodynamics

This section deals with the validation of the preliminary sizing and aerodynamics of StratoMAV. The model is validated on the lift coefficient, drag coefficient, required power, stability and controllability.

These parameters are plotted in figures 4.8 to 4.11. In each plot, 2 lines are shown. The green line is the plot without stabilisation and the red line is the plot with stabilisation by the tail, which can directly be seen in the $C_m - \alpha$ plot (figure 4.8). Without stabilisation, the moment coefficient decreases with an increasing angle of attack, while the moment coefficient remains constant when StratoMAV is stabilised by the tail. It can be concluded that the aircraft is stable and controllable in longitudinal direction.

The $C_L - C_D$ plot, shown before in figure 4.5, is compared to the plot produced by XFLR5, shown in figure 4.9. It can be seen that the curves correspond with each other. XFLR5 cannot calculate all values, due to the low Reynolds numbers at the tip in combination with the high lift values of the wing. The curve produced by XFLR5 shows a marginally lower drag coefficient than calculated before. The airfoil might be more efficient than assumed.

Also the $C_L - \alpha$ curves can be compared. The $C_L - \alpha$ wing curve is given in figure 4.3 and the plot produced by XFLR5 is given in figure 4.10. Both curves have a lift coefficient of 0.7 at an angle of attack of 0°. When the angle of attack increases to 8°, both curves have a lift coefficient of 1.45. At higher angles of attack, XFLR5 can not compute the lift coefficient.

The power needed at cruise condition can be validated. The power was estimated at 35.8 W at a velocity of 18 m/s. When this is compared with the power that XFLR5 calculates, as shown in figure 4.11, it can be seen that the power needed is slightly lower, namely 34 W. This difference is probably due to the fact that XFLR5 uses a lower drag coefficient than was assumed in the previous calculations.

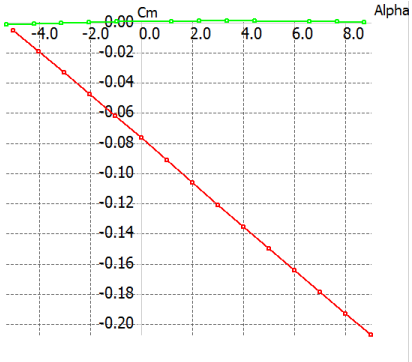

Figure 4.8: $C_m - \alpha$ curve obtained from XFLR5, Re = 100,000

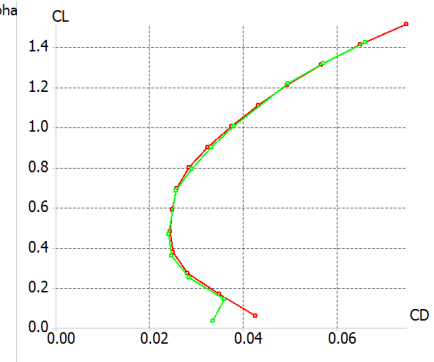

Figure 4.9: $C_L - C_D$ curve, obtained from XFLR5, Re = 100,000

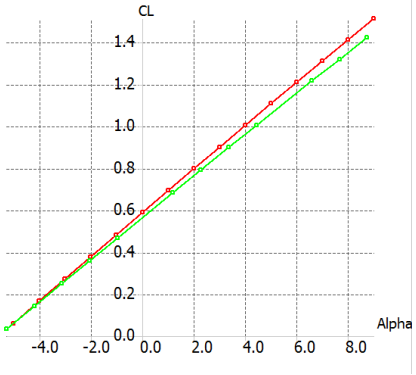

Figure 4.10: $C_L - \alpha$ curve, obtained from XFLR5, Re = 100,000

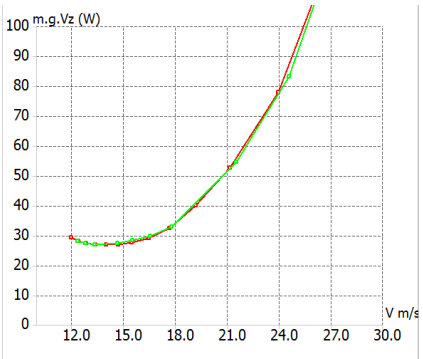

Figure 4.11: Power - Speed curve

4.5 Control Surfaces

The control surfaces are designed on the basis of the flight dynamics analysis, as described in section 4.6. The control surfaces sizes and locations influence the control derivatives, which are an input for the state-space systems. The control surfaces are therefore chosen such that the dynamic response of the aircraft is satisfactory. It must be taken into consideration that the flight dynamics simulation of section 4.6 uses a separate elevator and rudder. Therefore, the elevator design is discussed, after which the rudder is designed. These are combined into the ruddervators, as an inverted V-tail is used. Finally, the aileron design is elaborated upon and conclusions and recommendations are presented.

4.5.1 Elevator Design

The elevator size influences mainly the aircraft pitch behaviour, and naturally depends on the horizontal tailplane size. This size was determined in subsection 4.3.4. Its surface area equals 0.24 m^2, its span 1.54 m and its chord length 0.15 m. From the flight dynamics analysis it is found that the elevator must cover 90% of the horizontal tailplane span, and 40% of the chord. This gives a total elevator area of 0.085 m^2, with a span of 0.21 m and a chord of 0.09 m. The maximum elevator deflection is set at 20°. This large area for the elevator and the large deflection are needed to ensure enough controllability, as the aircraft is very stable on itself.

4.5.2 Rudder Design

The rudder size influences the roll and yaw behaviour and depends on the vertical tailplane size. The vertical tailplane surface equals 0.14 m^2, the span is 0.13 m and the chord length also 0.36 m, as it must be equal to the chord of the horizontal tailplane to combine it into a V-tail. The rudder will cover 90% of the span of the vertical tailplane and 40% of the chord. Therefore, the total rudder area is set at 0.051 m^2. Its maximum deflection will be the same as for the elevator, namely 20°.

4.5.3 Ruddervator Design

The elevator and rudder must be combined into two ruddervators. The V-tail is designed in such a way that the projected horizontal and vertical surfaces are ensure controllability and that the V-tail surface is the sum of the two surfaces. Moreover, the elevator and rudder cover both 90% of the span and 40% of the chord of the horizontal and vertical tailplane respectively. Therefore, the ruddervators should cover the same percentage of the V-tail surface. With the surface of the V-tail $S_{vt} = 0.378\ m^2$, the dimensions of one ruddervator become: Surface $S_{rudder} = 0.9 \cdot 0.4 \cdot (0.5 \cdot S_{vt}) = 0.36 \cdot (0.5 \cdot 0.378) = 0.068\ m^2$ per ruddervator. The span $b_{rudder} = 0.875\ m$ per ruddervator and the chord becomes, $c_{rudder} = 0.078\ m$.

Placing the ruddervators too close together could cause the two flaps to touch. Figure 4.12 shows where the ruddervators should be placed if they can touch each other when deflected 90° downwards. Equations can be used to calculate the ruddervator position from the top of the V-tail. With $\alpha = 37.8°$, which is the V-tail angle, and $x_1 = 0.0778\ m$, which is the chord of the ruddervator, this position turns out to be $\frac{x_3}{2} = 0.080\ m$, which is at 8.3% from the top of the V-tail. This is possible, as the ruddervators will cover 90% of the V-tail span.

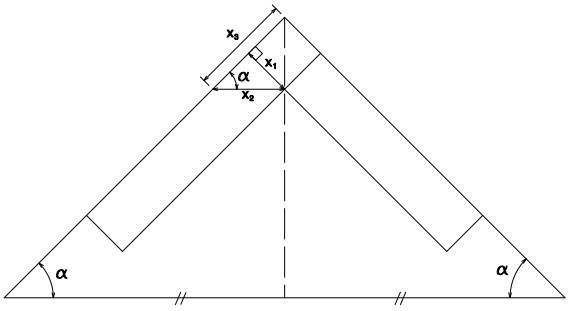

Figure 4.12: Geometry of the ruddervators of an inverted V-tail

$$x_2 = \frac{x_1}{sin\alpha} \tag{4.30}$$

$$x_3 = \frac{x_2}{cos\alpha} \tag{4.31}$$

For the ruddervators, a simple plain flap design is chosen. These flaps have a regular efficiency, but are lightweight because of their simple design. No extraordinary efficiency is needed for the ruddervators, and since a low weight is a key requirement for StratoMAV, the plain flap is the best solution [12]. However, the sealing of the hinge must be carefully done to ensure maximum efficiency.

4.5.4 Aileron Design

The aileron size and location influence the roll and yaw behaviour of the aircraft. Based on the flight dynamics analysis, it is determined that the ailerons will cover 20% of the span of the wing and 20% of the chord length. This gives the following dimensions for the ailerons: flapped area $S_{flapped} = 0.177\ m^2$, surface $S_{aileron} = 0.2 \cdot 0.2 \cdot (0.5 \cdot S) = 0.2 \cdot 0.2 \cdot (0.5 \cdot 2.37) = 0.0473\ m^2$ per aileron, outboard location $= 3.10\ m$ from the wing root, outboard chord $= 0.050\ m$ inboard location $= 2.25\ m$ from the wing root and the inboard chord $= 0.061\ m$.

The maximum aileron deflection is set at 20°. A plain flap design is chosen for the ailerons, as they are lightweight. Again, the hinge must be sealed properly, as the ailerons will otherwise lose efficiency.

4.6 Flight Dynamics

This section describes the flight dynamics analysis of StratoMAV. A linear simulation in MATLAB is built to analyse the flight dynamic characteristics. First, the linear equations of motion for the aircraft are described. Next, some of the important stability and control derivatives used for the simulation are discussed; the extensive list of all derivatives and their calculation can be found in appendix C. Finally, the eigenvalues of StratoMAV are presented and all five eigenmotions of the UAV are discussed.

4.6.1 Linear Equations of Motion

To analyse the characteristic modes of the aircraft, the equations of motion of the aircraft must be constructed. The general equations of motion are linearised and made non-dimensional, which makes it possible to make a relative simple simulation of the eigenmotions and to analyse the stability and control derivatives of StratoMAV.

The linearised equations for symmetric motion are given by equation 4.32 [20].

$$\begin{bmatrix} C_{X_u} - 2\mu_c D_c & C_{X_a} & C_{Z_0} & 0 \\ C_{Z_u} & C_{Z_\alpha} + (C_{Z_{\dot\alpha}} - 2\mu_c) D_c & -C_{X_0} & C_{Z_q} + 2\mu_c \\ 0 & 0 & -D_c & 0 \\ C_{m_u} & C_{m_\alpha} + C_{m_{\dot\alpha}} D_c & 0 & C_{m_q} - 2\mu_c {K_Y}^2 D_c \end{bmatrix} \begin{bmatrix} \hat{u} \\ \alpha \\ \theta \\ \frac{q\bar{c}}{V} \end{bmatrix} = \begin{bmatrix} -C_{X_{\delta_e}} \\ -C_{Z_{\delta_e}} \\ 0 \\ -C_{m_{\delta_e}} \end{bmatrix} \delta_e \tag{4.32}$$

The linearised equations for asymmetric motion are given by equation 4.33 [20].

$$\begin{bmatrix} C_{Y_\beta} + (C_{Y_{\dot\beta}} - 2\mu_b) D_b & C_L & C_{Y_p} & C_{Y_r} - 4\mu_b \\ 0 & -\frac{1}{2} D_b & 1 & 0 \\ C_{l_\beta} & 0 & C_{l_p} - 4\mu_b {K_X}^2 D_b & C_{l_r} + 4\mu_b K_{XZ} D_b \\ C_{n_\beta} + C_{n_{\dot\beta}} D_b & 0 & C_{n_p} + 4\mu_b K_{XZ} D_b & C_{n_r} - 4\mu_b {K_Z}^2 D_b \end{bmatrix} \begin{bmatrix} \beta \\ \phi \\ \frac{pb}{2V} \\ \frac{rb}{2V} \end{bmatrix} = \begin{bmatrix} -C_{Y_{\delta_a}} & -C_{Y_{\delta_r}} \\ 0 & 0 \\ -C_{l_{\delta_a}} & -C_{l_{\delta_r}} \\ -C_{n_{\delta_a}} & -C_{n_{\delta_r}} \end{bmatrix} \begin{bmatrix} \delta_a \\ \delta_r \end{bmatrix} \tag{4.33}$$

As can be seen in the equations above, many stability and control derivatives are needed to analyse the linearised equations of motion. How these can be found, is described in subsection 4.6.2. Other variables also appear in the equations. The ones that depend (mainly) on the aircraft geometry are:

- $\mu_c = \frac{m}{\rho S \bar{c}}$ and $\mu_b = \frac{m}{\rho S b}$
- $D_c = \frac{\bar{c}}{V}\frac{d}{dt}$ and $D_b = \frac{b}{V}\frac{d}{dt}$
- $K_X = 2\sqrt{\frac{I_x}{m}}/b$ and $K_Y = 2\sqrt{\frac{I_y}{m}}/l_{ac}$ which are the non-dimensional radii of gyration about the X and Y axes, respectively. l_{ac} is the length of the aircraft [22]. I_x and I_y are the moments of inertia and found from the lay-out of the aircraft, as presented in section 10.2.

- $K_{XY} = \frac{J_{xz}}{m}/b^2$, the non-dimensional product of inertia [22]
- $\bar{c}$ the chord length and b the span width

The remaining variables can be simulated or used as an input:

- $\hat{u} = \frac{u}{V}$ where u is the airspeed along the X-axis
- α the angle of attack, θ the pitch angle, β the angle of sideslip and ϕ the roll angle
- q the pitch rate, p the roll rate and r the yaw rate
- δ_e, δ_a and δ_r, the elevator, aileron and rudder deflection (respectively)
- V the airspeed

Both sets of equations of motion can be rewritten such that they become a state-space system, as given by equations 4.34 and 4.35. How this is done, is explained in reference [20], p.94 and onwards.

$$\dot{\mathbf{x}} = \mathbf{A}\mathbf{x} + \mathbf{B}\mathbf{u} \tag{4.34}$$

$$\mathbf{y} = \mathbf{C}\mathbf{x} + \mathbf{D}\mathbf{u} \tag{4.35}$$

where $\mathbf{x} = [\hat{u} \quad \alpha \quad \theta \quad \frac{q\bar{c}}{V}]$, $\mathbf{u} = \delta_e$ and y is the output vector. When the A, B, C and D matrices of the symmetric and asymmetric motions are put in MATLAB, two state-space systems can be constructed. The routine `eig.m` can give the eigenvalues of the two systems. These values can be examined to see if the aircraft is stable. The exact values of the eigenvalues are presented in subsection 4.6.3.

4.6.2 Stability and Control Derivatives

The stability and control derivatives of the aircraft must be calculated. This can also be done using CFD, wind tunnel testing or actual flight test. Not all equations to calculate the derivatives are presented here. Appendix C describes how they have been calculated using references. In table 4.5 and 4.6, the stability and control derivatives for StratoMAV are listed.

Table 4.5: Values of the stability derivatives

Stability Derivative	Value	Stability Derivative	Value
C_{X_u}	-0.0623	C_{n_β}	0.0044
C_{Z_u}	-0.00068	C_{Y_p}	-0.0510
C_{m_u}	0.00066	C_{l_p}	-0.3200
C_{X_α}	0.4627	C_{n_p}	0.0742
C_{Z_α}	-6.3633	C_{Y_r}	0.0023
C_{m_α}	-1.6943	C_{l_r}	0.1619
C_{X_q}	0	C_{n_r}	-0.0075
C_{Z_q}	-4.1417	C_{X_0}	-0.0309
C_{m_q}	-9.5712	C_{Z_0}	-0.6057
$C_{X_{\dot{\alpha}}}$	0	$C_{m_{\dot{\alpha}}}$	-1.5820
$C_{Z_{\dot{\alpha}}}$	-0.3765	$C_{Y_{\dot{\beta}}}$	0
C_{Y_β}	-0.0053	$C_{n_{\dot{\beta}}}$	0
C_{l_β}	-0.0572		

Table 4.6: Values of the control derivatives

Control derivative	Value
$C_{X_{\delta_e}}$	0
$C_{Z_{\delta_e}}$	-0.2240
$C_{m_{\delta_e}}$	-0.3360
$C_{Y_{\delta_a}}$	0
$C_{l_{\delta_a}}$	-0.0012
$C_{n_{\delta_a}}$	-0.00016983
$C_{Y_{\delta_r}}$	0.1237
$C_{l_{\delta_r}}$	0.0084
$C_{n_{\delta_r}}$	-0.027

4.6.3 Eigenvalues and Eigenmotions

Eigenvalues

With the state-space systems as described in subsection 4.6.1 and the stability and control derivatives found using subsection 4.6.2, the eigenvalues of the symmetric and asymmetric system can be found. This is easily done using the MATLAB routine `eig.m`. The eigenvalues for the symmetric and asymmetric motion are listed in table 4.7.

Symmetric	**Asymmetric**
-5.7214 + 5.2729i	-35.4078
-5.7214 - 5.2729i	-0.0225 + 0.9250i
-0.0409 + 0.0348i	-0.0225 - 0.9250i
-0.0409 - 0.0348i	0.0045

Table 4.7: Eigenvalues for symmetric and asymmetric motion

For the symmetric motions, it can be seen that there are two complex conjugate pairs of eigenvalues. The real parts of the eigenvalues are negative, so the symmetric motions are convergent and stable [20]. The first set of eigenvalues belongs to the short period and is heavily damped. The second set causes a lightly damped motion: the phugoid. These motions are discussed in the following.

The asymmetric motion has one complex conjugate pair of eigenvalues, and two real eigenvalues. The first eigenvalue and the real part of the complex eigenvalues are negative, but the last eigenvalue is a small positive value. This belongs to a slightly unstable eigenmotion. How unstable the motion is can be determined by looking at the time to double amplitude, given by equation 4.36 [20]. Here, λ_b is the real eigenvalue. For $\lambda_b = 0.0045$, $T_2 = 58.86\ s$, which means that the motion diverges in $58.86\ s$ to twice its amplitude. It is assumed that this gives the autopilot enough time to correct the motion. Therefore, the positive eigenvalue is not considered problematic.

The first asymmetric eigenvalue belongs to the aperiodic roll eigenmotion. The complex conjugated set belongs to the dutch roll motion. The last, positive eigenvalue gives the spiral motion. These motions are discussed in the following.

$$T_2 = -\frac{ln(0.5)}{\lambda_b}\frac{b}{V} \tag{4.36}$$

Phugoid

The phugoid motion is simulated using MATLAB's `lsim.m`, which can simulate the response. Using the state-space system of equation 4.32 with a time vector of 160 s and a step input on the elevator of 10° for 1 s, the response of the system is simulated, see figure 4.13.

A positive step input on the elevator (the flaps move 10° downwards) causes a pitch down. α and q decrease very fast as the step input starts, but recover quickly after it stops and become nearly constant. θ also decreases fast, but recovers much slower. It varies much more than α and q. The airspeed starts an oscillation, which is already damped out after half of a period.

The phugoid is damped and only makes half an oscillation. This is due to the relatively large tail, required for sufficient static stability margin. The phugoid motion is damped out after 130 s.

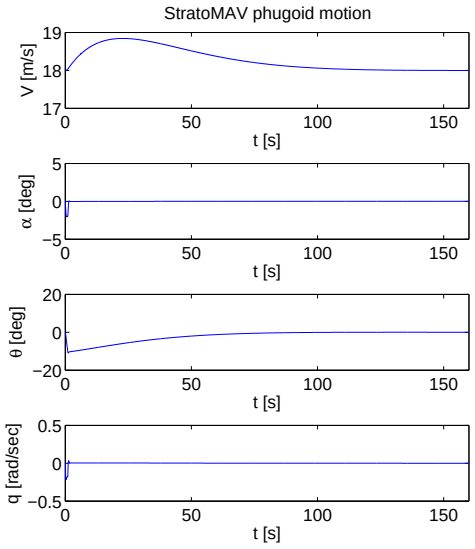

Figure 4.13: Phugoid motion of StratoMAV

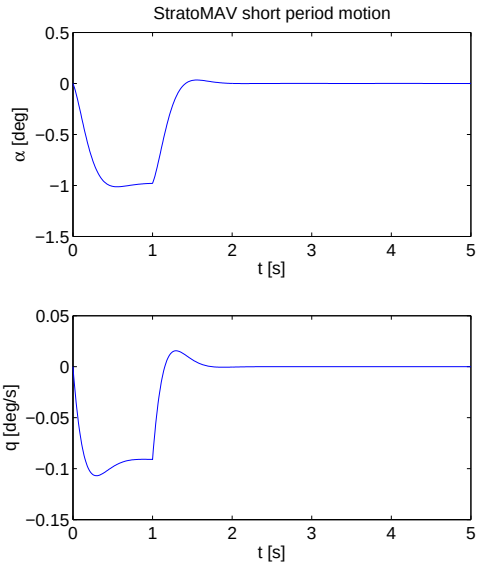

Figure 4.14: Short period motion of StratoMAV

Short period

The short period is heavily damped and is induced by a very short elevator deflection [23]. An elevator deflection of 10° for 1 s is used for the simulation. Some derivatives are set to zero. The airspeed is assumed constant. The initial steady flight condition is level, which causes θ to drop out of the equations [20]. These simplifications are needed to visualise the short period, as otherwise the phugoid motion is dominant. With a time vector of 5 s, the short period response of the aircraft can be simulated.

The result is presented in figure 4.14. As V is constant, $\hat{u}$ drops out of the state-space system, as well as θ. Therefore, only α and q are plotted. Due to the positive elevator deflection, the aircraft pitches down. It can be seen that both α and q oscillate fast and are damped out after 2 s. The difference in damping with the phugoid is large, which is typical for the short period.

Aperiodic roll

This eigenmotion is induced by an aileron deflection [20]. The asymmetric state-space system from equation 4.33 is used, with the assumption that the aircraft can only roll about its longitudinal axis. This causes some equations to drop out of the system, and only the roll rate is left to simulate. A time vector of 4 s and a step input on the elevator of $-10°$ for 1 s are used to obtain the aircraft response, shown in figure 4.15. The aperiodic roll is highly damped, which can also be deducted from the corresponding eigenvalue. The roll rate p and returns to zero very quickly after the input has stopped.

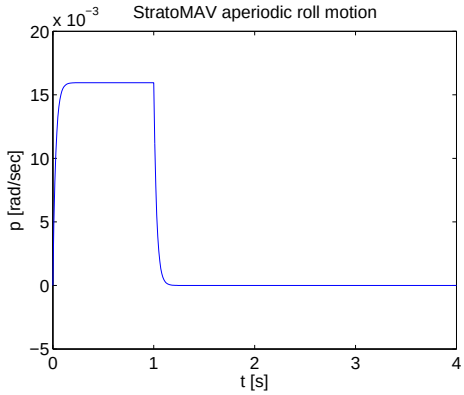

Figure 4.15: Aperiodic roll motion of StratoMAV

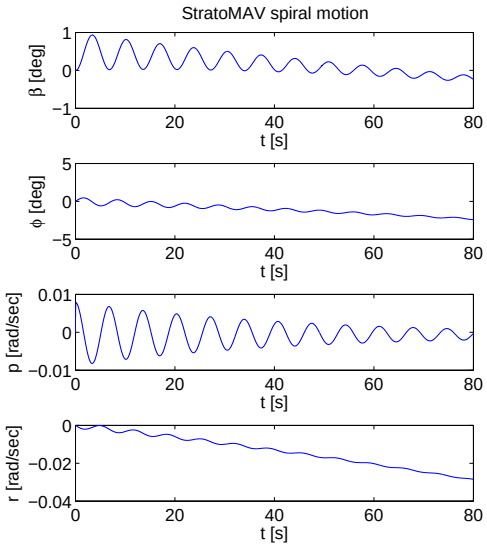

Figure 4.16: Spiral motion of StratoMAV

Spiral

This motion is induced by an aileron deflection. A time vector of 80 s and step input on the aileron of $-10°$ is applied. The spiral is an unstable motion as both the roll and yaw angle diverge, see figure 4.16. Both angles do not reach 5° within 120 seconds. Therefore, an autopilot can be programmed to prevent divergence.

Dutch roll

The dutch roll is initiated by a rudder deflection [20]. This mode is approximately stable for StratoMAV. The asymmetric state-space system is slightly adjusted for the simulation: according to [20], the derivatives $C_{Y_{\dot{\beta}}}$ and $C_{n_{\dot{\beta}}}$ can be set to zero. A step input on the rudder of 5° for 0.5 s and a time vector of 160 s are used. Figure 4.17 shows that the aircrafts yaws and rolls simultaneously, and that both β and ϕ diverge slightly. This can be corrected by an autopilot. Figure 4.18 shows that the roll rate slightly diverges.

4.7 Performance

In this section, the absolute ceiling of the aircraft is determined. Next, the turn performance is evaluated.

4.7.1 Absolute Ceiling

To determine the absolute ceiling, it must checked whether at a certain altitude, the wing can deliver the required lift coefficient and the propeller the required power. This is done by assuming a new

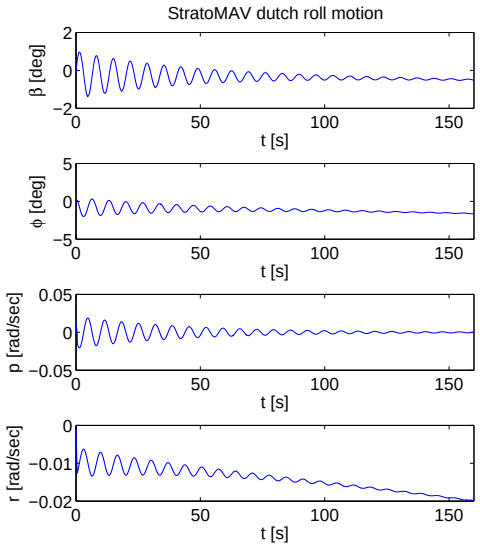

Figure 4.17: Dutch roll motion of StratoMAV

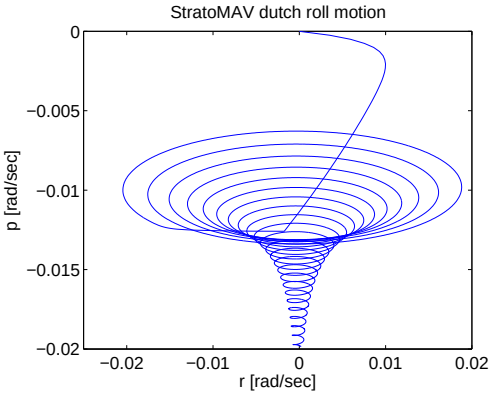

Figure 4.18: Dutch roll motion of StratoMAV - roll rate vs yaw rate

altitude, and recalculating the design lift coefficient $C_{l_{des}}$. Next, Re is recalculated and XFOIL is used to determine the new maximum lift coefficient $C_{l_{max}}$ and C_d. If $C_{l_{max}}$ is smaller than the $C_{l_{des}}$ and the drag does not cause a too high required power, the altitude can be increased. Moreover, the velocity can be increased if it turns out that the required lift cannot be reached.

The initial cruise velocity is set at 18 m/s. The velocity is not varied, until $C_{l_{max}}$ is reached. $C_{l_{des}}$ can be calculated using equation 4.10, as stated previously. At an altitude of 19 km (the first guess for maximum altitude), $C_{l_{des}}$ equals 1.37. Re is calculated and becomes 67,000. Using XFOIL, the $C_l - C_d$ plot is made, to check whether the required lift coefficient is still possible at this Reynolds number and to determine C_d at level flight. C_l at $Re = 67,000$ is 1.48. Hence, the required lift coefficient is sufficient for a level flight at 19 km, and it is assumed that the complete wing can also achieve a lift coefficient of 1.37. C_{d_0} becomes 0.023, which means that C_d is 0.06. The power needed for a level flight at this condition is 43 W. The maximum power of the engine is 155.4 W (and the maximum power that the solar panels can deliver is higher). Hence, the speed can be increased to have a lower $C_{l_{des}}$ at the same altitude, as can be seen in equation 4.11.

This process of increasing altitude and velocity is iterated, until the lift and power reach their maximum. The final velocity is 30 m/s and the altitude can be increased to 23 km, which is the absolute ceiling. $C_{l_{des}}$ becomes 0.92. With $Re = 40,000$, this lift coefficient can still be obtained by the airfoil, as can be seen in figure 4.19. At this altitude and velocity, the power required is 95 W. Taking all motor efficiencies into consideration, the power that needs to be delivered by the motor becomes 116 W (see section 6.2). If the velocity or the altitude is further increased, the required power exceeds the available power. However, it must be considered that the available thrust also decreases due to the lower Reynolds number. Also, the Reynolds number at the tip chord is lower than 30,000. Using XFOIL, it can be seen that C_l of the airfoil for that Reynolds number is much lower. Hence, testing in a wind tunnel or an actual flight test is necessary to validate if this absolute ceiling can be achieved.

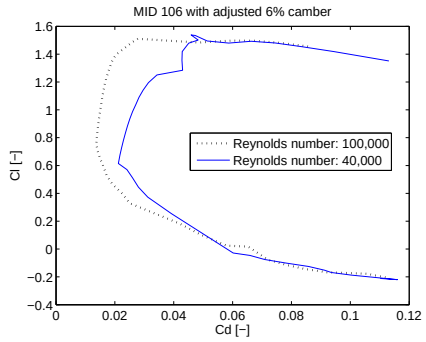

Figure 4.19: $C_l - C_d$ curves for MID 106 profile with 6% camber at a Reynolds number of 100,000 and 40,000. Results from XFOIL

4.7.2 Turn Performance

The turn radius can be calculated using equation 4.37, where V is the loiter speed of 18 m/s and $\dot{\psi}$ is the turn rate in radians 4.38, where g is the gravitational constant which equals 9.81 m/s^2 and n is the maximum load factor. As will be discussed in section 5.1, the aircraft is design for a load factor of 2. However, to ensure that if a sudden gust induces a load factor of 0.8 extra, the aircraft is only allowed to fly at $n = 1.2$. The turn rate is 0.3611 rad/s, whereas the turn radius is 69.2 m. This value will later on be compared to the requirements for following contrails, which is discussed in chapter 8.

$$R_{turn} = \frac{V}{\dot{\psi}} \tag{4.37}$$

$$\dot{\psi} = \frac{g\sqrt{n^2 - 1}}{V} \tag{4.38}$$

Chapter 5

Structures

This chapter explains how the airframe is designed. First, the design load factor determination is explained. The design then starts by considering the spar and continues with torsion box design, rib design and skin design. Finally, the tail and control surfaces are discussed.

The tailplane is not regarded when designing the main wing airframe. As the tail surface is 10% of the wing surface, the tail loads are assumed to be in order of magnitude of 10% of total lift. Preliminary analysis shows that the tailplane will mainly introduce a shear force and an additional torque on the torsion box, which are both considered negligible in magnitude.

Table 5.1 shows the relevant values from the Midterm Design phase.

Table 5.1: Midterm phase conclusion

Value	Unit	Explanation
50	cm	Maximum wing tip deflection
1	deg	Maximum wing tip section twist angle
10	mm	Spar flange width at root
2	mm	Spar flange width at tip
1	mm	Spar flange thickness
3.75	-	Maximum load factor
0.4	-	Wing taper ratio
7.5	-	Maximum chord thickness
6	-	Location of maximum thickness

5.1 Load Factor Determination

The load factor is determined from the expected scenarios during aircraft lifetime. The following scenarios apply.

- **Manoeuvring**: This includes pitching, rolling and yawing. The aircraft will not perform any high load manoeuvres like corkscrews or loopings.
- **Landing**: The wings of the aircraft should be able to sustain the loads induced by a belly landing.
- **Gusts**: A gust could occur when flying at cruise altitude, or when descending to the landing site. Gusts induce additional loads and therefore change the structural requirements.

The gust speed is expected to drive the design load requirements. The additional drag due to the temporarily increased airspeed is not taken into account in the structural design. It is found that the maximum gust speed probable to occur at cruise height is limited to a maximum of 3.65 m/s at a height of 15 km [5]. As StratoMAV is assumed to cover a large distance during its mission, it will inevitably encounter this maximum gust speed at least once.

It is assumed that a gust can hit the aircraft at any angle and thus induce a positive or negative lift. In the worst case scenario, a gust hits the aircraft and increases the α such that $C_{L_{max}}$ is reached. The corresponding load factor can be determined by adding the free stream velocity to the gust speed and using the design lift coefficient to determine the lift. This is a conservative calculation, which ensures that the wings can take the maximum load.

At cruise airspeed and altitude, the maximum load factor due to occurring gusts is 1.8, and the minimum is 0.2. At a lower altitude, the gust speeds will be higher, which induces higher load factors than 1.8 or lower than 0.2. The aircraft will descend at least five times in five years and will encounter gusts while doing this. A quiet day should be selected to land, in order to reduce gust occurrence probability. Note that the impact of a severe gust would result in more wing deflection than desirable, however it will not directly result in yielding.

For turning, a load factor of 2 is chosen such that a gust can be encountered at the same time. Section 4.7 showed that with this load factor, a turn with a radius of 69.2 m is possible, which is sufficient. It is assumed that the aircraft designed for a maximum load factor of 2 will also be able to withstand a load factor of -1. Therefore, the aircraft will be designed to withstand a load factor of 2.

5.2 Spar Design

In order to properly design a spar, its functions and requirements are identified. These are:

- Resist the bending moment
- Resist the shear forces
- Resist any normal forces
- Resist any forces introduced by control surfaces
- Fulfil requirements on spanwise deflection

The main issue in spar design is finding a structure able to resist the bending moment. For the wing tip deflection due to bending, a maximum deflection of 0.5 m is set as a requirement. The deflection decreases as the moment decreases, the section inertia in bending direction increases and the Young's modulus increases. The bending moment depends on the wing load, the section inertia depends on the spar design, and the Young's modulus depends on the selected material. As a simplification, the spar design assumes there are no normal loads applied.

The largest section inertia, which is still lightweight, is achieved using an I-section. The airfoil limits the size of the I-section. Note that the spar flange and web are not considered to be of similar material. The web should be designed for carrying the shear loads occurring in the web. It will not carry the main loads induced by bending.

5.2.1 Spar Flange Design

Firstly, a material for the flanges is chosen, that ideally has a high specific Young's modulus in order to minimise strain. Secondly it would have a high specific yield strength, creating the highest ultimate

load resistance. It can be seen, using the same manner as discussed in appendix G, that Carbon Fibre Reinforced Plastic (CFRP) performs best on the set criteria. CFRP is manufacturable, not very expensive and readily available. Therefore, CFRP (unidirectional fibre direction), is selected as spar flange material.

Considering the calculations from the Midterm Phase [21], based on unidirectional CFRP, a 10 mm wide spar flange and 1.1 mm thickness are able to bear the loads induced by the load factor of 3.75. The new load factor of 2 requires less stiffness, which means that a lighter spar is possible.

The design is continued by considering the moment distribution. The spar will run from tip to root; its height will be equal to the thickness of the airfoil at 23% of the chord. After several design iterations, the following spar design is the result. The section moment of inertia distribution is shown in figure 5.1, based on an I-section with a constant flange thickness of 1.1 mm. The width of the flange at the root and tip is equal to 10 mm and 2 mm respectively.

5.2.2 Wing Tip Deflection

Using the spar moment of inertia, the deflection and failure check can be performed. Using the moment of inertia shown in figure 5.1, the deflection can be computed. This is done by twice integrating the moment curve and subsequently dividing by the inertia and the Young's modulus of CFRP. The total tip deflection is computed to be 0.18 m, which is significantly smaller than the requirement of 0.5 m. This means that a large safety factor is included.

The failure check is based on the moment of inertia per section. For this, the maximum normal stress per spanwise location is computed. The stresses are divided by the compressive strength (for CFRP 1.5 GPa), making this a fraction, as displayed in figure 5.2. As long as the fraction does not exceed 1, the spar will not fail. As can be seen in the figure, this is the case, as the deflection requirement is driving the design to a larger extend than the failure requirement.

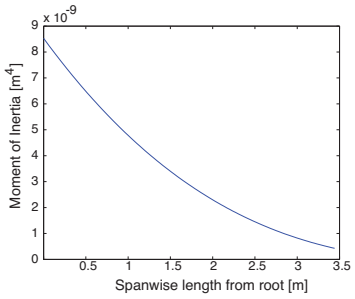

Figure 5.1: Moment of inertia distribution over the span

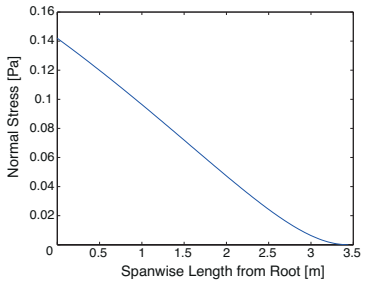

Figure 5.2: Maximum normal stress fraction over the span

The spar flange mass is determined to be 110 g, by summing all section surfaces, multiplying this by the spar thickness and CFRP density ($\rho_{CFRP} = 1600\ kg/m^3$). Note that in order to create the dihedral angle from section 4.2, the spar should be cut in half and a small joint should be applied in the middle of the spar.

5.2.3 Spar Web Design

The spar web has two functions: ensuring the flange position and supporting the shear loads. The web material should be able to withstand the local shear forces and have a low density. Figure 5.3 shows the

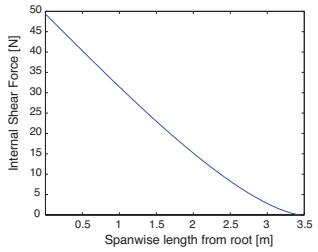

Figure 5.3: Shear force distribution over the wing

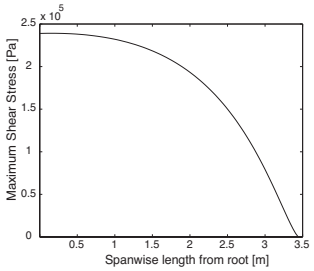

Figure 5.4: Shear stress distribution over the wing

shear force to be resisted, based on a load factor of 2. The material should be able to carry 49 N shear force. The maximum shear induced stress will occur in the top web section. Equation 5.1 is used to compute the maximum shear stress. The shear force is assumed to occur in line with the shear centre, or centre of gravity for this doubly symmetric geometry. For equation 5.1, the shear stress is assumed to vary linearly over the profile height. It follows that the highest shear stress is twice the average shear stress, as given in equation 5.1, in which $F_{shear_{max}} = 2 \cdot 49\ N$, and the web area is $44 \cdot 10^{-5}\ m^2$ ($10 \cdot 10^{-3} \cdot 4.4 \cdot 10^{-2}\ m^2$).

$$\sigma_{max_{root}} = 2 \cdot \frac{F_{shear_{max}}}{Area_{web}} = 0.23\ MPa \tag{5.1}$$

The web thickness equals the spar width, for the web should support the flanges over the whole width to prevent buckling. The web height is assumed equal to the maximum local airfoil thickness, the flange thickness is neglected for simplicity. The spar flange width at the root and tip are 10 mm and 2 mm respectively. Two things can occur. Firstly, the maximum shear force is distributed over the wing as desired. Secondly, the maximum shear stress is equal to 0.24 MPa, and occurs at the root.

The web material can now be selected, based on the shear stress. The material performing best is ROHACELL 51, with a density of 52 kg/m^3. This is done using the method described in appendix G. This foam is readily available, easily manipulable and costs €100/kg. The total amount of spar foam will have a mass of approximately 50 g.

5.2.4 Spar Cost

The spar consists of two flanges glued to a web. For the flanges material, twice the span is required with thickness of 1.1 mm. For one strip of CFRP with a length of 1.40 m, a width of 4 mm and a thickness of 1.1 mm the price is €6.03 [51]. Three strips are needed if no removed material would be recycled. This results in 30 strips, or a price of €180. This includes material losses due to mistakes in fabrication processes, since the spar is tapered and would not require three strips wide over the total span.

The ROHACELL 51 foam costs €100/kg, and the total foam mass is 50 g. The spar is tapered and therefore material is lost when cutting the foam. It is assumed that therefore twice the volume is required. The foam will then cost €10 and the total spar material cost is €190.

5.3 Torsion Box Design

For the torsion box design, its functions and requirements are identified:

- Resist the bending moment
- Resist the shear forces
- Resist any normal forces
- Resist any forces introduced by control surfaces
- Resist the torque introduced by the wing lift distribution
- The wing should not twist more than half a degree from tip to chord

It is assumed that the torsion box only resists the torque introduced by the lifting force, as its stiffness in longitudinal or lateral direction will be significantly less than components specifically designed to take these forces. The torsion box design is therefore based on the required stiffness to resist torque. Figures 5.5 and 5.6 show the internal torque and twist distribution resulting from the preliminary design phase.

Obviously, a closed torsion box is preferred over an open section. Based on the preliminary design, it becomes clear that the preliminary (closed) torsion box already satisfies the requirements for twist, based on the previously applied higher load factor. Secondly, the moment coefficient has been determined to be -0.16 (previously -0.20) from the aerodynamic design. The torque T is computed as a function of load factor $n = 2$, cruise speed $V_{cruise} = 18\ m/s$, wing surface $S_{wing} = 2.37\ m^2$, moment coefficient $C_{m_{cruise}} = -0.16$ and average wing chord $\bar{c} = 0.3442\ m$.

$$T = n \cdot (0.5 \cdot \rho \cdot V_{cruise} \cdot S_{wing} \cdot C_{m_{cruise}} \cdot \bar{c}) \tag{5.2}$$

Equation 5.2 gives a total torque of $-8.2\ Nm$. The torque distribution is illustrated in figure 5.5. Note that this is a distribution depicted for half the wing, which therefore ends at half the value computed in equation 5.2, which is the summation of all torque generated over the complete wing.

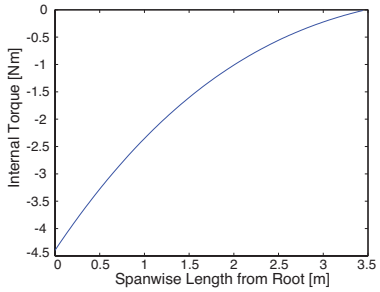

Figure 5.5: Torque distribution ($n = 2$, $C_m = -0.16$)

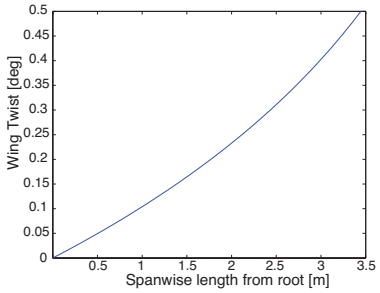

Figure 5.6: Twist distribution ($n = 2$, $C_m = -0.16$)

Torsion Box Material

Torsion box material should have a high specific shear modulus, and the best material would also provide a high specific Young's modulus. As expected from the Midterm Report [21], CFRP turns out to be most suitable and is selected for the torsion box. This is determined using the same method as described in appendix G. The CFRP fibre direction will be put in a $\pm$ 45 degrees orientation with respect to the longitudinal direction.

5.3.1 Torsion Box Geometry

The torsion box surrounds the total front section in front of the spar. The box will have the same shape as the airfoil. The thinnest skin section is weakest and therefore driving. In the Midterm Report [21], it is suggested to apply a 0.1 mm thick skin. This skin sheet thickness is one of the thinnest materials commercially available and has a mass of about 0.115 kg/m^2.

Applying the load factor and using the material and geometry above, a maximum twist of half a degree results. The torsion box torsional stiffness will not be adjusted to meet the requirement of one degree. The Finite Element Analysis (FEA) shows more severe deflections.

5.3.2 Torsion Box Mass and Cost

The torsion box mass is computed by calculating the torsion box surface, and multiplying this surface by the carbon sheet mass per square metre (115 g/m^2). The torsion box surface is computed using the airfoil coordinates. The location of maximum thickness (at 23% chord length from the leading edge) is assumed to be the end of the torsion box. The torsion box circumference turns out to be 58.5% of the chord length.

Equation 5.3 shows how the total torsion box surface is computed. The wing is divided into n segments (in this case $n = 200$), for which for every section the chord length is known. D denotes the span wise distance of every segment. The total CFRP-sheet for the torsion box is 1.4 m^2. Since the skin sheet has a mass of 0.115 kg/m^2, the total torsion box mass will be 161 g.

$$Surface = \sum i = 1^{n} Chord_i \cdot D \cdot 0.585 \approx 1.4m^2 \tag{5.3}$$

The CFRP sheets of required thickness cost €120/m^2 [51]. Assuming a material loss of 30%, the torsion box material price is €218.40.

5.4 Rib Design

To design the ribs, their functional requirements are analysed. These are:

- Absorb the loads taken by the skin at the back section
- Prevent the torsion box from buckling at the front section
- Transfer the forces to the spar
- Transfer forces induced by control surfaces
- Transfer forces induced by other subsystems (e.g. batteries)
- Retain the airfoil shape in spanwise direction

5.4.1 Back Rib Material Selection

The forces that the ribs are subjected to are low. Therefore thin ribs will be enough to withstand and transfer these loads. As thin sections are prone to buckling, a material should be found that is both lightweight and has a good buckling performance.

To make an objective choice for this material, the following analysis was performed based on the method of Ashby [24]. The analysis comprises of judging every material in a database (CES Edupack) for its

performance on buckling. Two columns are assumed, both with length l and equal mass. The column with the highest buckling load thus represents the material with the highest specific strength. One of these columns is the reference column with $\rho_{ref} = 1\ kg/m^3$, a width and thickness of 1 mm and thus $I = \frac{1}{12}$. The second column has a density of ρ_2. For the second column to have the same mass as the reference column, its width and thickness should be $\sqrt{\frac{\rho_{ref}}{\rho_2}} \cdot 1\ mm$. The second column thus has $I_2 = \frac{1}{12} \cdot \left(\sqrt{\frac{\rho_{ref}}{\rho_2}}\right)^4$. Substituting this last relation in the Euler buckling equation for a simply supported beam yields:

$$F_{buckling} = \frac{\pi^2 \cdot E \cdot \frac{1}{12} \cdot \left(\sqrt{\frac{1}{\rho_2}}\right)^4}{l^2} = \frac{\pi^2 \cdot E}{12 \cdot l^2 \cdot \rho_2^2} \tag{5.4}$$

Because l and ρ_{ref} are constant for both columns, it can be concluded that the material with the highest specific buckling performance is the material with the highest value of $\frac{E}{\rho^2}$. Appendix G shows the comparison.

It follows that balsa wood is the best choice for the ribs. Balsa wood is readily available, not costly [52] and can be easily shaped. It is therefore selected as material for the ribs. Balsa wood has a density between 90 and 110 kg/m^3.

5.4.2 Back Rib Force Analysis

The ribs are supposed not to take any other forces than those transferred by the skin. The forces generated by the lift are assumed to only put a vertical force on the ribs, so drag is not accounted for. The exact wing lift distribution is not known and is therefore approximated as shown in figure 5.7. It is not known how much of the force will be carried by the back ribs, and how much by the front ribs. Therefore, the design is conservative; the back ribs are assumed to be subjected to the full lift load. Furthermore, the wing section behind the spar is assumed to have a linearly decreasing pressure distribution from leading edge to trailing edge.

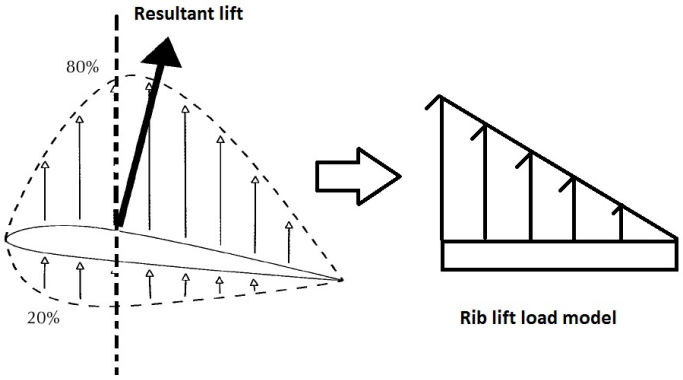

Figure 5.7: Back rib lift load model

Multiplying the 2D-pressure per section by the rib spacing gives the total force carried by each rib. A larger rib spacing will induce a higher force per rib but reduces the weight of the ribs. A smaller rib spacing will better retain the airfoil shape and prevent buckling, but is heavier. An optimum has to be found here.

The rib spacing is now fixed at 10 cm, which is based on comparable constructions used in radio controlled model aircraft. The force that one rib will be subjected to is computed using equation 5.5. It is assumed that the maximum force per rib is the maximum total wing load divided by the amount

of back ribs. Using a load factor of $n = 2$, an aircraft weight of $W = 5 \cdot 9.81$, a span $b = 6.88\ m$ and a rib spacing of $0.10\ m$, the maximum force per rib is $1.43\ N$.

$$F_{rib} = nW_{aircraft}\frac{Spacing_{ribs}}{b} \tag{5.5}$$

5.4.3 Back Rib Design

The back rib outer geometry is completely fixed by the airfoil shape. Furthermore, the rib should be fixed to the spar. The rib thickness is assumed to be $1.5\ mm$ thick, based on comparable radio controlled aircraft constructions and manufacturing limits of balsa wood.

The back rib mass can be reduced by cutting out material. The outer rib surface should not be removed, since this fixes the airfoil. It is assumed that the outer $1.5\ mm$ are be sufficient to transfer the loads. The inner section is now cut out until a truss structure remains. It is estimated that up to half of the total surface of each rib is removed, for example by laser cutting balsa sheets of required rib thickness. All inner cut truss edges must be rounded with a radius of at least 2 millimetres in order to reduce stress concentrations.

The average airfoil surface for the whole wing box can be computed by drawing a rectangle with a height equal to the local airfoil thickness and a width of the local chord length. It is assumed that 80% of the rectangle will be covered by airfoil, wich wil be the basis for the rib surface. Subsequently, the back rib runs from 23 % of the chord to the trailing edge. This gives an average back rib surface of $68\ cm^2$. With a rib thickness of $1.5\ mm$, a balsa wood density of $100\ kg/m^3$ and a total amount of ribs (70), the total back rib mass becomes $71\ g$.

5.4.4 Front Rib Design

For the front rib design, the loads induced by the torsion box should be considered. The torsion box transfers a relatively high load and should therefore be protected from buckling. The front rib spacing is therefore small, ensuring the torsion box shape. A rib spacing of $2\ cm$ is assumed to suffice based on comparable radio controlled aircraft having similar structural concepts. This spacing results in a total of 344 front ribs. The rib thickness is assumed to be equal to the thickness used for the back ribs.

In analogy to the back rib mass computation, the front rib mass can be computed. The front rib surface is estimated to be $20\ cm^2$. With 344 ribs and a density of $100\ kg/m^3$, this gives a total mass of $100\ g$.

5.4.5 Rib Cap Strips

In order to assist the back ribs in transferring the forces into the spar, cap strips are glued over the top and bottom of the back ribs onto the spar. These are small CFRP strips, as wide as the back ribs are thick, or $1.5\ mm$. The strips have a thickness of $0.12\ mm$. Applying 70 cap strips over the twice back rib length (for covering top and bottom) of $2\ mm$ by $0.12\ mm$ thickness, the total mass is $30\ g$.

5.4.6 Rib Material Costs

A sheet of balsa wood of the required thickness ($1.5\ mm$) costs €1.95 for $100\ cm$ by $10\ cm$ [52]. Including material losses, 15 back ribs and 15 front ribs can be produced per sheet. Out of 5 sheets,

70 back ribs and 70 front ribs can be cut. The remaining 264 front ribs are cut out of 14 sheets. This adds up to 19 sheets, or €37.05 for the balsa.

The cap strips cost €1.38 per metre, when ordered at 1.5 mm width and 0.12 mm thickness [51]. Using 70 back ribs (since the front ribs do not need cap strips) of average length 25 cm, 17.5 m of cap strip is needed, which costs €24.15 in total. The total rib material price, including cap strips, would be €61.20.

5.4.7 Rib Design Considerations

For the subsystem integration, the ribs concept are convenient. The aircraft centre of gravity should lie in a certain range (see section 4.3). The subsystems can be placed freely due to the possibilities the ribs offer. Any subsystem to be integrated can be easily mounted and attached in cut-outs in the ribs by means of glue or screws. If the subsystem is heavy (for example a battery), the applicable ribs are made thicker or the truss structure is replaced by a solid rib. A small CFRP tube is placed at the trailing edge. This has a double function. It fixes the back ribs and supports the back foil at trailing edge location. The tube hardly bears any load, and is therefore very light (10 g). For this reason it is not considered in the mass budget.

5.5 Skin Design

The torsion box serves as skin for the wing front part. The back part of the airfoil should be covered with foil in order to finish the complete structural wing design. The total wing surface is estimated to be 2.15 times the projected wing area. This means that the total wing outer surface is 5.1 m^2 ($2.15 \cdot 2.37$ m^2). The back rib (which the back skin should cover) covers 77% of the chord, and it is therefore assumed that the back skin surface is 77% of the total outer wing surface. This results in 3.93 m^2 back skin surface. Conventional radio controlled aircraft use crimp foil to cover the back skin, which is proposed to do here as well. Oracover is often applied and has a mass of 36 g/m^2 [53], for the light version of Oracover, Oralight. This foil is 12 μm thick and is made of polyethelyne teraphthalate (or PET). This results in a 141 g for the total back skin mass. The skin will be glued to the solar cells, which is regarded feasible, since the local skin deformation is small enough to not introduce significant forces to the solar cell array. Section 13 will give suggestions for combining skin design and solar cell foil in structural sense.

5.5.1 Skin Material Cost

The total skin surface is 3.39 m^2. The Oracover foil costs €105 for a roll of 0.6 m by 10 m [53]. Accounting for material losses, one roll will be needed and the skin material adds up to €105.

5.6 Tail Design

The inverted V-tail will be connected to the wing with two booms, as introduced in chapter 4. The tail will be subjected to minor loads in comparison to the main wing. If the tail surface is assumed to be a downscaled main wing (with same structural concept), the relative loads will be similar. It is assumed that the mass is linearly related to the surface area, which is somewhat conservative. However, this will ensure that the tail design can sustain the applied loads. The tail surface is 0.378 m^2, which is 10% of

the surface of the main wing. The mass of the tail airframe is therefore approximated to be 10% of the main wing mass. Recommendations for improving this tail plane design are given in chapter 13.

The distance from the main wing aerodynamic centre to the tail wing aerodynamic centre measures 1.5 m. Therefore, two booms of 1.5 metres length (8 mm outer diameter, 2 mm thick) are required to join the wing and tailplane. A one metre long CFRP-tube is used, which can carry loads up to 20 g. It has a mass of 16 g/m [51]. The tube is hollow, which makes it possible to let servo and power wiring go trough the tail booms into the tail for controlling the ruddervator. In total 3 metres of boom is used, and therefore the total boom mass is 48 g. A 10% of the main wing lift is assumed to be generated by the tail. The tail is connected with two booms, and every boom is therefore assumed to transfer 5% of the main wing load. The moment corresponding to this force at location of the main wing connection is 7.35 Nm ($0.05 \cdot 2 \cdot 49\ N \cdot 1.5\ m$). The (polar) moment of inertia for the boom is $3.22 \cdot 10^{-9}\ m^4$ ($\pi \cdot 8 \cdot 10^{-3^3} \cdot 2 \cdot 10^{-3}$). The maximum stress is 9.1 MPa, which would be a maximum 0.6 % strain.

5.7 Aileron Design

Finally, the aileron design for StratoMAV is discussed. The addition of ailerons is assumed not to increase the mass of the airframe a lot. The ailerons will be implemented by "cutting out" the required wing surface at the trailing edge side. A CFRP control bar will run through the front side of the aileron, connected to the rib and a servo. At the servo location the rib is stronger than the average rib in order to transfer the increased forces coming from the ailerons. The aileron construction will consist of ribs with smaller spacing (forces increase when the aileron is deflected), having multiple little carbon tubes running through them to serve as "aileron spars". At the back rib section, the ribs will be covered with skin foil. Adding an aileron is estimated to add 20% to the mass of the wing, accounting for the CFRP control bar. According to chapter 4, the aileron runs from 2.25 m to 3.1 m spanwise. The surface of the two ailerons equals 0.094 m^2, which is 4% of the total wing surface. Adding the ailerons thus results in a 0.8% mass increase due to the ailerons.

5.8 Conclusion

The complete airframe has now been designed. The most important design parameters are tabulated in table 5.2. The total material costs are tabulated in table 5.3. It includes two jars of 90 g adhesive (€ 20) [52], for glueing all parts together. It is assumed that the tailplane assembly adds 20% to the main wing costs. It must be noted that this price does not include labour costs. The total price could easily rise, since processing CFRP and laser cutting balsa is time consuming and therefore expensive. The first StratoMAV is assumed to consume 100 labour hours, or € 2000 when assuming € $20/hr$ wage.

Table 5.2: Airframe design conclusions

Conclusion	Explanation	Conclusion	Explanation
-1	Most negative load factor	0.5 deg	Torsion box twist under
2	Most positive load factor		a load factor of 2
CFRP	Spar flange material	Balsa wood	Rib material
ROHACELL 51	Spar web material	68 cm	Average back rib surface
10 mm	Spar width at the root	20 cm	Average front rib surface
2 mm	Spar width at the tip	1.5 mm	Rib thickness
1.1 mm	Spar flange thickness	10 cm	Back rib spacing
12 cm	Maximum vertical wing	2 cm	Front rib spacing
	tip deflection	71 g	Back rib mass
49 N	Maximum shear force,	30 g	Cap strip mass
	occurring at the root	100 g	Front rib mass
0.24 MPa	Maximum shear stress	201 g	Total rib mass (including
	in the spar web		cap strips)
160 g	Total spar mass	Oralight	Skin material
-8.2 Nm	Maximum torque,	3.93 m^2	Skin surface area
	occurring at root	141 g	Skin mass
CFRP	Torsion box material	73 g	Total tailplane mass
0.1 mm	Torsion box material thickness	819 g	Total aircraft airframe mass
161 g	Torsion box mass		

Table 5.3: Material costs

Price	Item
€190	Spar
€218.40	Torsion box
€61.20	Ribs
€105	Oracover back skin
€20	Glue
€595.60	Main wing (excluding tail)
€714.72	**Total material costs**

Chapter 6

Propulsion System

In this chapter the main features of the propulsion system are discussed. Firstly, section 6.1 elaborates on the design of a custom propeller for StratoMAV. Secondly, the motor choice is discussed in section 6.2. Lastly, the design for a custom gearbox is given in section 6.3 and a summary is given in the conclusion (section 6.4).

6.1 Propeller Design

This section introduces the derivation of the advance and pitch diameter ratio. Hereafter, the final design performancer is discussed, followed by the propeller construction. This section ends by presenting the propellor mass and costs.

6.1.1 Derivation of Advance and Pitch Diameter Ratio

In order to design a propeller, one first has to determine the advance ratio J, and pitch diameter ratio P/D. The dimensionless J (equation 6.1) gives the relation between the distance the propeller moves forward in one revolution and the diameter of the propeller. In which V_∞ is the free stream velocity, n is the number of revolutions per second and the propeller diameter is given by D. The pitch diameter ratio gives the relation between the pitch angle and propeller diameter. Because there is not a lot of reference data available, a model for a propeller was created using blade element momentum theory. The validation and working principles of this model are in appendix F. The model gives a good estimate of the propeller performance.

$$J = \frac{V_\infty}{n \cdot D} \tag{6.1}$$

The model was ran for three different chord lengths and for four different diameters. The airfoil of the propeller is a Clark Y airfoil, which is a common propeller airfoil, but with a modified maximum thickness for the low Reynolds numbers at which the mission is performed. When the P/D ratio is varied, different efficiency curves arise as can be seen in figure 6.1. These graphs are constructed for different diameters and chords. The maximum of the overarching curve of the efficiency curves gives an optimal value for J and the corresponding P/D ratio. The results from the graphs are listed in table 6.1. Resulting from the thrust coefficient (c_T) curve in the model, the thrust coefficient (c_T) value at the calculated J can be found.

Equation 6.1 and 6.2 enable us to calculate the last two unknowns: number of revolutions per minute, n, and diameter, D. Different combinations of propellers and amount of blades were tried and T was divided by the number of propellers and blades. In other words, this determines T per propeller blade. After the value of D is found, one can deduce its efficiency from the gathered data in table 6.1. Table 6.2 summarizes the results.

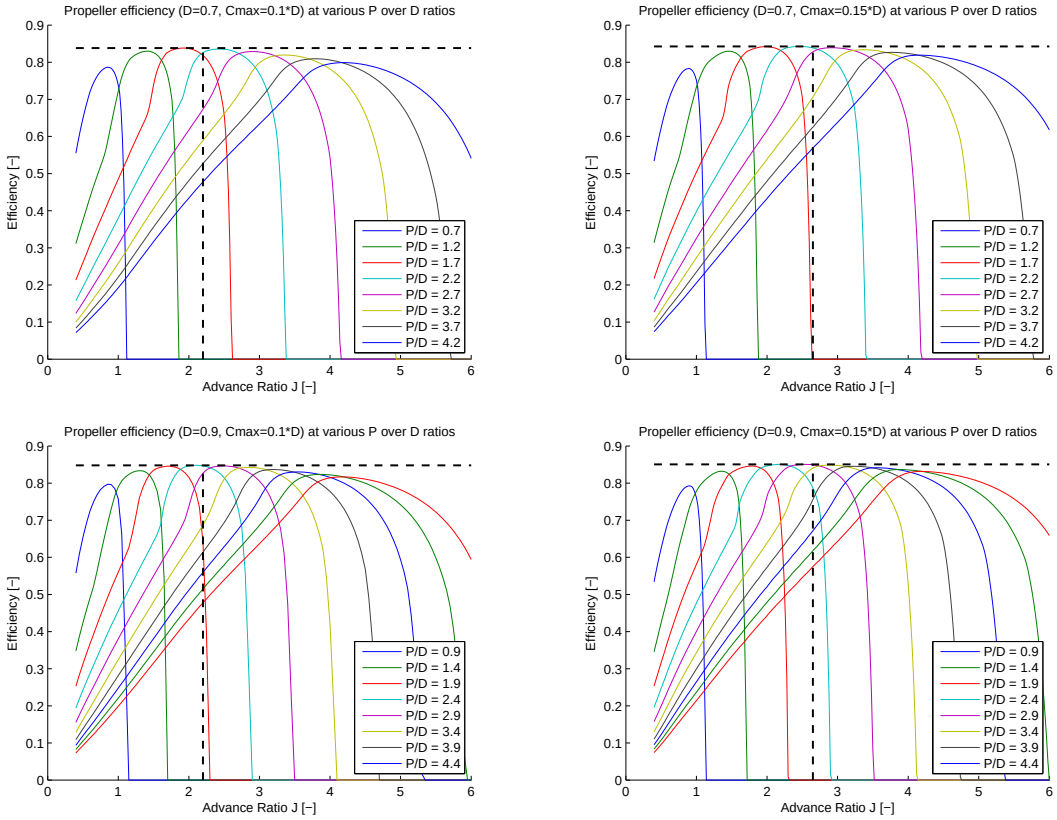

Figure 6.1: Propeller efficiencies for two diameters, 0.7 m and 0.9 m, and two c_{max} values, 10% and 15% of the diameter

The maximum chord is varied from 10% to 20% of the propeller diameter to investigate its influence on the optimum P/D and J values. As an initial planform of the propeller blade, a sinusoidal chord distribution was chosen, with c_{max} at halfway the blade and a tip and hub chord that are half of the maximum chord. This distribution, for a diameter of 0.7 m and a maximum chord of 10%, is shown in figure 6.5. Equation 6.3 describes the shape of this figure, in which the maximum chord length is given by c_{max} and the relative position of the currently analysed blade element is given by r/R.

$$T = c_T \cdot \rho \cdot n^2 \cdot D^4 \qquad (6.2)$$

$$c = c_{max} \cdot \frac{1}{2}\left(sin\left(\frac{r}{R}\pi\right) + 1\right) \qquad (6.3)$$

As can be seen in table 6.1, a maximum chord of 15% yields roughly the same optimum values as a maximum chord of 20%. A maximum chord of 10% gives somewhat different values, this can be explained by the lower values of the Reynolds number and thus the quickly decreasing value of C_l/C_d. Generally speaking, the bigger the propeller diameter, the higher the efficiency is (table 6.1). Therefore, for the same amount of T, the diameter of a propeller with a small chord is bigger than of a propeller with a larger chord, thus the efficiency is highest for the propeller with the smaller chord. This is true until the Reynolds numbers drops too much and the resulting performance drops. Also, a smaller chord

Table 6.1: The optimal J and P/D as function of c_{max} and D

$c_{max} = 0.10 \cdot D$				
D $[m]$	1.10	0.90	0.70	0.50
Pitch $[m]$	3.25	2.55	2.15	1.30
η [%]	85.5	84.5	83.5	82
J [-]	2.35	2.20	2.35	2.05
P/D [-]	2.95	2.83	3.07	2.60
c_T [-]	0.15	0.15	0.15	0.13

$c_{max} = 0.15 \cdot D$				
D $[m]$	1.10	0.90	0.70	0.50
Pitch $[m]$	3.55	3.00	2.45	1.60
η [%]	85.5	85	84	83
J [-]	2.80	2.70	2.80	2.50
P/D [-]	3.23	3.33	3.50	3.20
c_T [-]	0.19	0.19	0.23	0.17

$c_{max} = 0.20 \cdot D$				
D $[m]$	1.10	0.90	0.70	0.50
Pitch $[m]$	3.55	3.15	2.45	1.60
η [%]	85.5	85	84	82.5
J [-]	2.65	2.80	2.80	2.50
P/D [-]	3.23	3.50	3.50	3.20
c_T [-]	0.30	0.32	0.31	0.30

Table 6.2: Efficiency of calculated diameter for 2 bladed propeller at output power of 50 W

	$c_{max} = 0.10 \cdot D$ $c_T = 0.145$ $J = 2.20$			$c_{max} = 0.15 \cdot D$ $c_T = 0.20$ $J = 2.65$			$c_{max} = 0.20 \cdot D$ $c_T = 0.30$ $J = 2.65$		
	D $[m]$	η [%]	n $[rpm]$	D $[m]$	η [%]	n $[rpm]$	D $[m]$	η [%]	n $[rpm]$
1 prop	0.87	84.5	587	0.76	84	599	0.62	83.5	723
2 props	0.52	82	1046	0.53	83	847	0.44	81	1037

results in higher rpm needed and a lower required gear ratio. In terms of efficiency, there is not a big difference between $c_{max} = 0.10 \cdot D$ and $c_{max} = 0.15 \cdot D$.

6.1.2 Performance Final Design

The chosen final design has the highest efficiency, namely the propeller with a 0.87 m diameter from table 6.2. Now the general design parameters are known, the design is evaluated in two plots. The first plot shows the efficiency at different values of V_∞ for a certain T value (figure 6.2). The second plot shows the efficiency at different V_∞ for certain values of advance ratios (figure 6.3).

The final propeller was designed for an output power of 50 W. During cruise a propeller output power of 35.8 W is required. Therefore, for now it was decided to fly at this lower power and accept the fact that the efficiency will be slightly lower. Figure 6.4 gives the range in which the propeller has to operate. At the given power range in the figure, the propeller operates near maximum efficiency which proves that the design is already quite efficient.

6.1.3 Propeller Construction

The propeller will be constructed out of composites to have the highest structural efficiency. In chapter 5, one can find the reasoning behind using the different materials. In contrast to the wing, which is constructed with a D-box and ribs, the propeller blades will be made as a single moulded part. The

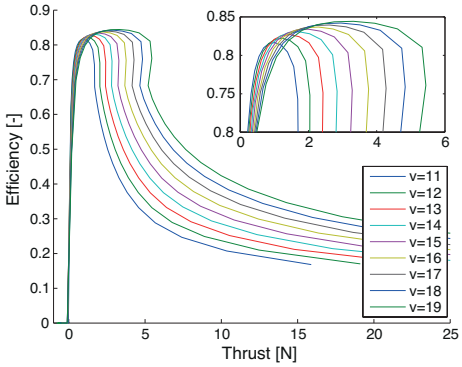

Figure 6.2: Efficiency η at different V_∞ for certain values of T

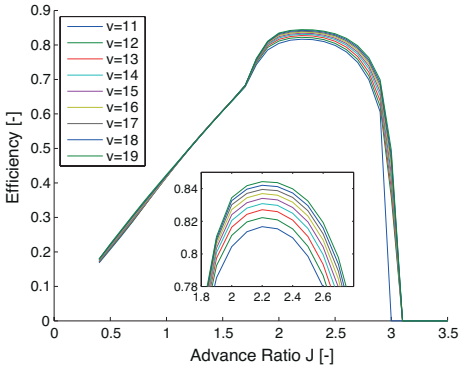

Figure 6.3: Efficiency η at different V_∞ for certain values of J

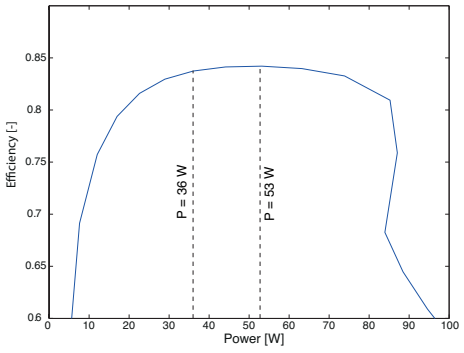

Figure 6.4: Propeller efficiency versus power

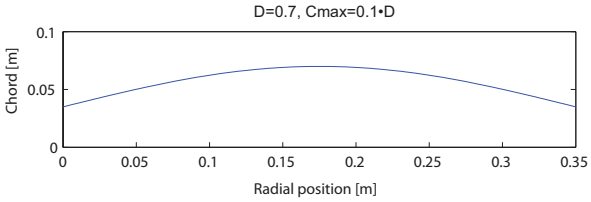

Figure 6.5: Propeller Chord Distribution

main motivations for this are the easier and cheaper production process and the fact that a build up construction (with ribs) probably does not make a lighter construction because of the relatively small dimensions ($c_{max} = 87\ mm$). Compared to the wing, the complexity of the propeller loading makes it more favourable to have a more homogeneous construction. How the single moulded part is built up is explained in the following subsections.

Skins and Core

The skin will be made out of the same material (CFRP) and number of layers as the D-box of the wing. The difference being that only half of the material will be placed in $\pm$ 45° to give the propeller its torsional stiffness. The other half of the fibres will be placed in the span direction of the blade to withstand the bending moment. A simple calculation shows that this is sufficient. The maximum torque on the propeller to drive it is $\pm 1.07\ Nm$ as stated in the next section (section 6.2). Half of this torque is put on each propeller blade, so the maximum bending moment in each blade is $0.535\ Nm$. The root chord of the blade is $33.5\ mm$. The airfoil at the root was changed to a thick NACA 0030 airfoil. The reason was to improve the structural efficiency, aerodynamically this does not matter much since the speed is very low at the root compared to the tip. This airfoil has a maximum thickness of 30% thus an actual thickness of $0.30 \cdot 33.5 = 10.05\ mm$. Assuming an average thickness of $10\ mm$ over

a chord of 15 mm gives roughly an I-beam shape. The carbon layers at $\pm$ 45° are neglected. The two layers in the span direction have a joint thickness of 0.05 mm. The moment of inertia of this beam can be found in equation 6.4. Using equation 6.5, the normal stress in the propeller is calculated. Since the allowable stress is $1,500\ MPa$ the propeller is assumed to be strong enough. It must be noted that only a small strip of 15 mm was assumed while the root chord of the blade is 33.5 mm. Also the $\pm$ 45° layers will help slightly to carry the bending moment. $\frac{2}{12} \cdot 15 \cdot 0.05^3 + 0.05 \cdot 15 \cdot 5^2 = 18.75\ mm^4$ (6.4)

$$\sigma = \frac{M \cdot z}{I} = 142.67 MPa \quad (6.5)$$

The foam core is designed to give reasonable compressive strength for impact (such as landing and folding) and handling, shear stresses due to bending are assumed to be negligible. Rohacell 51, the same material as in the web of the wing spar, is used. Because of the small blade volume, it is not beneficial to use a lighter foam at the cost of compressive strength.

Central mechanism

In the root of the blade, a small aluminium insert will be glued which will be connected to the central mechanism with a hinge. The hinge is designed such that it can only fold the blade backwards. Both the thrust and the centrifugal force keep the propeller open during operation. When the motor is stopped, for landing or in case of a failure, the blade will automatically fold backwards because of the drag of the blade. This feature makes sure the propeller is protected and the aircraft has less drag in its gliding configuration. The central mechanism is simply a T-shaped part of aluminium. The leg, the rotation axis of the propeller, is mounted in bearings and connected to the gearbox. The other two ends will form the hinge pieces to which the aluminium inserts in the blades are connected. A simple spinner is mounted on the central mechanism to reduce the drag. The spinner will be a thin composite shell with a very small mass.

Fuselage

Because the wing is not thick enough to provide enough space for the gearbox and also to make sure the propeller does not get in contact with the leading edge of the wing, a small extension is made in the wing. This small extension will be referred to as the fuselage. This fuselage will have a diameter of 55 mm just after the propeller and will blend into the wing shape. The fuselage will extend 60 mm in front of the wing, this is needed to make sure the propeller is free from the wing. For the centre of gravity it is also beneficial to have some mass in front of the wing to compensate for the tail mass.

6.1.4 Mass and cost

The propeller system has a total mass of 43 g where 27.2 g is taken by the two propeller blades and 15.8 g is taken by the spinner and central mechanism. The total material cost of the propeller system is estimated at €16.65. The largest part of the total cost: labour hours, mold and machining costs, are not taken into account here. Appendix K shows the propeller design result.

6.2 Motor Selection

Because outrunner motors require a smaller gear ratio and are more efficient at lower numbers of revolutions per minute (RPM), an outrunner motor is selected. In the next section, the effect of the

number of windings is explained.

6.2.1 Number of Windings

The ratio between the amount of torque and the number of revolutions per minute can be changed by adjusting the number of windings. Increasing the number of windings decreases the number of revolutions per minute and increases the torque. This means that a motor with a higher number of windings needs only a smaller gear ratio [54]. This is illustrated with the AXI 2212 Gold Line motors in table 6.3.

Table 6.3: Effect of the number of windings on the AXI 2212 Gold Line motor

Motor	**# Windings**	**RPM** $[rpm/V]$
AXI 2212/12 Gold Line	12	1950
AXI 2212/20 Gold Line	20	1150
AXI 2212/26 Gold Line	26	920
AXI 2212/34 Gold Line	34	710

6.2.2 Requirements

The requirements to drive the propeller result directly from the propeller calculations for the power needs: 35.8 W and 53 W.

- Power need for cruise of 35.8 $W/\eta_{prop} \approx 43$ W, advance ratio (J) is equal to 2.4, an RPM of 517.2 rpm and the corresponding torque need is 0.794 Nm (equation 6.1 and 6.2)
- Maximum power for ascent of 53 $W/\eta_{prop} \approx 63.5$ W, an RPM of 564 rpm and the torque need corresponding to this is 1.075 Nm

$\eta_{prop} \approx 83.5\%$ which became clear from the previous section (section 6.1).

6.2.3 Specifications

Next, these values are used to calculate the motor power requirements. A single-stage spur gear gearbox typically has an efficiency of 98.5%. For StratoMAV a two-stage gearbox within the available space in the wing is needed for the required gear ratio. This results in a gearbox with an efficiency of approximately 97% and a maximum power need for the motor of 63.5 $W/0.97 \approx 65.5$ W. The maximum efficiency of the motor should be at a power of 43 $W/0.97 \approx 44$ W. The AXI 2212/34 Gold Line motor satisfies these requirements. This motor weighs 57 g including cables and turns at 710 rpm/V. For a three cell battery system of 11.1 V this results in an RPM_{max} of $7,881$.

Communication with the manufacturer of the motor led to a concept motor in their range. Namely, the AXI 2217/24 Gold Line motor which is about 12 g heavier than the AXI 2212/34 but has a peak efficiency which is 5 to 7% higher, topping at 83% at 50 W. The peak power the motor can deliver for 60 s is 155 W. The motor has a $KV = 700$ rpm/V, resulting in a $RPM_{max} = 7,770$ rpm this reduces the required gear ratio compared to the 2212/34. To be able to control the motor, the Jeti Advance Pro 12 controller is chosen, which has a mass of 9 g. Because the efficiency of the 2217/24 is higher, approximately 7% less power is needed. Adding to that, the gear ratio can be 1.5% smaller.

This corresponds to a decrease in power needed of $\approx 4.5\ W$ which corresponds to a $\approx 400\ g$ decrease in battery weight (section 7.2). Now the motor is known, and with its RPM_{max}, the required gear ratio can be determined.

6.3 Gearbox Design

$RPM_{max} = 7,770\ rpm$, but $RPM_{max_{prop}} = 564\ rpm$ which means a reduction ratio of 13.8:1 is needed. The maximum torque that should be delivered by the motor is then 13.8 times smaller, namely $0.078\ Nm$.

To achieve an efficient and lightweight design of the gearbox, the KISSsoft [55] gearbox design tool was used. The program allows to input the loads put on a certain gear together with the corresponding gear ratio. Furthermore, a spectrum of loads can be defined. In this spectrum one can define the frequency of a certain load, the fraction of the torque and the fraction of the speed during this load. The program then gives a number of possibilities. One possibility is then traded-off on the basis of weight and size. The weight has to be as low as possible and the size needs to be compact to fit in the wing. To be able to meet these requirements, a two-stage spur gear gearbox is designed.

Because the load case for the second stage is higher, the gears are generally larger. Therefore, it was chosen to increase the gear reduction ratio of the first stage to 4.425:1 which then results in a reduction ratio for the second stage of 3.112:1. The material chosen for the gears is aluminium 7075 T6, which is a hardened version of the aluminium 7075 alloy. This is done, to be able to create a low weight solution. The lifetime for which the gearbox has been designed is 5 years, though yearly maintenance is required to check for wear on the gear teeth and bearings. The final efficiency of the gearbox is 97.6%, the estimated mass including bearings is approximately 45 g.

6.4 Conclusion

A propeller with a diameter of 0.87 m and an efficiency of 83.5% is designed to operate efficiently in the high altitude, low density conditions. The weight of the propeller is estimated to be 43 g. To drive this propeller an efficient motor needed to be found. After communication with a motor manufacturer, a low rpm, outrunner motor with a high efficiency is chosen. The efficiency of the motor is 83% at 50 W, having a mass of 69 g. It operates at 700 rpm/V which corresponds to an RPM_{max} in a three battery cell system of $7,770\ rpm$. The RPM_{max} of the propeller is 562.8 rpm which means a gearbox is needed to reduce the RPM_{max} of the motor. A two-stage spur gear gearbox with a transmission ratio of 13.8:1 with an efficiency of 97.6% is designed. The estimated mass with gearbox casing and bearings is approximately 45 g. The total mass of the propulsion system is then 166 g. The overall efficiency of the propulsion system is 67.6%.

Chapter 7

Power System

In this chapter the detailed design of the power system is discussed. First the strategy behind the energy storage system (ESS) sizing is explained. Secondly, the ESS's mass is reduced by performing a sensitivity analysis and developing an optimal route. Thirdly, a battery is selected using a trade-off to find the most feasible type of rechargeable battery. The cost, mass and battery characteristics of the chosen battery are analysed. Moreover, a trade-off is made between different types of thin film solar cells. Finally, the electrical circuit is designed.

7.1 Energy Storage System Sizing

StratoMAV has to make use of sustainable energy, as it needs to stay airborne for a year and cannot carry fuel. StratoMAV's energy source is solar power. However, solar power is not available continuously during a day and its intensity fluctuates. To compensate for these irregularities, a storage system is designed. From a trade-off between different types of energy storage systems (ESS) [21], it became clear that a rechargeable battery system was the most feasible for StratoMAV. In this section, the strategy for calculating the battery capacity and mass is explained.

The battery system has to satisfy certain requirements. The first requirement is that during the day the batteries can be charged by excess solar energy. The second requirement is that the battery must have enough capacity to power the motor, payload, telemetry and avionic systems, during the time that the solar panels cannot deliver enough power.

7.1.1 Solar Irradiation

To satisfy the first requirement, data about the available solar irradiation is needed. It was found that the amount of available solar energy depends on the irradiation of the sun at a certain time. This can be calculated using equation 7.1. Here, θ is incidence angle, which can be calculated with equation 7.2 [25]. The solar constant in equation 7.1 equals $1,372$ (W/m^2). η_{alt} represents the atmospheric loss in irradiation at the considered altitude. At higher altitude, the loss due to scattering and absorbing is smaller, which will result in a higher efficiency.

$$Solar\ irradiation = \cos\theta \cdot Solar\ constant \cdot \eta_{alt} \tag{7.1}$$

$$\begin{aligned} cos\theta = {} & \sin\delta\sin\phi\cos\beta - \sin\delta\cos\phi\sin\beta\cos\gamma + \cos\delta\cos\phi\cos\beta\cos\omega \\ & + \cos\delta\sin\phi\sin\beta\cos\gamma\cos\omega + \cos\delta\sin\beta\sin\gamma\sin\omega \end{aligned} \tag{7.2}$$

In equation 7.2, β is the inclination angle of the solar panel from the horizontal and γ the azimuth angle. The latitude of the chosen location is defined by ϕ. Furthermore, δ is the declination angle and ω represents the hour angle. A graphical visualisation of these angles is in figure 7.1.

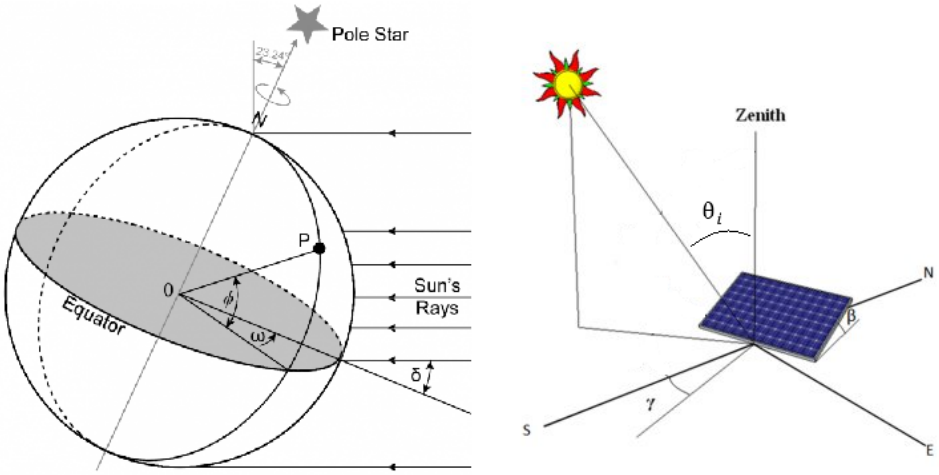

Figure 7.1: Solar angles

The solar panels are integrated into the wing, thus β and γ depend on the curvature of the airfoil and the attitude of the aircraft. However, equation 7.2 is simplified by setting both β and γ to zero, which yields equation 7.3.

$$\cos\theta = \sin\delta\sin\varphi + \cos\delta\cos\varphi\cos\omega \tag{7.3}$$

The only unknowns are now δ, ϕ and ω. The latitude depends on the mission location of StratoMAV. As the contrails are measured in Central Europe, this lies between 35° and 52°. The declination can be obtained with the empirical equation 7.4, where n is the number of the day with $n = 1$ at 1 January 1^{st}. The calculation of ω is straightforward: at solar noon it equals zero and it changes 15° per hour (rotation of the Earth per hour), the hour angle at any time of day can be calculated.

$$\delta = 23.45\sin((284 + n)\,(360/365)) \tag{7.4}$$

Now, the incidence angle and the solar irradiation can be calculated for every latitude at any time of the day (hour angle) for every day in a year (declination).

7.1.2 Battery Sizing Strategy

Now that the solar irradiation can be calculated, the battery can be sized. The battery must have a sufficient capacity to deliver cruise power for a whole night. To ensure that StratoMAV's battery is able to deliver enough power for any day, it is designed for the worst case scenario: the day of the year with the shortest daytime at a latitude with the least solar irradiation. This is on 22^{nd} December for the northern hemisphere, at a latitude of 52°.

During cruise, 35.78 W is required to propel the UAV. The battery has to deliver more power, due to losses from the components of the propulsion system. Their efficiencies are presented in table 7.1. A

safety factor of 5% is applied to the required propulsion power. When integrating the battery power over the time span in which solar energy cannot provide enough energy, a required battery capacity of $1.05 \cdot 10^3\ Wh$ is found. With this capacity, the battery mass can be estimated by dividing the capacity by the specific energy of the battery. A higher specific energy will decrease the mass of the storage system. As mentioned in the Midterm Report [21], a specific energy of 400 Wh/kg has been chosen. Therefore, a battery mass of 2.63 kg is required.

It must be checked if for the worst case scenario enough solar energy can be acquired to propel the aircraft and charge the batteries at the same time. Taking into account a solar cell efficiency of 17%, a solar array area of 2.3 m^2 and energy losses of the solar cells, it was found that there is not enough energy at a latitude of 52° on 22^{nd} December, only on latitudes of 34.4° or lower. The battery mass required is 2.23 kg at a latitude of 34.4°. Note that the required battery capacity and mass also changes with latitude. The relation between mass and latitude is found in figure 7.4; possible solutions lie in the lower left part of the graph. A more detailed analysis is required to determine the optimal ESS design, such that the UAV can also fly at higher latitudes than 34.4°. This sensitivity analysis is presented in the next section.

Table 7.1: Component efficiencies

Component	**Efficiency**[η]
MPPT	0.970
Discharging/charging	0.997
Gearbox	0.960
Propeller	0.835
Converter_1	0.810
Converter_2	0.740
Electric Motor	0.830

7.2 Battery Sensitivity Analysis

In this section, the parameters that affect the ESS mass are analysed. In general, the ESS mass depends on:

- **Cruise power**. During cruise 35.78 W has to be delivered to overcome the drag and generate sufficient lift.
- **Solar module efficiency**. At a certain point in the day, the solar modules take over the function of delivering power from the ESS. The solar module efficiency determines when enough power can be delivered, and thus will affect the ESS mass.
- **Latitude**. The latitude determines the duration of the night. As the ESS has to provide energy during the night, the latitude will have an effect on the ESS mass.

Of course, there are many more parameters that affect the ESS mass, such as the solar array area and the efficiencies of all power train components. However, they have been fixed at values that seem reasonable when compared to reference UAVs, to constrain the design space. Figures 7.3, 7.2 and 7.4 show how the ESS mass varies with each of the three parameters mentioned before. For each graph, two parameters are fixed and one is allowed to vary. From figure 7.2 it can be seen that the ESS mass decreases with an increase in solar module efficiency. However, this decrease is very small. To obtain a decrease of 0.05 kg, the efficiency has to be increased by 15%. Such an increase in efficiency would

greatly increase the cost of the solar module system. Furthermore, such an increase in efficiency will result in thick solar modules which are difficult to implement on a flexible curved wing.

As can be seen in figure 7.3, the ESS mass increases with an increase in cruise power. For a fixed solar module efficiency, latitude and day of the year, the increase is approximately 0.056 $\frac{kg}{W}$. However, decreasing the ideal cruise power requires a change of the UAV configuration or aerodynamics of the UAV, which is not possible in this stage of the design.

Figure 7.4 shows a preliminary analysis of how the ESS mass changes with latitude, for each month of the year. It can be seen that the time of year determines how much the ESS mass increases or decreases for different latitudes. By changing the latitude for the months between April and September results in a decrease in ESS mass up to 0.5 kg, if the latitude is increased. This is because during these months, the nights are shorter at higher latitudes, while at the equator the night time remains approximately constant over the year.

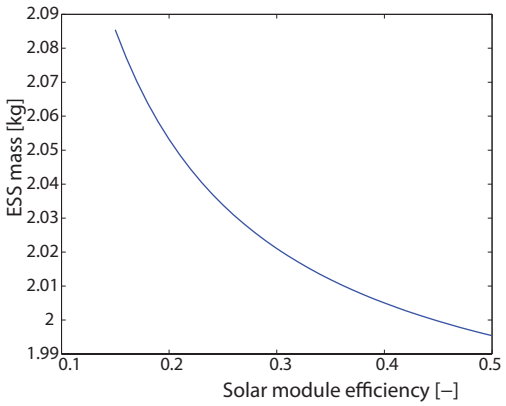

Figure 7.2: ESS mass as a function of solar module efficiency, for a cruise power of 35.8 W, a latitude of 0° at day 356.

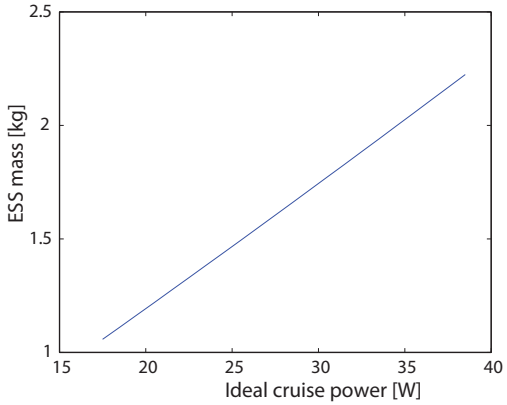

Figure 7.3: ESS mass as a function of cruise power, for a solar module efficiency of 17%, a latitude of 0° at day 356.

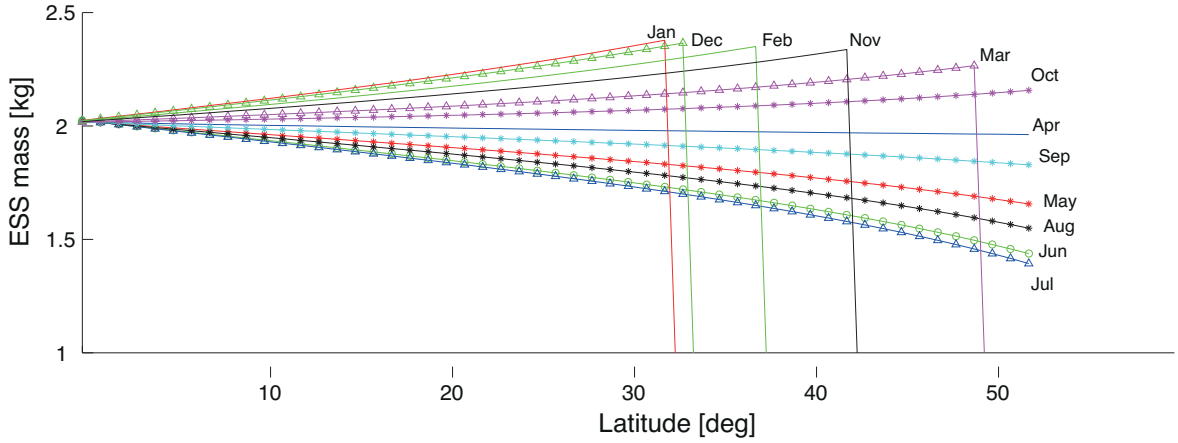

Figure 7.4: ESS mass as a function of the latitude, for an ideal cruise power of 35.8 W, a solar module efficiency of 17 % for all months.

It can be concluded that decreasing the cruise power or increasing the solar cell efficiency are not the favourable solutions to decrease the ESS mass, as they require an extensive design change or greatly increase the cost. Therefore, it is chosen to develop a flying route that changes latitude at the right

time of the year, instead of designing for the worst case scenario. This will result in the lowest possible battery mass.

7.3 Route

As discussed in the previous sections, changing the latitude is the most efficient way to decrease the mass of the batteries. Therefore, a route will be developed that minimises the battery mass.

7.3.1 Calculating the Possible Solutions

First, the battery mass for each combination of day of the year and latitude must be found. This information can be used to find the optimal route, which requires the lowest battery mass. The battery mass is calculated using a MATLAB program, with the solar cell efficiency, the solar array area, the specific energy density and cruise power fixed. The latitude is varied from 0° to 52 °, and for each day the solar irradiation is calculated. For each day, the battery mass required to cruise during night is found, after which is checked if the batteries can be charged during day. The results are plotted in figure 7.5.

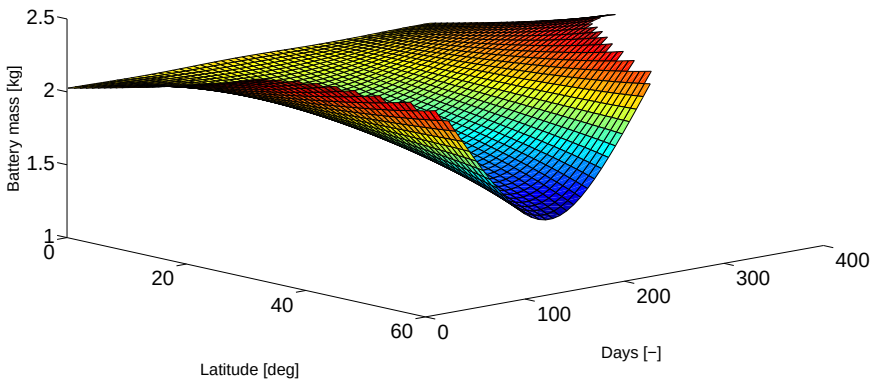

Figure 7.5: Variation of the direction of the vector for which the directional derivative is computed

Figure 7.5 can be used to determine an optimal route. It shows that the required battery mass is minimal at a latitude of 52 ° on day 176. Furthermore, there are two local maxima at the start and end of the year for the regions between 32° and 52° latitude. It is not desirable to fly at these two local maxima, because the high required battery mass, at these two local maxima, will not be used for the rest of the mission. The battery mass that has to be carried on board is equal to the maximum battery mass found on the route; all other points on the route will have an excess battery capacity. It is desirable to fly through the points where the excess capacity is largest, for the following reasons:

- On these points, the battery does not need to be fully recharged during day, which increases their lifetime and performance.
- A part of the battery can be used for operations other than flying, such as downlinking mission information, performing more measurements, thermal control or performing special manoeuvres.

7.3.2 Finding the Optimal Route

To find the optimal route, a convenient starting point is needed. The global minimum in figure 7.5 will be used for this, as it represents the lowest battery mass. To find the next waypoint on the route, the point with the minimum increase in mass must be found. In mathematics, the directional derivative of a multi-dimensional function along a given vector **v** at a given point A represents the instantaneous rate of change of the function, moving through point A in the direction specified by **v** [26]. This means that by using the directional derivative the increase in mass at a given point in all directions can be found. Therefore, the directional derivative will be used to find the direction in which the increase in mass is minimum.

The directional derivative is calculated using equation 7.5. Here $m_\varphi(\overline{\varphi},\overline{t})$ and $m_t(\overline{\varphi},\overline{t})$ are the partial derivatives of the battery mass with respect to latitude and time, respectively, at point $(\overline{\varphi},\overline{t})$ on the surface. Equations 7.6 and 7.7 [27] are used to calculate these partial derivatives. The vector $[\Delta\varphi\ \Delta t]$ represents the direction in which the partial derivative is calculated. Equations 7.6 and 7.7 show that m is assumed to vary linearly between data points. This reduces the accuracy, but also reduces the complexity of the calculation. Accuracy is not of key importance for finding the optimal route since the user of StratoMAV should still be able to flexibly operate it. As it is not of key importance for this problem, this assumption is justified.

$$dm(\overline{\varphi},\overline{t}) = \begin{bmatrix} \frac{\partial m}{\partial \varphi}(\overline{\varphi},\overline{t}) \\ \frac{\partial m}{\partial t}(\overline{\varphi},\overline{t}) \end{bmatrix} \cdot [\Delta\varphi\ \Delta t] = \frac{\partial m}{\partial \varphi}(\overline{\varphi},\overline{t}) \cdot \Delta\varphi + \frac{\partial m}{\partial t}(\overline{\varphi},\overline{t}) \cdot \Delta t \tag{7.5}$$

$$\frac{\partial m}{\partial \varphi}(\overline{\varphi},\overline{t}) = \left.\frac{m(\varphi+\Delta\varphi,t) - m(\varphi,t)}{\Delta\varphi}\right|_{\overline{\varphi},\overline{t}} \tag{7.6}$$

$$\frac{\partial m}{\partial t}(\overline{\varphi},\overline{t}) = \left.\frac{m(\varphi,t+\Delta t) - m(\varphi,t)}{\Delta t}\right|_{\overline{\varphi},\overline{t}} \tag{7.7}$$

The difference between $\Delta\overline{\varphi}$ and $\Delta\varphi$ is that $\Delta\overline{\varphi}$ represents the change in latitude from the starting point to the first adjacent data point. This is used in calculating the partial derivative in point $(\overline{\varphi},\overline{t})$. The parameter $\Delta\varphi$ represents the change in latitude from the starting point to any other data point. This parameter is varied for all latitudes to find the best point.

Since the route should offer flexibility in the use of StratoMAV, the waypoints of the route will be determined for every week. In this way, StratoMAV has enough time to track and measure a contrail and to downlink information, before moving on to the next waypoint. The variable Δt in equations 7.7 now represents one week.

From the starting point, the waypoints should move one week every time. Therefore, the value Δt representing week in equation 7.5 is set to 1, and $\Delta\varphi$, which represents the change in latitude, is varied. Equation 7.5 is used to calculate dm for the complete range of values of $\Delta\varphi$. The minimum value of dm is then selected and the corresponding value of $\Delta\varphi$ is obtained. This value of $\Delta\varphi$, together with $\Delta t\ = 1$, gives the vector in which the directional derivative is minimum. Now, the new waypoint can be calculated by adding this vector to the previous waypoint. This can be done for all data points. The result is shown in figure 7.6. The red line shows the optimal route.

Table 7.2: Overview of where StratoMAV has to fly for all weeks

latitude [°]	**weeks** [-]
0	1-11 and 39-52
52	12-38

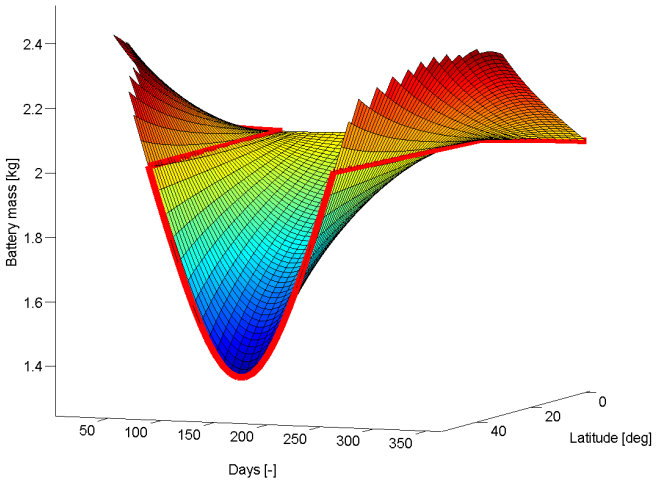

Figure 7.6: Route optimised for latitude and week

Figure 7.6 and table 7.2 show that it is best to fly at a latitude of 0° for the first 11 weeks. After these first 11 weeks, the minimum battery mass occurs no longer at a latitude of 0° but at 52°. StratoMAV then needs to fly to this latitude in one week. It remains there until week 38. It then has to fly back to 0°, again in one week. To check whether this is feasible, the distance it must travel in that week and the cruise speed of StratoMAV must be considered. The circumference of the Earth is approximately $40,075\ km$; therefore, 52° of latitude represents $\frac{40,075}{360} \cdot 52 = 5,788\ km$. With a cruise speed of 18 $\frac{m}{s}$, the travel time becomes 89 hours, or 3.7 days. This makes the above route feasible.

7.3.3 Required Battery Mass

The required battery mass can be obtained from the route described above. This is the maximum battery mass that lies on the route, which is 2.025 kg. This limits the coverage of the mission, as StratoMAV can now only fly in the regions of figure 7.6 where the mass is below 2.025 kg. This area is shown in figure 7.7 and 7.9.

The route has been optimised with respect to the battery mass. Finally, it can be analysed how much excess energy the batteries have for all points on this route. The excess energy left for all points in the (φ, t)-plane is plotted in figure 7.8. In the same figure the optimal route is projected on the (φ, t)-plane. It can be observed that the excess energy has two local maxima: between day 70 and 100 and between day 260 and 290 for a latitude of 0°. Furthermore, a global maximum is reached in the summer at 52° latitude. The planned route goes through these maximum values, which is beneficial, as mentioned before in subsection 7.3.1.

7.4 Battery Trade-off

Now that the battery system is sized and optimised, a battery type has to be selected. There are 3 types of batteries which are suitable for StratoMAV: Lithium Ion (Li-ion), Lithium Polymer (Li-Po) and Lithium Sulphur (Li-S) batteries. The properties of these batteries are presented in table 7.3.

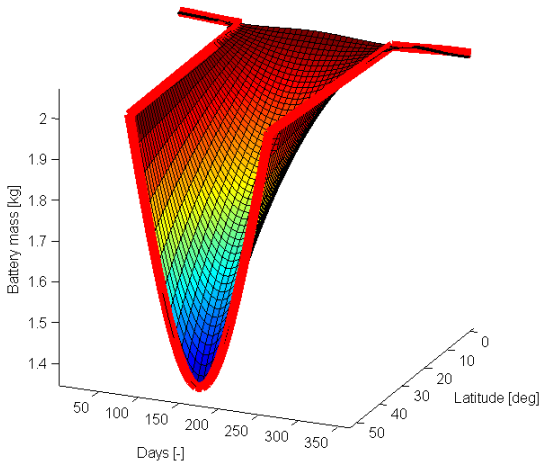

Figure 7.7: Possible flight regions for StratoMAV

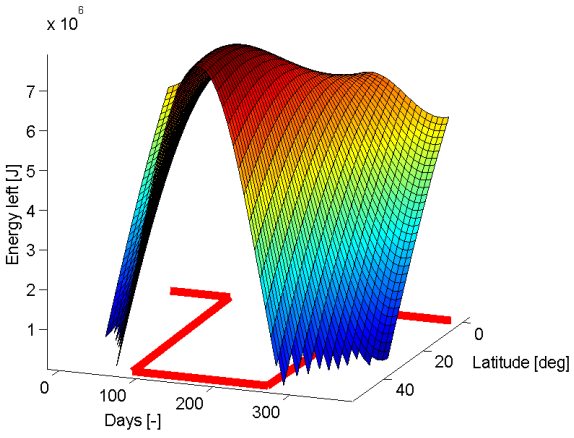

Figure 7.8: Excess energy on the optimal route

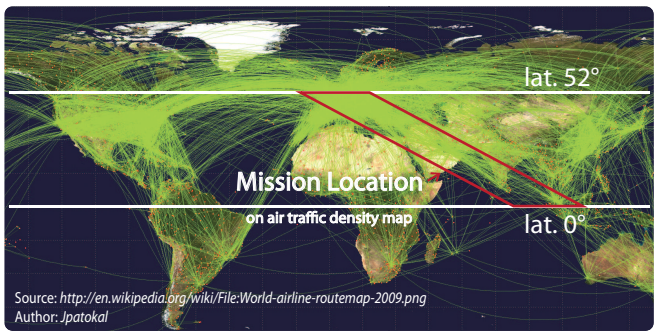

Figure 7.9: Possibe flight regions for StratoMAV project on the world map

Based on these characteristics, a trade-off table (table 7.4) is made to select the most suitable battery for StratoMAV. The energy density and cycle life have a weighing factor of 30% since these two characteristics are the most important. The power density and efficiency have a weighting factor of 10%, as all batteries have approximately sufficient power densities and all batteries have very high (>90%) efficiencies. The remaining parameters are of the same importance and are given a weight of 20%.

The Li-S batteries have a cycle life of only 100 cycles. This means that after 100 charge/discharge cycles the capacity of the battery falls below 80%. Because of this, Li-S batteries cannot be used for StratoMAV. This can also be concluded from the trade off table, as Li-S has the lowest total score. This means that a choice must be made between Li-ion and Li-Po batteries.

The cycle lives of both the Li-ion and Li-Po are sufficient and the charge/discharge efficiencies of these batteries are very high. The biggest advantage of Li-Po batteries compared to the Li-ion batteries is that they have higher power densities. However, the power density of Li-ion battery is sufficient for StratoMAV as well. Li-Po batteries do not have the required energy density of 400 Wh/kg. Higher energy densities are theoretically possible, but to make sure the batteries are available when StratoMAV will be assembled, this is not taken into consideration. Therefore, the Li-Po batteries are graded lower.

From the trade-off table it can be seen that Li-ion batteries have the highest total. In the following section this type of battery will be further analysed.

Table 7.3: Battery Characteristics

	Li-ion	**Li-Po**	**Li-S**
Nominal voltage $[V]$	3.6	3.7	2
Energy density $[MJ/kg]$	0.58	0.47-0.72	0.94-1.44
Energy density $[Wh/kg]$	150-400	130-200	450
Theoretical energy density $[Wh/kg]$	580	400	2,500
Power $[W/kg]$	1,800	3,000+	600
Charge / discharge efficiency	99+%	99.8%	99.5%
Cost $[€/Wh]$	0.19-0.31	0.19-0.31	0.23
Cycle life [#]	300-10,000	500-1,000	100

Table 7.4: Battery Trade-off table

Criterion	Weight	Battery Type		
		Li-ion	**Li-Po**	**Li-S**
Energy Density	30%	3	2	4
Power Density	10%	3	4	1
Cycle Life	30%	5	2	1
Efficiency	10%	5	5	5
Cost	20%	3	3	4
Total score	**100%**	**3.8**	**2.7**	**2.9**

7.5 Lithium Ion Battery Characteristics

Lithium ion batteries are used in a large variety of products. This type of batteries is most popular for portable electronics. They have a high energy density, and are therefore becoming more popular for aerospace applications.

As mentioned before, the best batteries for StratoMAV are Li-ion batteries. There are a lot of companies delivering this type of batteries. After performing a market analysis, it became clear that the company "Envia Systems" makes a Li-ion battery with the desired energy density of 400 Wh/kg. The characteristics of a cell of this battery are displayed in table 7.5 [56]. From this table, the cycle performance can be seen. After 300 cycles, the Envia cells have 91% of their original capacity. This will impose a restriction on the mission profile.

In section 7.3, the total battery mass required for StratoMAV was calculated to be 2.025 kg. With a battery cell mass of 0.365 kg (see table 7.5), this means that $2.025/0.365 = 5.5$ cells are needed, which rounds up to 6 cells. With 6 cells, the total battery mass will be 2.190 kg. With an energy density of 400 Wh/kg and a cost of €0.29/kg, the battery cost amounts to €254.04. If the batteries are replaced every year, the total cost becomes €1270.2.

The capacity retention of the battery cells might cause problems for the long duration mission. With a mission duration of 365 days, a minimum of 365 cycles must be possible. Therefore, a launch date must be selected to cope with this. According to section 7.3, in weeks 39-52 and weeks 1-11 (of the new year) the maximum battery capacity is required to fly. If StratoMAV is launched in week 39, it has its maximum capacity and can therefore fly as the route suggests. In week 11, the battery has not yet reached 300 cycles but will have lost some of its capacity. This is not a problem, since the mass of the battery is slightly higher than the required battery mass from section 7.3. After week 11, StratoMAV flies to another latitude where less energy is required and the capacity retention is no longer a problem.

Table 7.5: Envia cell characteristics

Parameter	Value
Nominal Voltage $[V]$	3-4.2
Capacity $[Ah]$	46
Energy density $[Wh/kg]$	400
Charge/Discharge efficiency [%]	99
Capacity Retention [%]	91% after 300 cycles
Operating Temperature$[^\circ C]$	-10 − 60
Dimensions (w·h·d) $[cm]$	9.7·1·19
Mass $[kg]$	0.365
Cost $[€/Wh]$	0.29

7.6 Thin Film Solar cells

From a trade-off in the Midterm Report, it became clear that thin film solar cells are the best option for StratoMAV, due to their relatively low mass to area ratio (in kg/m^2) when compared to thick crystal solar cells. It is found that there are four different types of thin film (TF) solar cells with efficiencies ranging up to 28%. The first type consists of Silicon solar cells, which can be amorphous (a-Si) or crystalline (c-Si). The second type consists of Copper Indium Gallium Selenide solar cells; third is Cadmium Telluride and last is Gallium Arsenide. A trade-off needs to be performed to select the best TF solar cell. The selection will be based upon the following characteristics: efficiency, mass, cost and sustainability.

The TF solar cell properties are presented in table 7.6. It can be seen that GaAs has by far the highest efficiency, but is also the most expensive. Note that the solar cell efficiencies are measured under laboratory conditions. The solar module efficiency will be lower, which should be taken into account during calculations. The prices of the solar module are production costs, which do not equal the selling price. The mass to area ratio is around the 300 $\frac{g}{m^2}$ for all TF solar cells, but with a higher efficiency, the used area will be smaller.

Table 7.6: Thin film properties

TF solar cell	Efficiency	g/m^2	Sustainable	$€/W$
a-Si	13.4	260-320	high	0.62
c-Si	20.1	270-320	high	0.64 [57]
CIGS	20.3	-	medium	0.74 [58]
CdTe	18.3	-	low	0.56 [59]
GaAs	28.8	250-300	low	0.90

GaAs and CdTe score very low on sustainability. Cadmium is a heavy metal which can become an environmental hazard when it leaks into the soil, and telluride is rare material. The Gallium Arsenide cell contains toxic and unsustainable arsenide. CIGS solar cells score average, due to the fact that they only contain a small amount of cadmium. TF silicon solar cells score the best on sustainability, because the silicon is abundantly available and recyclable.

A trade off is made to choose the most suitable thin film material, shown in table 7.7. The weighting factor is 40% for mass, as this is a driving requirement for the UAV. Efficiency weighs 25%, as a higher efficiency can reduce solar area and thus mass. Sustainability is given a weighting factor of 20%, since the PV materials used in the solar cell should not be a burden to the environment. Cost is given a

weighting factor of 15%, as it is the least driving factor. A scoring system of 1 to 5 is used, where 5 is the best score.

It becomes clear that TF c-Si has the best overall score. An often used TF c-Si solar cell called Silicon Solar Space Cell S-32 will be used for StratoMAV. The S-32 has an efficiency of approximately 16.9%. The specification sheet for the S-32 solar cell can be found on the Azure Space company website [60].

Table 7.7: Solar Cells Trade-off table

Criterion	Weight	Thin film type				
		a-Si	**c-Si**	**GaAs**	**CIGS**	**CdTe**
Weight	40%	4	4	4	4	4
Efficiency	25%	2	4	5	4	3
Sustainability	20%	5	5	1	2	1
Cost	15%	4	4	1	3	5
Total score	**100%**	**3.7**	**4.2**	**3.2**	**3.45**	**3.3**

Now that the solar cell has been selected, it still needs a coating to protect it from environmental influences. Some properties that this coating should have, are a high reflectance, preferably flexible, lightweight and low in degredation. A coating that satisfies these properties is the Dupont Teflon fluoropolymer coating. The mass to area ratio of this coating is 117 $\frac{g}{m^2}$[61], which is very lightweight when compared to a glass coating which are approximately 780 $\frac{g}{m^2}$. The total required coating mass then becomes $117 \cdot 1.725 = 201.83\ g$.

7.7 Electric Circuit Design

Now that the batteries and TF solar cell have been selected, the electrical circuit and components can be designed. First, all the subsystems and components are identified with the help of an Electrical Block Diagram, which is presented in figure 7.10.

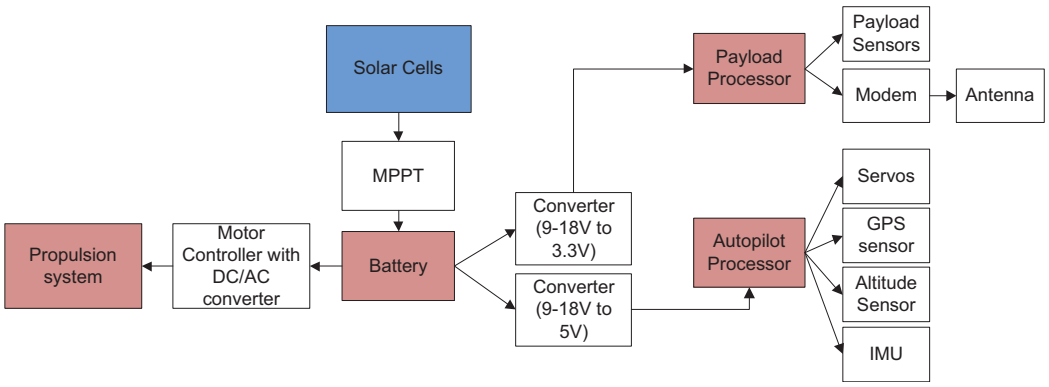

Figure 7.10: Electrical Block Diagram

In the block diagram it can be seen that the energy is first generated in the solar module. Then, a maximum power point tracker (MPPT) finds the current and voltage where the power is maximum. The MPPT is connected to the battery, which is linked with multiple subsystems. The battery has to power the electric motor, the payload, the telemetry system and the avionics. Between the battery and electric motor a DC-AC converter has to be placed, because the chosen electric motor works on

AC. Between the battery and each remaining subsystems an individual DC-DC converter is placed to match each subsystem voltage.

The first step in the circuit design is to match the voltage of the battery to the voltage of the electric motor. The battery has a mean cell voltage of 3.7 V. If the cells are placed in series, the voltage adds up; if they are placed parallel, the currents are added. The electric motor works on a voltage of 11.1 V, so it is chosen to have a string of 3 battery cells in series and 2 strings in parallel. This design will lead to a battery pack with a mean voltage of $3 \cdot 3.7 = 11.1$ V. Electric motors are usually such designed that their voltage is a multiple of the mean output voltage of the battery. This is why the mean voltage of the battery pack matches with the input voltage of the electric motor.

The next step is to choose the configuration of the solar cells. A S-32 thin film solar cell has an area of 23.61 cm^2. The wing area is 2.38 m^2, but not the entire wing area can be filled with solar cells. It is assumed that 75% of the wing area can be used, which equals 1.725 m^2. The number of solar cells required then becomes 730. With a solar cell mass of 320 g/m^2, this gives a total mass of 552 g.

Now the configuration of these solar cells and solar modules must be determined to achieve a certain mean voltage and current output of the solar modules. The module voltage must be higher than the maximum voltage of the battery, to be able to charge the battery. The battery delivers a maximum voltage of $3 \cdot 4.2 = 12.6$ V when fully charged. To achieve a higher voltage than 12.6 V, some solar cells must be placed in series. The solar cells have a maximum power point voltage (MPPV) of 528 mV. However, the solar cells cannot operate at this MPPV all the time, due to varying light intensity and due to the efficiency of the MPPT. Therefore, a safety margin of 5% is taken for the MPPV of the solar cell. So the worst case MPPV voltage will be 475.2 mV. The same holds for the maximum power point current (MPPI) which will be 1.012 A.

A certain nominal voltage will give a combination of cells in series and parallel. Typical off the shelf solar modules have nominal voltages of 12 V and 24 V. However, S-32 solar cells are sold separately, thus the module and voltage can be customly designed. The amount of solar cells in series and parallel are calculated as follows.

- The daily Available mean sun hours (Ams-hours) requirement equals the energy capacity divided by the nominal voltage.
- The required current is the daily Ams-hrs divded by the equivalent sunlight hours.
- The current per module is the required current divided by the amount of solar modules.
- The amount of parallel solar cells is the current per module divided by MPPI.
- The amount of serial solar cells is the nominal voltage divided by MPPV.

From the calculations above, it was found that to obtain the required amount of solar cells, more than 2 modules must be used and connected in parallel. For 1 and 2 modules the amount of 730 solar cells cannot be achieved for nominal voltages up to 24 V. Since every module needs a separate MPPT, the mass will increase by using more modules. Therefore, 3 solar modules will be used. This results in a configuration of 49 solar cells in series and 5 in parallel for every module, at a nominal system voltage of 23 V. The selected configuration of the solar modules is visualised in figure 7.11.

Now that the solar module is designed, some effects to be taken in consideration. Once a solar cell is in use, its power output will decrease due to degradation of the solar cell. There is a short term power loss which is due to a physical process in the solar cell and a long term loss due to weathering and degradation of the module package. It is seen that solar cells have a short term power loss of 2.4% and a annual loss of 0.2% per year [62]. After a year the solar module will have an efficiency of

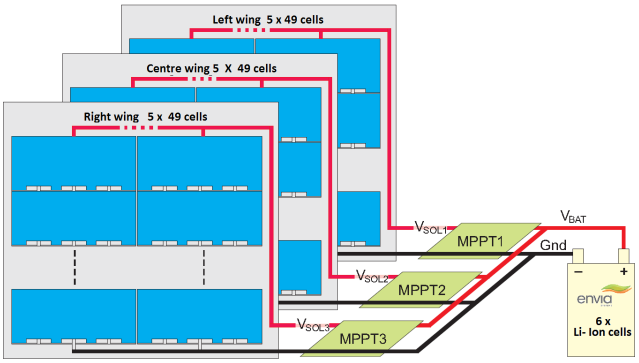

Figure 7.11: Configuration of the solar modules

$16.9 * 0.974 = 16.46\%$, this is not a significant loss. This will not endanger the power system during the flight mission, but should be repaired during maintenance after a year.

Now the amount of solar modules are known, a MPPT must be selected. Due to the increasing PV market there are a lot of supplier of MPPTs. The MPPT will be selected based on the max power delivered by the solar modules. The maximum power delivered by the solar modules can be calculated using equation 7.8;

$$P_{Max} = (MPPV \cdot \#cells_{serie}) \cdot (MPPI \cdot \#cells_{parallel}) \tag{7.8}$$

Using equation 7.8 with $MPPV = 0.528\ V$ and $MPPI = 1.012\ A$ the maximum power delivered by the solar modules is 130.9 W. After a survey of the market research some MPPTs are found with weights ranging between 180-200 grams. As previously mentioned 3 MPPTs will be used. This will make the total MPPT mass too much. But, most of the found MPPTs are designed for fixed applications and are therefore not optimized for low weight. These MPPTs use casings which makes the MPPT heavy. Therefore some MPPTs of solar aircraft and solar cars are analysed to get an idea about the weight of the MPPT for mobile applications where weight reduction is important. In figure 7.12 [28] a graph can be seen of the max power vs mass. By using the regression formula an indication of the MPPT weight for StratoMAV can be obtained. For a maximum power of 130.9 W a weight of 55.3 g is assumed to be possible. This weight can be obtained by designing a MPPT specifically for StratoMAV. At the design of the MPPT the various components must be identified. The MPPT consists out of a DC-DC converter with adjustable gain controlled by a micro controller. The input of the controller is the measured output voltage and current of the solar panel. Thereafter the MPPT controller executes an algorithm to find the MPP. The output of the controller drives the DC-DC converter's switching device which regulates the output voltage. The design of a MPPT is a project on its own and will therefore not be treated in detail. The designed MPPT would have the specification listed in table 7.8.

One of the final steps was to choose compatible DC-DC converters for the remaining subsystems. All converters are required to have a voltage input of between 9 V and 12.6 V, because the battery voltage varies between 9 V to 12.6 V . The output voltage however depends on the subsystems voltage. So in order to chose the converters, the voltages of the subsystems have to be known, the values are found in table 7.9. From this table can be seen that the subsystems require either 5 V or 3.3 V. This means that 2 DC-DC converters are needed. After market research 2 appropriate converters are found. The characteristics of these converters can be seen in table 7.10. Since these components are crucial and lightweight, redundancy is applied by adding two backup converters.

The final step is estimating the cable weight that is necessary for the power system. From American

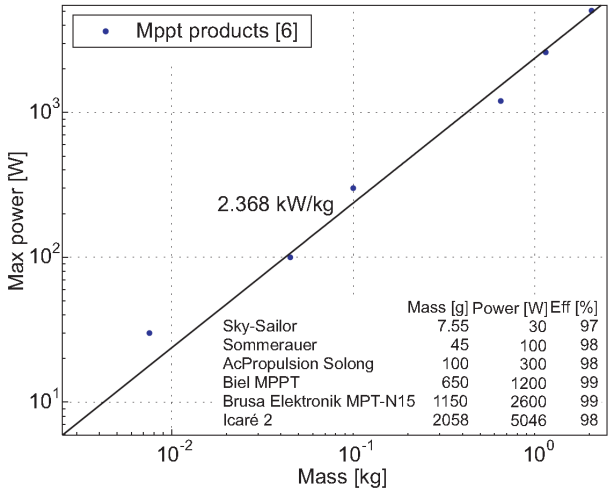

Figure 7.12: Power to Mass ratio of high efficiency MPPTs

Table 7.8: MPPT properties

Characteristic	**Value**
Maximum Power input $[W]$	130.9
Maximum Voltage input $[V]$	26
Electrical efficiency [%]	97
Tracking efficiency [%]	99+
Operating Temperature $[°C]$	-40 − +80
Weight $[g]$	55

Wire Gauge (AWG) table [63] a selection is made for the required copper cable diameter. The selection is based upon the maximum current going trough the copper cables. The solar modules have a maximum power of approximately 130 W and a corresponding voltage of 23 V, this means that a maximum current of $130/23 = 5.69$ A will go through the cables. To overcome a maximum current of 5.69 A an AWG value of 22 is found. A cable with an AWG value 22 has a mass of 7.44 g/m [64] . These cables are used to connect the solar modules with the batteries. The wing span of StratoMAV is around 6.8 m, if in the worst case the modules are placed at the wing tips and the batteries are placed in the middle of StratoMAV the cables have a maximum distance. This means that one module will have a cable length of $6.8/2 = 3.4$ m, but it needs to be connected twice. So a total cable length of 6.8 m is required for the solar module on the left wing, while this amount is also needed for the module on the right wing. The middle solar module will have a approximately a total cable length of 3.4 m. There also has to run a cable from the battery to the engine, which is also around the 3.4 m. The total cable length is around $2 \cdot 6.8 + 2 \cdot 3.4 = 20.4$ m, and the total mass is $20.4 \cdot 7.44 = 151.7$ g.

Table 7.9: Subsystem electrical properties

Subsystem	**Voltage** $[V]$	**Power** $[W]$
Payload sensor	5	0.03
Payload thermal sensor	3.3	0.92
Telemetry	3.3	0.05
Avionics	5	0.3

Table 7.10: Properties chosen DC-DC converters

	XP Power IZ1205SA	**XP Power JCA0212s03**
V_{in} $[V]$	9-18	9-18
V_{out} $[V]$	5	3.3
I_{out} $[A]$	0.6	0.6
P_{out} $[W]$	3	2
Working Temperature $[°C]$	-40 − +70	-40 − +75
Efficiency[%]	81	74
Weight $[g]$	4.5	13
Cost [€]	13.96	15.07

7.8 Conclusion

It can be concluded that the battery system that was designed for the worst case scenario was not feasible, mainly due to its high mass of 2.63 kg. The battery weight is reduced by planning a route for StratoMAV. It was computed that StratoMAV has to fly at latitude 0° between weeks 1-11 and 39-52, and fly at latitude 52° between weeks 12 and 38, to obtain an optimum route with respect to battery mass. A lithium ion battery with a specific density of 400 $\frac{Wh}{kg}$ is chosen and he battery weight is reduced to 2.19 kg. From a trade-off between thin film solar cells, S-32 thin film c-Si from Azure Space turns out to be the best option. The coating used on the S-32 solar cell is a teflon fluoropolymer coating from Du Pont with a total mass of 202 g. The solar cell mass without coating is 552 g. Finally, the electrical circuit has been designed, resulting in 3 solar modules. Each solar module has mean power output of 130 W. Two converters are chosen, one with a stepdown ratio of $1.8 - 3.6$ with an efficiency of 81% and another with a stepdown ratio of $2.7 - 5.5$ with an efficiency of 74%. For each converter a redundant converter is added to increase the reliability of the power system. Three custom-made MPPTs will be used to reduce the weight of the power system, which have a total weight of 165 g. The cables to connect the power system has a mass of 151.7 g.

Chapter 8

Payload and Science Mission

This chapter deals with the payload carried aboard StratoMAV. The payload sensors perform the scientific mission which is to investigate the regional effects of contrails on the ground surface temperature. The details of the science mission and the characteristics of the chosen sensors are discussed here. Finally, the payload configuration together with the chosen flightpath and the requirements on other subsystems are presented.

8.1 Science Mission

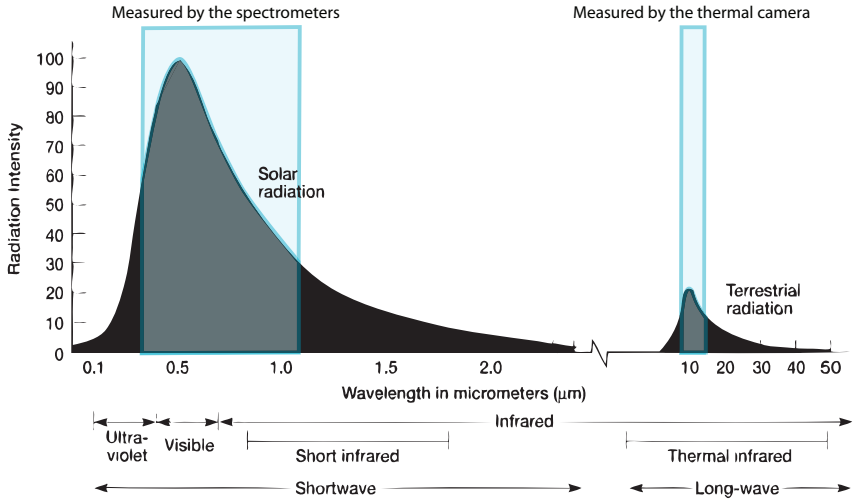

Figure 8.1: Solar and terrestrial radiation measured by the payload sensors

The radiation flux of contrails is measured at day and night to find out which effect of contrails is larger: blocking incoming sunlight during day, or trapping radiation emitted from the Earth during day and night, see figures 8.2 and 8.3. The first would mean that contrails have a cooling effect on the ground temperature, while the latter would mean that contrails have a warming effect. The differences in wavelength ranges and energies between solar and terrestrial radiation are shown in figure 8.1, adapted from [65]. The solar radiation is measured by two spectrometers; one measures in the range 340-750 nm and the other in the range 640-1050 nm. For the long-wave terrestrial radiation measurements at night, the thermal camera measures in the range of 7.5-13.5 μm. These sensors cover the peaks of the solar and terrestrial radiation, see figure 8.1. It is assumed that by measuring the peaks containing

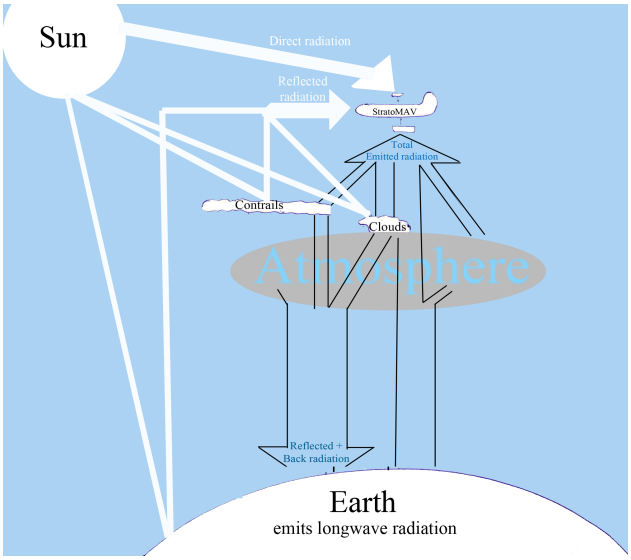

Figure 8.2: Total radiation measured by StratoMAV at day. This is broken down into reflected solar radiation, emitted radiation from cloud, contrails, Earth and atmosphere

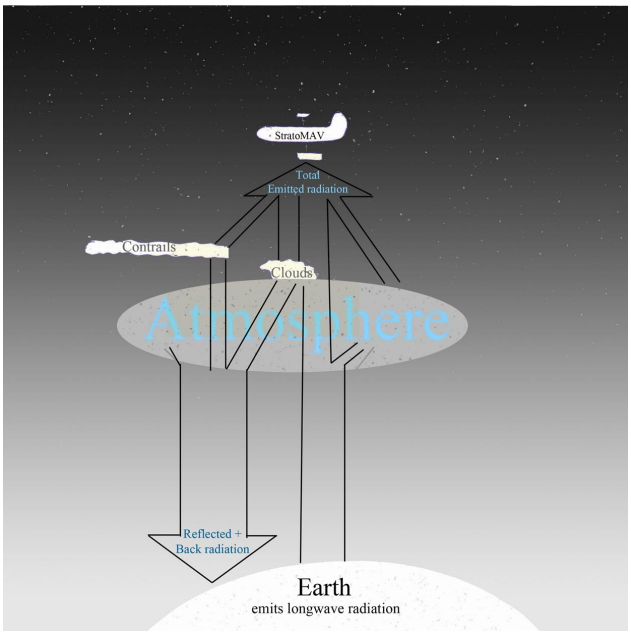

Figure 8.3: The radiation measured by StratoMAV at night, consisting mostly of long-wave radiation

the most energy, it can be determined whether contrails have a significant impact on regional surface temperatures.

The measured radiation data will have to be compared to other data: the incoming solar radiation at the time of the measurements and the background radiation (from the ground and clouds underneath the contrails). The incoming solar radiation is modelled from satellite data packages, as sufficient knowledge is available about the atmospheric composition and the amount of sunlight depending on the location and day of the year. The background radiation is measured by a second set of sensors that are set at an angle to measure directly next to the contrails.

Before measurements can be taken, contrails must be found. Contrail detection is done automatically on board with the use of a pattern recognition algorithm, which is applied to the thermal camera images. Therefore, the thermal camera is used for both contrail detection and radiation measurements. Taking measurements on all contrails is hard to achieve with only one UAV and requires extreme UAV capabilities. Satellites are a lot more suited to take measurements on a large amount of contrails in a large area at the same time. Therefore, the main goal is to take regular measurements throughout the growth and extinction of a contrail on its radiative properties, which can supplement static satellite data which lacks the temporal resolution provided by StratoMAV. A typical contrail detection and radiation measurement scenario is given at the end of this chapter.

8.2 Sensors

This section describes the properties of the chosen sensors in detail. The field of view is calculated, as well as the spatial resolution at contrail height, the frame rate and power consumption.

8.2.1 FLIR Quark Uncooled Thermal Core

The FLIR Quark thermal camera core is used to detect contrails and to measure the emitted thermal radiation from contrails at night. On the FLIR website several lens options are given with their properties [66]. A choice must be made between the Quark 640 and the Quark 336, which have the same weight and mostly the same specifications, except for their sensor size, field of view (FOV), cost, and a small difference in power consumption. An example calculation is performed for the Quark 336, which has a sensor size of 336 x 256 pixels, and the smallest lens; the results for the other lenses are given in table 8.1. The smallest lens has a 13 mm diameter and FOV (H x V) of 24° x 19°. With an altitude difference of 4 km between StratoMAV and the contrail (15 km StratoMAV altitude - 11 km target contrail height), the horizontal width at contrail height is $4,000\ m \cdot tan(24°/2) = 850\ m$. To find the pixel width at contrail height, the previously calculated width is divided by half the amount of pixels on the horizontal side of the sensor: $850\ m/168\ px = 5.1\ m/px$. The same calculations are performed for the vertical direction, with a $FOV = 19°$, and half the vertical sensor size of 128 px: $4,000\ m \cdot tan(19°/2) = 669\ m$ (see figure 8.5), and $669\ m/128\ px = 5.2\ m/px$. A check is performed from the instantaneous field of view (iFOV) which is 1.308 $mrad$ for the 13 mm lens. For an altitude difference of 4 km the contrail pixel size equals $4.0 \cdot 10^3\ m \cdot 1.308 * 10^{-3}\ rad = 5.2\ m/px$.

Table 8.1: FLIR thermal core lens properties

Lens size	**13 mm**	**14 mm**	**17 mm**	**19 mm**	**35 mm**
Pixel size at contrail (m), Quark 640 and 336	5.2	**4.8**	4.0	3.6	2.0
Width of area (m), Quark 640	3,314	**3,152**	2,600	2,295	1,268
Length of area (m), Quark 640	2,676	**2,522**	2,070	1,848	982
Width of area (m), Quark 336	1,700	1,628	1,338	1,124	650
Length of area (m), Quark 336	1,338	1,268	1,052	912	496

To make a trade-off between the Quark 640 and the Quark 360, as well as the possible lenses, table 8.1 is used. To recognise contrails, the largest FOV is advantageous for the pattern recognition algorithm that finds linear contrails. It is quite sufficient to recognise contrails with the lowest possible resolution (5.2 m per pixel at contrail altitude). A minimum contrail width of 100 m should be recognisable, meaning that 19 px of 256 px in the worst case of the Quark 336 will cover a contrail, and 40 px of 512 px for the Quark 640. When a contrail grows wider than 100 m, the algorithm might not recognise the contrails as linear stripes, especially with the Quark 336. Since the spatial resolution and weight are the same for both sensors, Quark 640 will ease pattern recognition for linear contrails. The Quark 640 is chosen for its larger sensor size (640 x 512 px) and larger FOV, while the Quark 336 has 336 x 256 px and half the FOV. The smallest lens has sufficient spatial resolution and FOV, but is not the lightest option. From table 8.1 the lightest lens is the 14 mm lens: the total combination weighs 21.5 g. Its spatial resolution (4.8 m/px) and FOV are sufficient (resulting area: $3,152\ m$ x $2,522\ m$) for the contrail detection with Quark 640. The sensor-lens combination has a price of €6,384.

8.2.2 Hamamatsu Spectrometers

The Hamamatsu mini-spectrometers C10988MA and C11708MA measure the reflected visual and near-infrared (solar) contrail radiation at day. Since there is only thermal emission at night, the spectrometers only operate at day. Similar calculations are made for the spectrometers as for the thermal camera to determine the FOV and width of the measured area at contrail height.

In the specifications the FOV is not given, but the numeric aperture is given as a solid angle of 0.22 (steradians). To find the half angle of the solid angle cone, equations 8.1 to 8.3 are used. The half

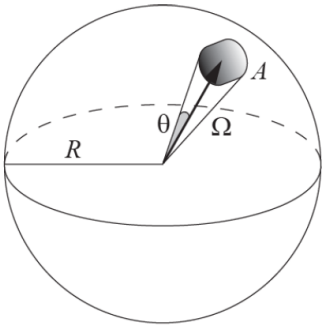

Figure 8.4: Illustration of the solid angle

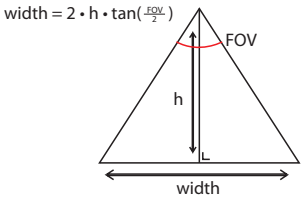

Figure 8.5: Calculation of measured area dimensions

angle is used as the sensor FOV. The solid angle is a 3D angle which relates the area of the solid angle cone to the area of sphere with radius R with equation 8.1 (also shown in figure 8.4 [67]). The area projected by the cone (A) on the sphere is described in terms of cone half angle (θ) as in equation 8.2. Using the two previous equations, the solid angle can be rewritten in terms of the cone half angle as in equation 8.3, where Ω is the solid angle, A is the area on the sphere of radius R and θ is the half angle of the cone related to the solid angle. The solid angle is 0.22, which is used in the previous equation to find the half angle θ, the result is 15.2°.

$$\Omega = \frac{A}{R^2} \qquad (8.1) \qquad A = 2\pi R^2(1 - cos\theta) \qquad (8.2) \qquad \Omega = 2\pi(1 - cos\theta) \qquad (8.3)$$

Now, the total field of view is $2 \cdot 15.2° = 30.4°$. With an altitude difference of 4 km between the sensor and the contrail, and the sensor size of 256 px (linearly placed), the resulting width of the measured section equals: $2 \cdot 4,000\ m \cdot tan(15.2°) = 2,174\ m$ (see figure 8.5). Given that the slit size of this sensor is 75 x 750 μm and the field of view is 30.4°, the field of view in the length direction is one tenth, or 3.04°. Taking an altitude difference of 4 km between the sensor and the UAV, the measurable contrail width equals $2 \cdot\ 4,000\ m \cdot tan(1.52°) = 212\ m$.

8.3 Processor and Data Storage

Because the payload requires power for the image processing and contrail tracking, a processor is required. The autopilot board contains a processor, but it carries out the flight control calculations and the power control calculations (hill climbing and maximum power point software); see also chapter 10.4.1. The amount of operations per second required for the autopilot is difficult to estimate; therefore, the processing power available for the payload is unknown. Since image processing is resource consuming, another more powerful processor is needed, which also serves as a back up to perform vital functions in case the autopilot processor fails. The selected processor is a Texas Instruments TMS570LS1224, which is described as a "high performance automotive grade microcontroller for safety critical applications" on the Texas Instruments website [68], where the specifications can be found. The payload processor features a 180 MHz system clock, 192 KB RAM, and 1.25 MB flash memory. The average power consumption is calculated from its data sheet [68]. The recommended core supply voltage (V_{CC}) is 1.2 V, the I/O voltage (V_{CCIO}) is 3.3 V, the core current (I_{CC}) is 350 mA and the I/O current (I_{CCIO}) is 15 mA. This results in a power consumption of $V_{CC} \cdot I_{CC} + V_{CCIO} \cdot I_{CCIO} = 1.2 \cdot 350 + 3.3 \cdot 15 = 470\ mW$. For the data storage, two microSD cards selected (one serves as a backup). The chosen cards are SanDisk Extreme Pro© microSDHC UHS-I cards with a data capacity of 16 GB each.

8.4 Flight Path and Sensor Placement Options

Different combinations of spectrometer placement and contrail measurement flight paths have been considered in figure 8.6. During measurements, radiation data of contrails and the nearest background is required. Option 1 would measure too much background radiation together with the contrail radiation. Option 3 is very inefficient because of the required turns. The same applies to Option 2, but less mass is needed for the sensors. Option 4 is both lightweight and does not require turning; therefore, this option is chosen. Two sets of spectrometers are required, making the total four. To achieve an acceptable payload mass, the ultra compact spectrometers of 9 g are selected. One set of sensors points straight down to measure the contrails, the other set is tilted 3.04° to measure the background.

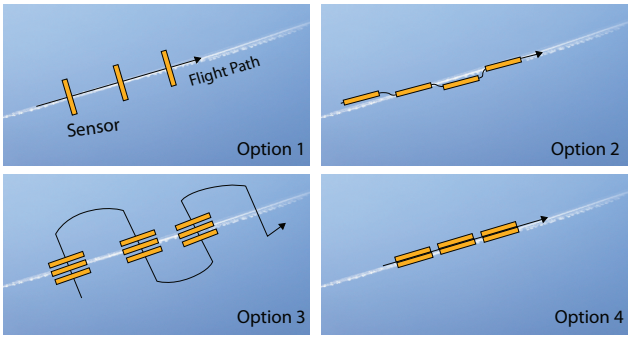

Figure 8.6: Spectrometer placements relative to flight paths that were considered

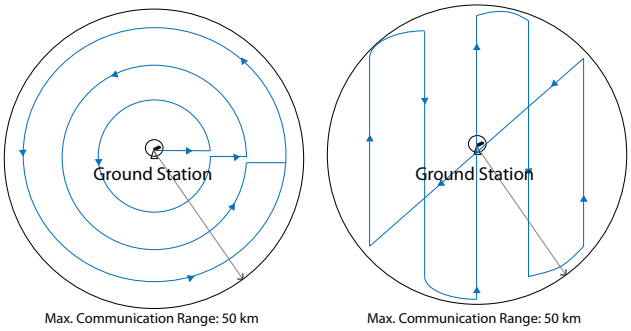

Figure 8.7: Optional flight paths to take contrail measurements

8.5 Thermal Camera Frame Rate (Contrail Detection Sensor)

At the cruise speed of 18 m/s, StratoMAV travels $1,080$ m/min. The Quark Product Specification [69] lists the possible frame rates for different configurations, and it is found that the minimum frame rate for PAL is 8.33 Hz. However, a lower rate might be preferred, as not all data is needed. There will be a lot of overlap in the data and time for processing is needed. Lowering the output frame rate might be achieved through serial command of the sensor, freezing an image, or immediately clearing the buffer when data is not needed at the moment. Changing the frame rate does not affect the power consumption (see section 8.7). Since StratoMAV is cruising at $1,080$ m/min and the measured contrail area per frame is $3,152$ $m \cdot 2,522$ m, 1 frame per 2.3 minute would be required to have no overlap in the data if the contrail is static. In the worst case scenario, the contrail is moving at 20 m/s in the direction opposite to StratoMAV's flight path. Dividing the shortest side of the frame which is $2,522$ m by a 40 m/s worst case relative velocity of the contrail gives a maximum of 63 s before the next frame should be taken. However, this does not take processing time or transmitting time into account and some overlap would be desired for contrail tracking and error detection in the measured data. This is decided by the available processing time on board. Additionally, blurring should be taken into account when considering the frame rate.

Blurring With a frame rate of 8.33 Hz the integration time per frame equals $\frac{1}{8.33} = 0.12$ m/frame. In that time, at $V = 18$ m/s, the UAV has moved $\frac{18}{8.33} = 2.16$ m/frame. With a resolution of 4.8 m/px at contrail height, this means that the frame has moved less than half a pixel during the integration time.

A frame rate of 8.33 Hz will therefore not pose a problem to the contrail detection algorithm when it comes to blurring.

Processing Time As previously described, in the worst case when the contrail is moving away in perpendicular direction from the UAV, one minute of total processing time is available. In that time the frame should be stored, the contrail detection should be performed to determine contrail presence, if so the flight path should be adjusted and another frame should be taken to determine the heading of the contrail. The latter is assumed to take less than contrail detection time, because a simple check could be performed around the pixels where the contrail was detected in the frame. With these requirements in mind, the processor performance of StratoMAV should be looked at in further research.

8.6 Spectrometers Frame Rate (Solar Radiation Sensors)

The longest integration time of $10,000$ ms is taken to capture the most light. This is necessary to accurately detect the difference in background radiation and contrail radiation, because light is absorbed, reflected and scattered in the 4 km of air between the contrail and the sensor. In that time the UAV has flown 180 m, which is small compared to the field of view of $2,174$ m. During the contrail radiation measurements it is not necessary to take static measurements, because the optical properties of the contrail compared to the background are required, not a static image.

8.7 Power Consumption

The power consumption of the ultra-compact spectrometers is 30 mW each, making the total 120 mW. Table 8.2 shows the power characteristics of the Quark configurations [70]. Only one digital channel will be used (parallel or serial) such that the values from 8.2 are valid. However, actual power dissipation will be lower because of the lower operating temperature. Assuming that the temperature dependence of the electrical resistivity is linearly related to temperature, the estimated power dissipation for an operating temperature of $-40°C$ is $1.10\ W - 65°C \cdot \frac{0.15\ W}{55°C} = 0.92\ W$.

Table 8.2: Quark Power Dissipation

Quark Configuration	Power at 25°C	Power at 80°C
336	$\leq$ 1.00 W	$\leq$ 1.15 W
640	$\leq$ 1.10 W	$\leq$ 1.25 W

Table 8.2 is given with the following note: "*The values above assume a single digital channel (BT.656, CMOS, or LVDS) is enabled and that the analog channel is disabled. The values are increased by approximately 65 mW by disabling all digital channels and instead enabling analog.*"

8.8 Contrail Search Flight Path

To find contrails within range of the ground station, a search flight path is determined. Two types of paths are considered: circular and linear. The circular flight path is selected, as it does not require a small turning radius and is more effective at searching the area for contrails in all directions. The minimum turning radius of StratoMAV is 69 m, which is sufficient to carry out the contrail search flight

path that requires a minimum turning radius of 10 km. The turning radius of 69 m is also adequate to turn around at the end of the contrail, as it is smaller than the width of a starting contrail (around 100 m) and much than the length of a contrail (several kilometers).

8.9 Contrail Detection and Radiation Measurement Scenario

The following is a typical contrail measurement scenario. A certain area is chosen for contrail measurements for a week, depending on the available power, before the UAV moves to another location. The ground station is placed in the center of the area, from which StratoMAV starts its contrail search flight path: a spiral outwards to the boundary of the ground station's range. The first contrail found will be closest to the ground station, which is advantageous for the downlink. Flight status updates are sent periodically. Every 0.12 s the thermal camera takes an image, but every minute a frame is processed by the contrail detection algorithm to determine contrail presence. If no contrail has been found, StratoMAV continues its path and takes another image. If the algorithm did detect a contrail, the image is downlinked with a notification. StratoMAV first determines from a second frame the direction the contrail is moving in and then flies along the border, making sure the spectrometers are aligned with it. At day, the spectrometers take measurements every 10 s; at night only the thermal camera works. StratoMAV tracks the contrail until the maximum communication range or the end of the contrail is reached. The UAV also stops tracking if the power is low, or the ground station sends a message to stop measuring. In all cases, StratoMAV turns around and follows the contrail in opposite direction. Contrail tracking can last several hours. StratoMAV stops measuring when the contrail is no longer detected by the algorithm. Then StratoMAV resumes its search flight path and turns off the spectrometers (if it was day). Now, the collected data is downlinked for processing.

8.10 Conclusion

In total five sensors take measurements on the radiative properties of contrails, to understand the regional climate effects. The sensors are four Hamamatsu spectrometers and one FLIR thermal camera, which have been chosen for their lightweight design and low power consumption. The thermal camera measures an area of 3.1 x 2.5 km and has a pixel size of 4.8 m at contrail height (4 km below StratoMAV), with a sensor size of 640 x 512 px. The spectrometers each measure an area of 2.2 x 0.2 km and has a pixel size of 212 m at contrail height, with a sensor size of 640 x 512 px. Their total weight is 58 g and the power consumption is 1.0 W. They will take regular, continuous measurements once a contrail has been found with the contrail detection algorithm. A payload processor has been chosen to carry out the required image processing, but serves as a backup processor in case the autopilot processor fails.

Chapter 9

Support Systems

The support systems are the subsystems on-board StratoMAV that do not perform the flight, or measurements. These support subsystems are the autopilot, telemetry, thermal control and the ascend and landing system. The design of each subsystem is described in more detail in this chapter.

9.1 Telemetry

StratoMAV's telemetry has three main functions. First there is the uplink from the ground station to the UAV. This can be for example a new mission location the UAV has to fly to, or a stop command when enough data has been collected. The second function is providing status updates of the UAV. Finally there is the payload data that has to be downlinked. The main focus of the section is on the design of the downlink, since this is important for the UAV communications subsystem design. The ground station telemetry design is less critical because it is not limited by weight constraints. First the components of the telemetry subsystem are looked at. Next the calculation of the data rate is presented and the link budget calculation is given. To obtain a low transmission power while maintaining sufficient range, a balanced combination of choices is made between the gain of the antenna (and its weight), the chosen modem and data rate, and other factors in the link budget calculation.

9.1.1 Antenna

One of the important components of the telemetry subsystem is the antenna. Its gain is a major factor in the link budget calculation and has an influence on the required transmit power. Its shape will affect the structure of the UAV and perhaps its aerodynamic properties.

Antenna Type Selection

First of all, an antenna type is selected from the most commonly used antenna types. Several examples are discussed below.

- **Wire antennas:** These are the simplest types of antennas. Wire dipole antennas are very commonly used. Among the circular wire antennas are loops which have been arranged in a certain pattern, such as the slot antenna, a random configuration or a grid. A long wire arranged in a certain shape could easily be integrated in the lower part of the wing and is inexpensive. However, if the antenna is fixed permanently in the wing structure, it might be hard to disassemble or repair

the antenna in case of damage. The gain and directivity of a dipole increase with the length of the dipole (in multiples of the wavelength). However, the wing dimensions will constrain the antenna design and thus the possible operating frequencies and corresponding gains. Additionally, folds in the loop reduce the gain of the dipole. The wire dipole antenna has an omnidirectional radiation pattern, which is not necessary for the UAV because the antenna should only transmit in the downwards direction of the UAV and not in the upwards direction (towards the wing). Loop antennas are often used as receiving antennas, because they are difficult to match to a transmitter (due to the antenna's impedance) [71].

- **Microstrip antennas:** Similar to wire antennas, microstrip antennas can easily be integrated at the lower side of the wing, without protruding elements that would disturb the flow (because of their flat profile). Patch antennas are low weight, inexpensive and suitable for the use in ranges from around 1 GHz to 6 GHz, so they are frequently used in aircraft and spacecraft applications. By placing multiple microstrip antenna elements in an array, the resulting gain can be increased. The polarization of the antenna can easily be adjusted in the design and microstrip technology can easily be printed and integrated with other circuit elements. "A single microstrip patch antenna has a typical directivity of 8-9 dBi. Multiple microstrip radiating elements can be coupled together to produce a higher gain which can approach 20 dBi gain." [29]
- **Reflector and Aperture antennas:** While these two types of antennas provide high gain, they are also bulky and would take up a lot of space and disturb the airflow around the UAV. They are therefore not a feasible options for the UAV.

Looking at the weight, gain, cost, integration into the wing and maintainability of the possible antenna options, the microstrip antenna is the most favourable option.

9.1.2 Antenna Design

The chosen antenna design is based on the antenna described in the paper by T. R. Harris [30]. It is a rectangular patch made of Isola FR404 substrate which is a glass reinforced composite with copper layers at the top and bottom side. Its dielectric constant is $\eta_r = 4.26$. The dimensions of the patch are 102.9 mm x 74.3 mm. The weight is calculated from the densities of copper (8.94 g/cm^3) and Isola FR404 (1.85 g/cm^3) and the heights of the copper and composite layers (35 μm and 0.20 mm). Hence, the total weight is 7.6 g for two antennas in an array.

9.1.3 Modem

Several frequencies were considered, especially the 2.4 GHz and the 5 GHz bands. However, no low weight, low power consumption modems or transceivers for these frequencies could be found that would fit StratoMAV's requirements. Often little information was available from the manufacturer or seller. Since information about every subsystem of StratoMAV is crucial for the rest of its design, it was decided to choose a modem for 900 MHz which did have a specification sheet and is lightweight. The choice of this modem affects the antenna design. The chosen module is available with a simple wire antenna or with an antenna connector. It is suggested to design a specific high gain microstrip antenna for StratoMAV. For now, the antenna gain is assumed to be 3 dB. The specifications of the chosen RF module (Radio Frequency module), the XBee-PRO©900HP, can be found at the Digi website [72]. The most important values are the frequency band, 902-928 MHz, the transmit power, up to 250 mW, the maximum data rate, 200 $Kbps$, and a minimum operating temperature of $-40°C$. The receiver has an outdoor range of up to 45 km with a high-gain antenna. A custom high-gain antenna can be

connected to the RP-SMA connector. The receiver sensitivity is $-101\ dBm$ at 200 $Kbps$. The modem can be connected to the processor using the UART or the SPI serial connection ports.

9.1.4 Data Rate and Compression

The FLIR Quark core uses a 14 bit grey-scale depth and each pixel is stored in two bytes of memory. The data rate calculation for the FLIR thermal camera core is then: $640\ px \cdot 512\ px \cdot 2\ bytes = 6.6 \cdot 10^5\ bytes/frame$. With an effective frame rate of the contrail detection sensor of 1 $frame/min$ (chapter 8), the amount of bytes per second is $1.1 \cdot 10^4\ bytes/s$. The same data rate calculation is performed for the total of four spectrometers (taking an integration time of $10,000\ ms$ and an AD conversion of 16 bit, assuming 2 $bytes/pixel$): $4 \cdot 256\ px \cdot 1\ px \cdot 2\ bytes = 2.0 \cdot 10^3\ bytes/frame$. With an effective frame rate of 0.1 f/s, the amount of bytes per second is $2.0 \cdot 10^3\ bytes/frame \cdot 0.1\ frame/s = 2.0 \cdot 10^2\ bytes/s$. Compared to the contrail detection data, the spectrometer data is neglible, so the total data rate is $1.1 \cdot 10^4\ bytes/s = 89\ Kbps$.

The over-air-data rate is calculated with equation 9.1 [73], where D_{pl} is the payload data in bits, D_{ao} is application overhead in bits per payload transmission, D_{ro} is radio overhead in bits per payload transmission, and rt is the retry percentage, which is assumed to be 10%).

$$RFdatarate = (D_{pl} + D_{ao} + D_{ro}) \cdot (1 + rt)/time \tag{9.1}$$

Using ten data packages per second to transmit the generated payload data of one second, the total data in one package is calculated by adding a tenth of the payload data to the application overhead and the radio overhead. The application overhead is calculated to be 32 $bits$, by using a start byte, an address byte, a data-length byte and a checksum byte per package. The radio overhead is the amount of redundant bits used in Forward Error Correction to reduce the Bit Error Probability (BEP). Using a radio overhead of 12.5% of the payload data the decoding gain is 3.6 dB compared to not using decoding and the required Signal to Noise ratio for a BEP of 10^{-6} is 6.9 dB [31]. The required data rate to send one package is then: $(8.9 \cdot 10^3 + 32 + 1.1 \cdot 10^3) \cdot (1 + 0.1)/(1/10) = 110\ Kbps$. Since this equals half the transmitter data rate of 200 $Kbps$, the measured data can easily be transmitted to the ground station in real time. However, it might be too power demanding to take contrail measurements and transmit data at the same time. If excess power is available this could be done, but when flying at more critical latitudes the data could be stored during measurements and transmitted later. No compression is performed on the data before downlinking, because the data rate is already low and can be transmitted. Using the other transmission rate of 10 $Kbps$ supported by the modem, would save $230mW$ transmit power which is about equal to the required processing power(compare to autopilot and payload processor power consumption: $0.2W$ and $0.5W$) for a $11:1$ compression rate. Comparing the processing power to the transmission power, the increased complexity, processing time and inevitable data loss, it is not considered useful to use data compression.

9.1.5 Downlink Budget Calculation

The link budget is calculated using equation 9.2(eq. 13-13, SMAD[32]). The values used are shown in table 9.1. The main equation used is [32]:

$$\frac{E_b}{N_0} = P + L_{lt} + L_{lr} + L_{pt} + L_{pr} + L_a + G_t + L_s + G_r + 228.6 - 10log(T_S) - 10log(R) \tag{9.2}$$

BW was taken from the modem specifications [72]. Variables e, L_{pr}, L_{lt}, L_{lr} and L_a and G_t have been estimated based on values from an ITU 2011 report on UAV telemetry [33] and SMAD [32].

Table 9.1: Downlink budget example

Variable	Symbol	Used Value
Frequency $[MHz]$	f	900
Bandwidth $[MHz]$	BW	26
Range $[km]$	d	50
Data rate$[Kbps]$	R	200
Transmitter power $[mW]$	P	240
Transmitter antenna gain $[dBi]$	G_t	3
Transmitter cable loss $[dB]$	L_{lt}	-2
Free-space loss $[dB]$	L_s	-125.5
Ground antenna diameter $[m]$	D_{gr}	2.5
Receiver cable loss $[dB]$	L_{lr}	-1
Relative pointing error transmit [-]	e	0.25
Transmitter pointing loss $[dB]$	L_{pt}	-0.75
Receiver pointing loss $[dB]$	L_{pr}	-2.6
Attenuation loss $[dB]$	L_a	-23
Receiver antenna gain $[dBi]$	G_r	25.2
System noise temperature $[K]$	T_s	135
Signal to Noise Ratio [dB]	**SNR**	**21.4**

c is the speed of light with a value of $2.998 \cdot 10^8$ m/s and eff is taken from p.553 of SMAD[32].

$$L_s = 10log\left(\left(\frac{\frac{c}{f}}{4 \cdot pi \cdot d}\right)^2\right) \quad (9.3) \qquad L_{pt} = -12 \cdot e^2 \quad (9.4) \qquad G_r = 10log\left(\frac{\pi^2 \cdot D_{gr}^2 \cdot eff}{(c/f)^2}\right) \quad (9.5)$$

The total attenuation loss at $15km$ altitude has been extrapolated from data in the ITU report [33] to be $23dB$. With equation 9.2 the SNR is calculated to be 21.4 dB. This value is higher than the required value of 6.9 dB for a BEP of 10^{-6}, so 50 km is a range over which data can be transmitted with a sufficient SNR. The link margin equals $21.4 - 6.9 = 14.5dB$, which corresponds to a link reliability of 96% [34]. The downlink budget will result in similar values, if not better because a higher transmitter power can be used.

9.2 Autopilot

Since StratoMAV is an unmanned vehicle, it needs an autopilot. The autopilot support system consists of several hardware components and a software program to regulate the controls. The software sets the aircraft throttle, angle of attack, climb rate and its navigation route. These values are based on measurement data provided by the hardware. The hardware includes sensors for airspeed, attitude, position and power regulation between the components. A small processor is also needed to perform the required calculations.

The cost is a determining factor for the autopilot. It is possible to buy off the shelf autopilot systems such as the Micropilot system. These are all-in-one systems which can have a total mass as low as 28 g. However, these systems cost around $2,500. It is also possible to use Paparazzi systems, which have a cost of about $300-400 for the total system, while having the same mass. Additionally, the Paparazzi software is open-source, making it easier to change the coding for stable flights.

Therefore, a Paparazzi system has been chosen and the autopilot is designed using the JSBSim open

source software. This program is used for many existing MAVs. The autopilot uses PID controllers to control the aircraft. The way these controllers react can be adjusted by varying the gains in the program.

9.2.1 Autopilot Hardware System Choice

The hardware set up was selected from the available options on the Paparazzi website [74]. For the autopilot system the UMarim lite V2 board is chosen. This board is based on the LPC2148 micro controller, and its development was finished in the summer of 2012. The board contains the latest technology and uses the smallest gyroscope that is currently available. The Internal Measurement Unit (IMU) is built-in, which eases the choice considerably. The mass including the IMU is only 8 g, making this combination the lightest of all. The chip operates from $-40°C$, however the resistors produce enough heat to keep the chip at the required temperature. The chip has a required current of 100 mA with a working supply voltage of 3.3 V [35]. Therefore the required power is 330 mW. The board also has a built-in power regulation. This provides the correct voltage and power for the airspeed sensor, GPS sensor and the servos. The total cost of this package is $399 [75].

9.2.2 Sensors

In order to control the aircraft, input regarding the current state of the aircraft is needed. Parameters such as airspeed, pitch, bank and roll angle determine the error between the desired and current state. These parameters are provided by the sensors. Typically, an autopilot uses two types of sensors: one for orientation and one for altitude. Moreover, an airspeed sensor is required.

Orientation Sensors

To determine the orientation of StratoMAV, two types of sensors can be used: an IMU or infrared sensors. Both measure the attitude angles of the aircraft. The IMU measures accelerations and rotation rates using small gyroscopes and accelerometers; sometimes magnetometers are added to improve the accuracy of the measurements. Infrared sensors measure the temperature of the incoming heat flux. In the Umarim Lite V2, an IMU is built in that is accurate enough without IR sensors. Since StratoMAV is designed to make a belly landing, an IMU is preferable as it can be placed inside the aircraft. This is in contrast to the IR sensor, which has to have a line of sight towards the ground.

The built-in IMU has 3-axis electronic gyroscopes and accelerometers to accurately determine the attitude of StratoMAV. The accelerometer has a resolution up to 11 bits ranging from -4 g to 4 g. As StratoMAV can withstand loads up to 2 g, the maximum load factor is within the range and very extreme loads can be measured with sufficient accuracy; better than $1/100$ g. The sensors operate at a current of 23 μA with an operating voltage of 2.5 V. Three of them are used, one on each axis, which gives a total required power of $23 \cdot 10^{-3} \cdot 2.5 \cdot 3 = 0.15$ mW [36].

The operating temperature range of the accelerometers starts at $-55 \circ C$ and the for the gyroscopes at $-40°C$; they must therefore be kept warm to work properly. The accelerometers work at $6.5mA \cdot 3$ $V =$ 19.5 mW with an accuracy of $0.07 degree/sec/bit$. As they are built-in, their price is included in the chip price [37].

Altitude Sensor

To determine the altitude, a pressure sensor or a simple GPS sensor can be used. The pressure sensor compares the ambient pressure to the standard atmosphere to measure the altitude. GPS uses satellites to determine position and the derivative of the position is used to determine the airspeed. Since GPS is also required for accurate navigation, this system is selected for altitude determination. An airspeed sensor is used as redundant sensor as well, which will be discussed in detail in the next section. The static pressure of this sensor can also be used for altitude determination in case the GPS signal is lost. For the GPS sensor the UC530M from Ublox was chosen, which is a GPS chip with integrated antenna with a low mass and low power consumption. This sensor weighs 0.5 gr and has a power consumption of 66 mW operating at 3.3 V. The accuracy of the GPS sensor is 3 m circular error position (CEP) and works up to 10 Hz. The dimensions are $9.5 \cdot 14 \cdot 2$ mm so it fits in the wing. It has an operating temperature range of $-40°C - 85°C$, so this part needs heating or insulation to work properly [37].

Airspeed Sensor

The airspeed sensor uses a pitot tube to measure static and total pressure. Based on the difference between the two (the dynamic pressure), the ground speed is calculated. This can be used to get more accurate values for the speed. The airspeed sensor selected costs $43 including the pitot tube and has a total mass of 7 g. The accuracy of the sensor is 0.5 m/s. The pitot tube has to be placed in the direction of flight and at the leading edge of the wing. It can be placed at a certain distance so that it can measure at a location where the air is not influenced by the propeller. The package also contains a plastic tube of 3 m to overcome the distance from the air inlet to the air pressure sensor, while remaining the correct pressure [76]. The pitot tube needs heating or insulation to prevent ice build up.

Now all hardware components have been chosen, a summary is given in table 9.2 with the mass, power consumption and associated cost per item.

Table 9.2: Summary of the hardware components of the autopilot

Component	Masses (g)	Dimensions (mm)	Power (mW)	Cost ($)
Umarim lite V2	8	53 x 24 x 4	200	399
airspeed microsensor V3	4	28 x 16 x 10	10	43
pitot tube	3	80 x 4(D)	-	-
GPS sensor	0.5	9.6 x 14 x 2	66	35
Total	**15.5**	-	**276**	**477**

9.2.3 Servos

To design the servos, the maximum torque they experience due to control surface deflection has to be known. This torque can be calculated with an Excel sheet [77]. The following parameters have to be used: average control surface chord, average control surface length, maximum servo arm deflection angle, maximum airspeed and maximum control surface deflection angle.

First, the aileron servos are designed. The average aileron chord can be calculated by averaging the inner and outer chord: $(30.3 + 25.2)/2 = 27.75$ cm. The average aileron length was found to be 77 cm. The maximum servo arm deflection was found by looking at several micro servos, and is determined to be 60°. Now the maximum airspeed has to be converted to ground airspeed, as the spreadsheet uses

sea level values for density and pressure. The airspeed also has to be converted to mph. The ground airspeed in mph is found to be $((V_{max} \cdot 2.4)^2 \cdot (\rho/\rho_{ground})^{0.5} = 22\ mph$.

The output of the Excel program is the maximum torque the servo needs, to operate the ailerons. To have a reasonable servo mass (about 5 g per servo) the maximum torque may not exceed 16 $oz-in$, or 11 Ncm. For larger torques, the servo mass increases quickly. With a maximum aileron deflection of 20°, servos of 5 g can be used. The servo selected is the Dymond D47 and is capable of achieving a torque of 11 Ncm, which is sufficient for the ailerons. It has a higher maximum torque than other servos with the same mass and has a low power consumption. Each servo costs €19.90, has a mass of 4.7 g and requires 6 $V \cdot 80\ mA = 480\ mW$ at maximum deflection.

The same counts for the ruddervators, only here the speed is higher as air is accelerated by the propeller. This speed increment is determined using equation 9.6. A is the disk area of the propeller and T the thrust delivered. The change in airspeed ΔV can be found to be 1.5 m/s, so the airspeed at the tail is 26.5 m/s. Converting this to the ground speed in mph and keeping the maximum deflection of the ruddervator at 20°, a maximum torque of 13.6 $oz-in$ or 11 Ncm is found, which means that the same servo can be used. The size of the servos is 28 x 17 x 8 mm, so they will easily fit in the wing and the tail. The main problem with the servos is their operating temperature range: $-30°C$ - $40°C$. They need thermal control to keep them working in the cold environment. The mass of the servos for a total of four servos is $4.7 \cdot 4$=18.8 g excluding the cabling. The length and mass of the servo cables will be determined in the next section [78].

$$T = \rho \cdot A \cdot V_0 \cdot (\Delta V) \tag{9.6}$$

9.2.4 Servo Cables

The autopilot is assumed to be at or very close to the center of gravity. In the autopilot, the signals for the servos are generated. This signal has to go towards the servos through cables. For the ruddervators, the cables first go to the left or right boom over a distance of 77 cm, after which they go through the boom towards the tail located 150 cm backwards. The servo is installed near the control surface. From the centre of gravity towards the middle of the ruddervator, a cable of 250 cm is needed, both for the right and left ruddervator. The cables for the ailerons only go in X-direction. Again, the servo is located at the most inward location of the control surface. The aileron is located at 2.25 to 3.10 m from the root. A cable of 2.25 m is used for both the right and the left aileron. The total cable length now comes 9.5 m. The cabling used is Turnigy Teflon Coated Wire 36AWG, with a mass of 0.24 g/m for the wire only. Three wires per servo are needed: one for the signal, one positive and one negative wire. Assuming the coating also has a mass of 0.24 g/m, the total cable mass for the servos becomes $0.24 \cdot 2 \cdot 3 \cdot 9.5 = 14\ g$. The price of the cable is only \$0.59/m resulting in a total of \$6.5 for the cables. This cable has a voltage loss of only 0.05 $V/m/A$. As the maximum distance is 2.8 m and the maximum current is 80 mA, the loss is maximum only 0.01 V, which is acceptable [79].

9.2.5 Integration

The autopilot system and its components are located in the middle of the aircraft, close to the center of gravity. The components are glued to the rib. From the battery, a power cable runs to the autopilot system and the servos. The aileron servos will be connected to the rib at 2.25 m from the wing root. Screws are used to attach the servos to the rib. The cables run back, glued to the rib, towards the spar and are glued to the spar running back to the center of gravity to the autopilot system. The

ruddervator ailerons are located at half the V-tail and are connected to a rib using screws. The cables are glued to the spar in the V-tail. At the end of the booms, they follow the rib and the spar towards the autopilot. In total 15 g is reserved for the glue, the screws and other integration parts to connect the autopilot and the servos in StratoMAV.

9.2.6 JSBsim

An autopilot for StratoMAV is written using JSBSim. JSBSim is an open source flight dynamics model which uses forces and moment to calculate the movement and rotations of the aircraft. The aircraft parameters are implemented in a xml-file, which is divided in several sections. In the metrics section, the aircraft dimensions and mass are implemented, as well as the center of gravity location and the mass moments of inertia. In the next section the propulsion is defined. A file for our engine was made and implemented. Next the pitch, roll and yaw channels are defined. For simplification and because the control derivatives are calculated for this configuration, the model assumes a normal tail with a separate rudder and elevators. The maximum control surface deflections are implemented and the control surface for each moment is chosen. For pitching and rolling stability, respectively the elevators and ailerons are used. To steer StratoMAV to the correct PSI, it was chosen to use the rudder. This is because the aileron effectiveness was found to be quite small, and making a turn would take very long with a turn radius over 500 m.

After setting up the correct channels, the aerodynamics part was implemented. As JSBSim has 6 degrees of freedom, the aerodynamics part has 6 sections: lift, drag, side slip, pitch, roll and yaw. In the lift section the lift coefficient and the stability derivatives with respect to the Z-axis are implemented. It is assumed that$L = -Z$. For the side section, the stability derivatives with respect to the forces in Y-direction are defined. For the pitch, roll and yawing sections the stability derivatives and the control derivatives are implemented.

PID Controller Calculations

The JSBSim autopilot uses PID controllers to control the aircraft. These PID controllers are control feedback loop mechanisms, and are used in various applications. Initially, there is a difference between the desired value and the measured value. The desired value may be input received from the ground station or a result from a previous calculation. The controller multiplies the error and possible the integral and derivative by a gain and sends the value to a controller. The PID controller uses at most three control parameters: the proportional, the integral and the derivative. The proportional controller stands for the current error. The integral is the accumulation of the past errors and the derivative is for the prediction of future errors. The weighted sum of these controls the input for the controller. For example, an aileron deflection can be controlled by this system to get a required bank angle. An example of the PID heading control system is shown in figure 9.1.

Figure 9.1 shows that for the heading controller, the error is multiplied by a proportional, integral and derivative gain. The sum of these outcomes is interpreted as the desired rudder deflection. A limit is implemented as too high yawing rates result in high rolling rates. Finally, this signal goes to the yawing channel with a rudder deflection as a result.

JSBSim output

The state of the aircraft is can be calculated by JSBSim. It was found that without an autopilot the aircraft would eventually enter a spiral with increasing yaw angle and roll angle. JSBSim confirmed this

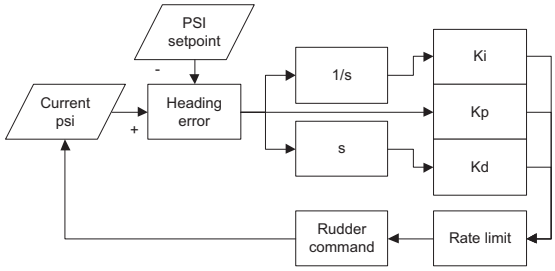

Figure 9.1: PID heading control in JSBSim

by simulating cruise flight at 15 km altitude. An autopilot can prevent this by activating the control surfaces in the correct way. For each of the 3 moments, the gains were tuned such that a smooth but quick response to inputs was established. Several limits to the control surfaces arose; roll and yaw rates can only be small, or the rolling moment will increase with an uncontrollable aircraft in response.

The differences between the simulation with and without autopilot are shown in figure 9.2 to figure 9.5. For the heading angle a desired angle of 330 degrees was chosen to show the rudder effectiveness. Also the roll angle for the autopilot shows a slight bump. This is due to the yawing motion to get to the desired PSI. With the rudder as steering device the heading angle can be adjusted way quicker than with the ailerons as steering device.

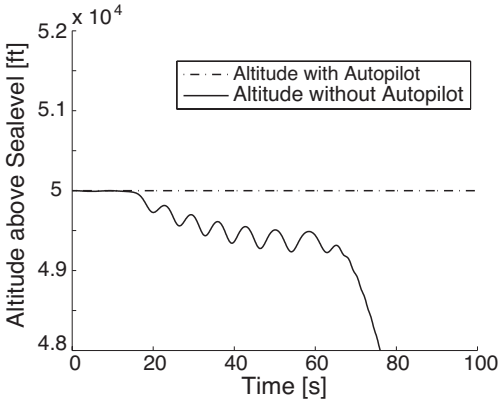

Figure 9.2: Altitude in cruise flight with and without autopilot

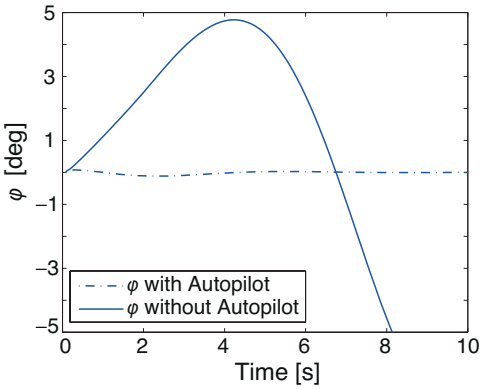

Figure 9.3: Roll angle in cruise flight with and without autopilot

As can be seen in figure 9.2, the autopilot keeps StratoMAV on the correct altitude even when it is asked to make a turn. The desired heading is in all cases 330 degrees. Without the autopilot, StratoMAV start a spin with an increasing roll rate and yaw rate. This results in an unstable condition.Figure 9.3 shows that the roll angle is unstable if the autopilot is turned off. With the autopilot turned on, the ailerons damp the motion completely so StratoMAV flies at a roll angle of 0 degrees.

In order to steer StratoMAV to the correct heading, the rudder is activated. At the same time the ailerons keep the roll angle low. As can be seen in figure 9.4 the heading angle is adjusted smoothly to the desired heading of 330 degrees. Without the autopilot StratoMAV, the heading is continuously changing. Finally in figure 9.5 the pitching angle is shown. Preferably the pitch angle is constant as is the case when the autopilot is turned on. Without the autopilot applying the correct elevator deflection, the pitch angle diverts quickly.

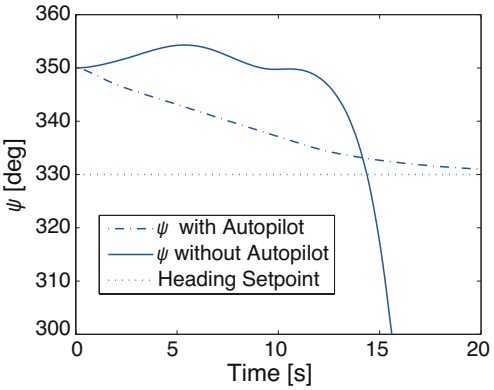

Figure 9.4: Heading angle flight with and without autopilot

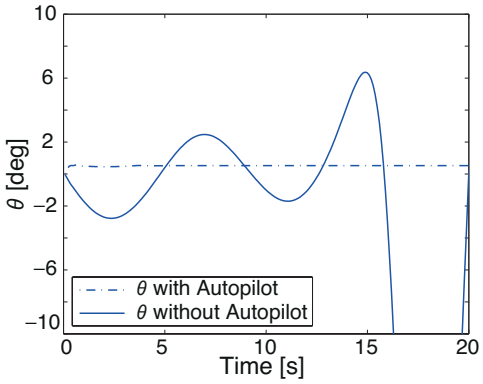

Figure 9.5: Pitch angle in cruise flight with and without autopilot

Scenery

In JSBSim different scenarios for testing StratoMAV can be executed. In the scenarios, the autopilot functions can be turned on or off. Commands can be given to adjust the power settings. The initial state of StratoMAV can be adjusted in the reset-file. Here, initial angles and velocities can be inserted.

9.2.7 Navigation Mode

To perform its science mission properly, StratoMAV must be able to navigate to the position where it will perform measurements. Therefore, a navigation mode is required for the autopilot. Starting in a user specified area, where the ground station is located, StratoMAV will have to look for contrails in the surroundings. From section9.1 it can be found the maximum distance to the ground station is set at 50 km. StratoMAV is therefore able to inspect $7.9 \cdot 10^3$ km^2 without losing the connection with the ground station. The UAV will fly in a outward spiral, starting at the ground station; it will fly in radii of $10, 30$ and 50 km. Hereafter, the aircraft fly back in a spiral. Most of the area is covered and the complete cycle is completed in 24 h. Therefore, the pattern can be repeated every day to check the results. The pattern is visualised in figure 9.6 but with smaller radii. The real flight plan has the correct radii implemented.

When a contrail is detected, the flightpath will be changed to follow the contrail. StratoMAV follows the contrail until it has reached the end of the contrails or the 50 km range is reached. In both cases, the aircraft turns around and follows the contrail back until it is vanished. Then the contrail search pattern is picked up again until the next contrail is detected. This pattern has been implemented in the Paparazzi flight plan.

Also some safety procedures are built in to ensure StratoMAV stays operational in case of system failure. When the UAV cannot connect to the ground station, it will automatically return and keep loitering above it until the telemetry link is back up again. It is decided that StratoMAV enters this mode after the radio connection is lost for more than 60 seconds. If the link is down for more than $12h$, the aircraft will automatically land at the home location where its telemetry system can be inspected.

When the GPS signal is lost for more than 5 minutes, the UAV also enters the safety mode and will return to the ground station. StratoMAV will circle around the ground station with a radius of 1 km. IMU data is used to determine the route in this case, but it must be kept in mind that the route may not be very accurate, as IMU data accumulates measurement errors. In normal conditions, the drift

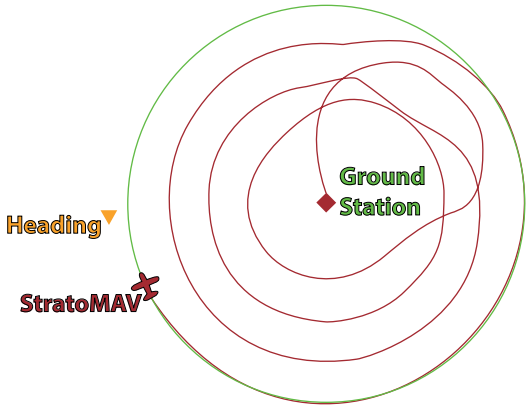

Figure 9.6: Flight pattern made in Paparazzi

can be adjusted by using GPS to correct the position and a pitot tube to correct the airspeed. If the GPS signal is lost for more than 12 h, StratoMAV will automatically descend and land at the ground station. These modes are implemented in the flight plan file in Paparazzi, where several navigation points can be defined such as the ground station position.

9.3 Thermal Control

To determine if thermal control is necessary, a first-order approximation of the temperature of the complete UAV system is made. This estimation is made for two worst case situations, further referred to as the cold case and the hot case. The cold case corresponds to the situation during the night when there is no irradiation from the sun. The hot case corresponds to a summer day when there is solar irradiation and the solar panels generate heat. Performing a thermal analysis for the system involves knowledge of the thermal properties of all components of the UAV. This analysis is beyond the scope of this design. Therefore, an analysis will be carried out involving easy to analyse components. The UAV is first approximated by a rectangular wing, a rectangular tail and two booms, which is shown in figure 9.7. It can be concluded that the area of the booms is negligible when compared to the tail and wing area. Therefore, the UAV is approximated as a single rectangular box which combines the tail and wing area, as can be seen in figure 9.8. The area of this box is equal to the actual UAV area and has an infinitesimal thickness.

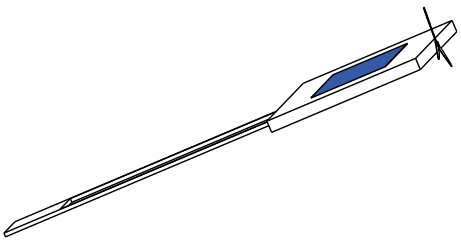

Figure 9.7: Approximation of the UAV for thermal control analysis.

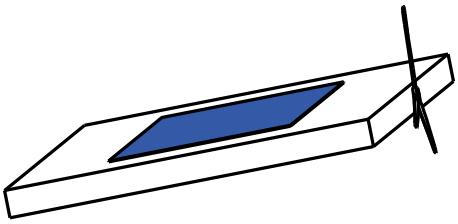

Figure 9.8: Approximation of the UAV

The temperature of the system is determined by the law of conservation of energy across the boundary/surface of the system. To do this, certain assumptions are made. It is assumed that the sides of the rectangular box are not involved in the exchange or absorption of heat from the internal or external environment, because of their negligible contribution to the total area of the box. Furthermore, it is assumed that the UAV is isothermal. This assumption excludes the possibility of temperature gradients within the system. Such temperature gradients increase the complexity of the problem and are therefore not included in this analysis. Heat can be transferred through three mechanisms: conduction, convection and radiation. For this case, it is assumed that there is no conduction since there are no solid bodies, present in the external environment, that come into contact with StratoMAV that could exchange heat. Finally, it is assumed that the motor and solar panels are the only components that internally generate heat. Furthermore, it is assumed that the waste energy of these components is converted completely into heat.

With these assumptions and the approximation of StratoMAV as a rectangular box, equation 9.7 shows the conservation of energy for this system.

$$Q_{absorbed} + Q_{dissipated} = Q_{emitted} + Q_{convected} \qquad [W] \tag{9.7}$$

For the cold and hot case, the terms in equation 9.7 are different. Therefore, in the following equations, the subscripts cold and hot will be used to distuinguish for these worst case situations. A_{total} represents the total area which is calculated as $A_{total} = 2 \cdot \ A_{wing} + 2 \cdot \ A_{tail}$ since the total area that is absorbing or emitting heat must be considered.

$$Q_{absorbed,cold} = (273 - 21)\alpha_{box}\frac{A_{total}}{2}cos(\alpha - \gamma) \tag{9.8}$$

$$Q_{absorbed,hot} = Q_{absorbed,cold} + G_{solar}A_{solar}cos(\alpha - \gamma)\alpha_{box} \tag{9.9}$$

$$Q_{dissipated,cold} = (1 - \eta_{motor})P_{motor} \tag{9.10}$$

$$Q_{dissipated,hot} = (1 - \eta_{motor})P_{motor} + (1 - \eta_{solar\ panels})G_{solar}A_{solar} \tag{9.11}$$

$$Q_{emitted} = \sigma \cdot \epsilon_{box}\left({T_{box}}^4 - {T_{surr}}^4\right) \tag{9.12}$$

$$Q_{convected} = h \cdot A_{total} \cdot (T_{box} - T_{surr}) \tag{9.13}$$

The IR radiation emitted by the Earth is $273 \pm 21\ W$ [38] and appears in the above equations as radiation absorbed by StratoMAV. Furthermore, G_{solar} is the irradiation coming from the Sun per square meter. To correct for the orientation of the aircraft, the angle of attack (α) and flight path angle (γ) are included in the above equations. With these angles the projected system area onto the local horizontal plane is calculated. The coefficient h represents the heat transfer coefficient. This coefficient determines how much heat is convected from the system to the environment or vice versa. It depends on the fluid type flowing along the convection surface, the material of the convection surface itself and on the fluid velocity. This coefficient has been set to 15 $W \cdot m^{-2}K^{-1}$ for a 18 m/s flow velocity, or cruise speed. Finally, the system will not absorb all incoming radiation nor emit all possible radiation. This is corrected for by the coefficients α_{box} and ε_{box}. The actual value of these coefficients is complicated to predict. They will be approximated according to equations 9.14 and 9.15, where it is assumed that StratoMAV consists, for a part, out of silicon(solar panels) and for the other part out of CFRP and Oracover [53], as discussed in chapter 5.

$$\alpha_{box} = \frac{A_{solar}}{A_{total}} \cdot \alpha_{silicon} + \left(1 - \frac{A_{solar}}{A_{total}}\right) \cdot (0.25 \cdot \alpha_{CFRP} + 0.75 \cdot \alpha_{ORA}) \tag{9.14}$$

$$\epsilon_{box} = \frac{A_{solar}}{A_{total}} \cdot \epsilon_{silicon} + \left(1 - \frac{A_{solar}}{A_{total}}\right) \cdot (0.25 \cdot \epsilon_{CFRP} + 0.75 \cdot \epsilon_{ORA}) \tag{9.15}$$

Now all parameters, except for T_{box}, in equations 9.8 to 9.13 are known. Equation 9.7 can be filled in and solved for T_{box} for both the cold case and the hot case. This will give the temperature of the system in the cold case and hot case situations, being -60.16 and -1.62 degrees respectively.

The thermal control system should be able to keep all components at their operating temperature. The desired operating temperatures of all components are given in table 9.3 and 9.4.

Table 9.3: All components with corresponding operating temperatures.

Component	**Operating Temperature [°C]**
Modem	-40 − 85
MPPT	-40 − 80
Contrail detection sensor	-40 − 80
Converter (to 5V)	-40 − 75
Converter (to 3.3V)	-40 − 70
IMU	-40 − 60

Table 9.4: All components with corresponding operating temperatures.

Component	**Operating Temperature [°C]**
GPS	-40 − 60
PCB	-40 − 60
Servos	-30 − 50
Data storage devices	-25 − 85
Battery	-10 − 60
Spectrometer	5 − 40

From table 9.3 and 9.4, it can be concluded that the cold case temperature is crucial for the design of the thermal control system. The thermal control system should be designed such that it is able to deliver at least enough power to keep the temperature at 5 °C for the spectrometer. Even though the required increase of temperature is large for the spectrometer, it is a relatively small component and therefore does not require much energy to heat up. The batteries require a ΔT of 50 °C and have a relative large area ($0.26m^2$). The batteries will therefore form a critical component for the design of the thermal control system. A large part of the components have a minimum operating temperature between -50 and -40 °C and thus require the same increase in temperature. It is convenient to group such components together and will be placed in zone_1. The same will be done for components with a minimum operating temperature between -30 and 5 °C and will be placed in zone_2. The battery will be identified as a separate zone (zone_3). In this way, three temperature zones are created within the UAV. Since the system has been assumed to be isothermal, the increase in temperature for each zone is known. The required temperature increase for zone_1, zone_2 and zone_3 are 20, 65 and 60 °C respectively. The temperature increase of 60 °C for zone_3 includes an increase of 10 °C since the optimal efficiency of the battery is at 0 °C.

At this point, a trade-off has to be made between using passive or active thermal control elements. Passive thermal control elements do not require power to operate, which is advantageous for StratoMAV. However, they do add weight to the system which in turn will also increase the power required to keep the system aloft. Active thermal control elements also increase the system mass, but could be lighter than passive thermal control elements. Furthermore, active thermal control elements require power to operate. A calculation will be performed here, to see how much power the thermal control system requires if it is build out of active elements. If the calculated power appears to be large, passive elements will be chosen to decrease the required power.

First the power required to heat up the batteries will be calculated. To do this, the law of conservation of energy is applied again; this time treating the system as the environment and the battery as the interior. The heat going out of the battery by conduction and emission must be counteracted by heat added to the battery from the heating element. This implies that $Q_{in} = Q_{out}$, which can be written as shown in equations 9.16,9.17 and 9.18.

$$Q_{in} = P_{heater} \cdot \alpha_{heater} \qquad (9.16) \qquad Q_{out} = \frac{\Delta T \cdot k_{bat} \cdot A}{\alpha_{bat} \cdot \Delta x} + \frac{\sigma \cdot \epsilon_{bat} \cdot \Delta T}{\alpha_{bat}} \qquad (9.17)$$

$$P_{heater} = \frac{\Delta T \cdot k_{bat} \cdot A}{\alpha_{bat} \cdot \Delta x} + \frac{\sigma \cdot \epsilon_{bat} \cdot \Delta T^4}{\alpha_{bat}} \qquad (9.18)$$

In these equations α, ϵ and k are thermal properties of the battery, whereas Δx is the thickness of the battery foil. With equation 9.18, the power that the heating element has to provide is estimated at 863 W. It is decided to use passive thermal control elements to decrease the heat going out of the battery. From the calculations, it appears that conduction plays a more dominant role than emission in the outgoing heat. Both conduction and emission can be decreased by using insolation systems, such as multiple layer insolations (MLI). A common type of MLI used in space and aeronautical applications, is a configuration in which there are multiple layers of kapton in combination with a polyester spacer [80]. In this design, two simpler types of MLI will be considered, namely multiple layers of kapton with air as a spacer on one hand. On the other hand, layers of aerogel with air as a spacer will be considered.

By using a passive thermal control element, the thermal conductivity k and emissivity ϵ in equations 9.16 and 9.17 are decreased. As a result, less heat is going out of the battery. The effective thermal conductivity and effective emissivity can be calculated using equations 9.19 and 9.20, where N represents the number of layers of the MLI.

$$k_{eff} = \frac{1}{\frac{1}{k_{bat}} + \frac{N}{k_{air}} + \frac{N}{k_{kapt}}} \qquad (9.19) \qquad \epsilon_{eff} = \frac{1}{\frac{1}{\epsilon_{bat}} + \frac{N}{\epsilon_{air}} + \frac{N}{\epsilon_{kapt}} - 1} \qquad (9.20)$$

Substituting the effective values of equations 9.19 and 9.20 into equation 9.18, the new power required to heat up the batteries can be calculated. This required power depends on the number of layers, as can be seen in figures 9.9 and 9.10.

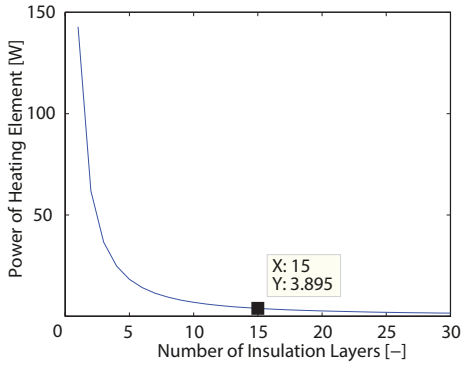

Figure 9.9: Power vs number of insulation layers graph for aerogel

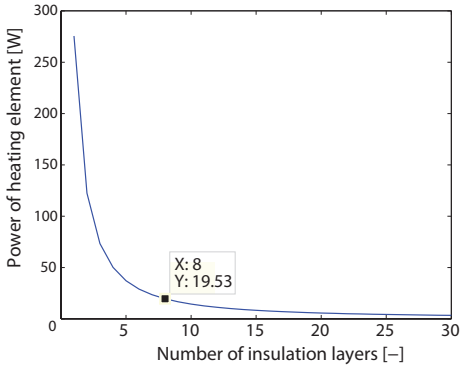

Figure 9.10: Power vs number of insulation layers graph for kapton

For an increasing number of insulation layers, the power required to heat up the batteries decreases, as expected. Furthermore, it can be seen that for 10 or more insulation layers, the required power

Table 9.5: Properties for two configurations of the thermal control system. The green highlighted configuration is selected as the final thermal control system.

	Weight [kg]	Power [W]
Active+Passive	0.20	3.9
Active	-	863

does not decrease significantly. The weight that is associated with the numbers of insulation layers, is shown in figures 9.11 and 9.12. For each point in these figures, the weight shown includes the weight of the insulation system and the weight of the active heating element that is required for the number of layers associated with the point in the figure. An approximation of the mass of the active heating element has been made and is equal to $0.01kg$ per installed W of active heating element. Figure 9.11 shows a minimum weight of 0.20 kg at 15 layers of aerogel, whereas in figure 9.12 a minimum weight of 0.49 kg occurs at 8 layers of kapton. The insulation system with 15 layers of aerogel has a lower weight and is therefore chosen. The thickness of the layers ($0.001m$) and the spacing between the different layers ($0.002m$) were not varied. The power required could be decreased further by varying these two parameters.

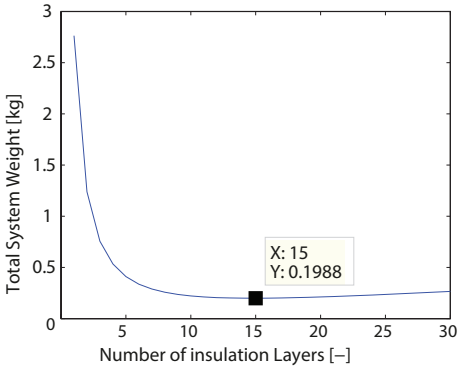

Figure 9.11: System mass vs number of insulation layers for aerogel

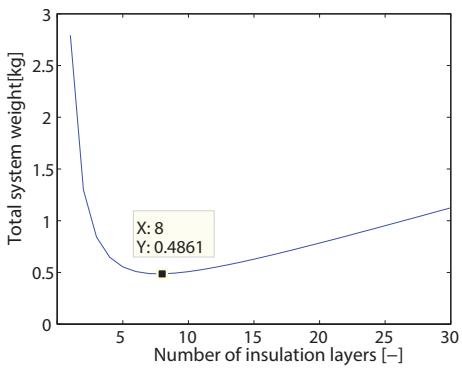

Figure 9.12: System mass vs number of insulation layers for kapton

From this analysis it can be concluded that the thermal control system for the batteries consists of an insulation system with 15 layers of aerogel with air as a spacer. Aerogel is an expensive insulator, but weight is regarded more important in the design of the thermal control system. The thermal control system weighs 0.20 kg and the active heating element requires 3.9 W. This is regarded achievable, since the power system has been designed with a safety factor of 5 %. It must be noticed that this power is only required in the worst case. For most of the time, the ΔT will be less and no power for active heating has to be used. For the components in zone_1 and zone_2, only an insulation system will be used. In table 9.5 it is shown how much power the thermal control system consumes and how much it weighs for two configurations. The green highlighted configuration is selected.

9.4 Launch System

StratoMAV does not have to ascend on its own power. However if StratoMAV is launched from the ground, it will need to be carried by several persons, like the Zephyr. StratoMAV would also spend

more than two hours in commercial airspace while ascending. During ascent, collision avoidance is difficult, since all the power goes to the ascent. Also, an extra system would have to be taken on board, to avoid other aircraft when crossing commercial airspace. Due to the aforementioned reasons it is concluded that ascending on own power is too difficult; therefore, an external launch system will be used.

Two options are considered for launching StratoMAV: the use of a balloon or an aircraft. The trade off is explained below.

- The expected load factor is the most important factor. This is due to the fact that the UAV has to ascend to $15,000\ m$ without breaking down, since after the launch repair is not possible. The expected load factor is assumed to be higher if StratoMAV is launched from an aircraft. Aircraft at altitudes above commercial airspace, have a higher velocity than the cruise speed of StratoMAV. Therefore it is assumed that the load factor during the launch will be higher than from a balloon, which has a velocity of zero with respect to the wind speeds.
- The launch speed is also of high importance. If the launch speed is too high, StratoMAV might experience high loads during launch. When the launch speed is too low, it might be uncontrollable. Aircraft that can carry StratoMAV usually fly faster than the cruise speed of StratoMAV.
- Launch costs have a relatively low weight factor, since they are not driven by requirements. However, they are important to take into account. The launch cost of a balloon will be around 400$ [81][82]. To launch by aircraft will be more expensive, since fuel, a pilot, take-off and landing rights have to be paid.
- Collision probability has a low weighing factor. This is due to the fact that the launch moment can be chosen, such that the chance of collision during ascent, like aircraft in commercial airspace. Launch with an aircraft has a high score, due to the fact that collision can actively be prevented.
- Gust resistance has a medium weight. The same holds as for the collision probability, the launch date can be selected such that the chance of a gust is minimized. However, the chance of a gust is higher than the chance of a collision.
- Technical complexity is given a high weighting factor. When an aircraft is used, a complex system has to be designed. If StratoMAV is mounted under the wing, a complex attachment system has to be used to resist the forces during take-off and cruise. If StratoMAV is launched from inside an aircraft, probably an even more complex launch system has to be made. For the balloon a simple launch system can be used, since it does not have to resist high loads and forces.

Regarding the previous mentioned points, the balloon is chosen as launch system. This is mainly due to the fact that the expected load factor during a balloon launch is lower.

Hereafter, the construction has to be made from which StratoMAV is launched. Since it needs an initial velocity to be controllable, StratoMAV needs to be launched under a inclination angle. This can be achieved using a truss structure in which StratoMAV can be mounted. This structure also needs a lock system, which prevents StratoMAV from sliding out of the structure. Hence, the release mechanism needs to be controlled from the ground and thus needs a receiver which releases StratoMAV.

The balloon needs to carry a payload of at least 6 kg because it is assumed to have a truss structure of atleast 1 kg. The balloon which has been selected is the HAB-3000 from Kaymont Balloons [81]. The cost of the balloon is 395$ [82], excluding helium. The balloon has a maximum altitude of $36,000\ m$ with a payload of 2 kg. With 3 kg payload, the balloon has a maximum altitude of $35,000\ m$. So there can be assumed that with 6 kg of payload, the balloon will at least reach $15,000\ m$. The balloon has an ascend rate of 5.3 m/s [81], which means it will take about 47 min to ascend to $15,000\ m$.

To launch StratoMAV at $15,000$ m, the release mechanism has to be unlocked, after which it should accelerate at full power. This has to be done to achieve a velocity higher than the stall speed such that StratoMAV can control itself. Next, it can start its mission.

The launch system of StratoMAV has to come down eventually when the balloon bursts [83]. Hence, a parachute has to be mounted on the cables which hold the launch system. The parachute has to carry the launch system, which means it has to carry 1 kg of payload. If a parachute of 1 m is used, the launch system will come down with a velocity of $16km/h$ [84]. It is assumed that the velocity is low enough to re-use the launch system of StratoMAV. The cost for the parachute is 40$. Even if a larger parachute is needed, the cost remains relatively low.

9.5 Landing System

This section discusses the StratoMAV landing system. StratoMAV should, according to the requirements, be able to land at a specified location. The landing system regards everything that is needed to descend to lower atmosphere and finally come to a standstill at ground level. As the requirements state, the UAV should have a lifetime of at least five years and have an endurance of at least a year. Therefore, StratoMAV is supposed to sustain five landings in its entire lifetime. In this section, the landing speed and landing system will be discussed.

9.5.1 Landing Speed

One of the main issues during landing is to generate enough lift while flying at a low airspeed. Most aircraft need high lift devices for this. Since StratoMAV is designed to fly at low airspeed during the entire mission, generating enough lift during landing will not be a problem. The air density during landing equals 1.225 kg/m^3, which is much higher than during cruise, where $\rho = 0.192$ kg/m^3. Therefore, the stall speed during landing is lower than during cruise. Equation 4.1 shows how the stall speed can be found. Taking the same $C_{L_{max}}$ as for cruise, which is 1.5, V_s for landing conditions equals 2.89 m/s. As described in section 4.1, the aircraft has been sized for a landing speed of 5 m/s, higher than the stall speed. This indicates that the aircraft can generate enough lift during landing and will not stall.

9.5.2 Landing System

Since weight is one of the main constraints in the design, landing gears will not be used. Such a landing system would introduce heavy solutions. The landing gears itself add weight to the design, and the points on the UAV where it is attached needs to be strengthened, adding additional weight. Instead, StratoMAV will be designed to land on its belly. This leads to some constraints for the landing site: it must be a field without obstacles and a relatively smooth surface. If there are for instance rocks on the field, the UAV will be damaged. A large grassy field or a desert seem the most useful. In order to land in this way, the belly of StratoMAV is designed in such a way that it can withstand some impacts, as can be found in chapter 5. Furthermore, the propeller is foldable, such that there is enough ground clearance. This can be found in chapter 6.

Chapter 10

System Overview

After the detailed design of the subsystems, this chapter gives an overview of the system integration and system interactions. First, the resource allocation and budget breakdown are presented. Next, the system integration and the internal configuration are shown, as well as the system interactions in the different diagrams. These include the communication flow, the hardware-software interfaces and the data handling. Finally, a risk analysis and compliance matrix are given.

10.1 Resource Allocation and Budget Breakdown

The final resource allocation and budget breakdown are given in table 10.1. It can be seen that the total weight of StratoMAV is 4.8 kg and the total material cost is €47166.57.

10.2 System Integration and Configuration

During the subsystem design, the various teams kept each other up-to-date about the dimensions, the mass and the required power of their systems. All the systems are integrated and the internal configuration has been determined. The placement of systems in the vehicle determines the centre of gravity (COG) of the aircraft, which must be checked with the static stability margin given in section 4.3. As the propeller generates a torque of 0.8 Nm during cruise, the masses should be distributed such that this torque is countered.

To determine where every part must be placed, an Excel spreadsheet calculated the contribution of each part to the location of the COG, and the COG for the complete aircraft. All design teams were asked for the optimal location of their part, which was taken into consideration. Moreover, the CATIA drawing shown in appendix J was used to check if all parts fit in the wing. As this drawing only shows the view of the XY plane, the Z component for each part was manually checked with the height of the wing at that particular position.

The x and y coordinates of all components, calculated by the Excel spreadsheet, as well as the mass moments of inertia for the aircraft were used for the flight dynamics analysis of section 4.6. For simplicity, the z coordinate is assumed to be zero for all components except for the V-tail; as the wing is very thin in comparison to its other dimensions, the approximation is made that all other parts lie in the XY plane. As can be seen in table J.1 in appendix J, the centre of gravity in x direction lies in the stability margin, discussed in section 4.3, as required.

Table 10.1: Resource allocation and budget breakdown

Component	Dimensions[mm][a]	Mass [g][b]	Power [W]	Cost [€]
Airspeed microsensor	28 x 16 x 10	4	0.01	33
PCB	53 x 24 x 4	8	0.2	300
Pitot tube	⌀4 x 80	3	-	-
GPS sensor	9.6 x 14 x 2	0.5	0.066	27
4 x Servos	17 x 22 x 8	19.6	1.5[c]	80
Modem	22.00 x 32.94 x 2.03	5	0.25-0.5	111.8
2x Antenna	102.9 x 74.3 x 0.54	27	-	100
Cables	l=11000mm	167.78	-	30
Avionics system		**234.9**	**2.276**	**681.8**
Main wing airframe	459x6884x41.3	695	-	596
Tail airframe	195x1540x600	121	-	119
Joining material	-	100	-	20
Airframe	1895x6684x600	**916**	**-**	**735**
Li-ion battery	97 x 190 x 10	2190	-	253.0
Solar module Middle	159.5 x 3626 x 0.1 [d]	184	-	12166.7
Solar module Left	159.5 x 3626 x 0.1[d]	184	-	12166.7
Solar module Right	159.5 x 3626 x 0.1[d]	184	-	12166.7
Coating	478.5 x 10878 x 0.013[e]	201.83	-	210
MPPT	42 x 42.5 x 9	165	-	100.0
2x Converter (to 5V)	21.85 x 10.66 x 9.2	9	-	27.92
2x Converter (to 3.3V)	10.0 x 20.3 x 25.4	26	-	30.1
Power system		**3159.83**	**-**	**37121.12**
4x Spectrometer	27.6 x 13 x 16.8	36	0.12	2000
Thermal camera	40 x 22.00 x 22.00	21.5	0.92	6324
Processor	16.10 x 16.10 x 1.4	5	0.47	1
Payload System		**62.5**	**1.51**	**8325**
Insulation Material	1140x582x3	110.5	-	122.00
Active thermal heating		143	6.9	49.50
Thermal control		**253.5**	**6.9**	**171.5**
Brushless motor	⌀27.7 x 35	69	54	74.7
Motor controller	28 x 17 x 7	9	-	34
Gearbox	77 x 55	46	-	8
Propeller	77.5 x 52 23	43	-	15.45
Propulsion Group		**167**	**54**	**132.15**
Total at take-off		**4760.73**	**64.69**	**47166.57**

[a]Dimensions are given per unit
[b]Total mass of the components (not unit mass)
[c]This is the maximum power required at maximum deflection
[d]The dimensions given here correspond to a rectangular configuration.
[e]This is the dimension of the coating as one plate.

10.3 System Engineering

During the design process, the subsystems were designed by different groups. This could have led to conflicts during the system integration. To avoid problems and to ensure that the product meets its

requirements, a system engineer was given the task to act as communicator between the design teams. He has to analyse the changing design choices and their influences on other subsystems. In this way, the team was able to keep an overall view on the design. The following subsystem groups were identified: the aircraft design, stability & control group, the structures group, the propulsion group, the payload and telemetry group, the avionics group, the thermal control group and the power group. The most important design parameters that could influence other subsystems were identified for each subsystem. In figure H.1 in appendix H, a flow diagram of these parameters can be found, and their influence on other subsystems. Three main parameters that influence all subsystems are: mass, cost and location. Fixed mass and cost budgets were distributed and two subsystems could not be placed at the same position. These three parameters are not connected to each subsystem in the flow diagram to keep this clear.

The subsystem design started with the design of the wing planform. Airfoil, wing area and aspect ratio had a direct influence on the design of the structure. Any changes in these parameters had to be communicated to the structures group, that used the values in their design. If the given values were not structurally feasible, the aircraft design group had to redesign. Cruise speed and altitude affected the propulsion system. These parameters could be changed by the propulsion group, which had to be communicated to the aircraft design group. Finally, the cruise altitude had an influence on both the payload and telemetry design. After the wing design, propulsion, avionics, telemetry, payload and structures were designed. The propulsion, telemetry, avionics and payload system calculated their required power. This had an effect on the power system. According to the power requirements, a battery was selected which then gave a battery mass. It was checked if the mass was within reasonable bounds, if not, the required power had to be reduced. It was found that the power system's total mass would be a problem, which was notified to the other design teams. They were to reduce the mass of their subsystems accordingly. The structures group drastically decreased their weight to compensate the battery mass, by decreasing the load factor used to design the structure.

During the detailed design, subsystem hardware devices were chosen. The operating temperature of the battery, spectrometers and modem had to be considered, as this was different from the ambient temperature. Therefore, the thermal control system had to be designed. It was chosen to have a combination of passive and active heating, so the thermal subsystem required a certain amount of power. This was communicated to the power design team, which needed to verify whether this was possible. At the same time, the stability and control of the UAV was considered. The stability derivatives were calculated and checks were made if StratoMAV was statically and dynamically stable. In case the stability characteristics were not as desired, the aircraft layout was adjusted. The stability and control group designed the control surfaces as well. The control surfaces have an effect on the structure and the avionics. The avionics group designed the servos, which depend on the size of the control surfaces. Small indirect design choices were made as well, such as voltages of the hardware. Because the voltages need to be matched, converters were added. A communal spreadsheet was made in which all the important parameters, such as mass, cost, wing dimensions and power requirements of all subsystems were listed. In this way the entire design team could keep an eye on changing parameters.

10.4 System Interactions

The interactions of the system are described in different ways. First of all, there is the communication flow between subsystems and between the components within them, shown in the Communication Flow Diagram. Next, there is the interaction between hardware and software, given in the Hardware-Software Block diagram. Lastly, there is the Data Handling diagram that describes the data flow between the hardware components.

10.4.1 Communication Flow

For the entire UAV, the communication flow diagram as shown in figure 10.1 gives a general overview of the communication flow in the system. It should be read together with the communication flow diagrams of the power, payload and autopilot subsystems which can be found in appendix I. The most important element in the communication flow is the command and data handling system. This has been implemented in the UAV by following the two-processor architecture as proposed in the paper of R. Klenke [39], which is further described in the Hardware/Software section and the Data Handling section. The external input data that the system receives are shown, as well as the output data. The most important task in the communication flow is sending the right data to the right subsystems.

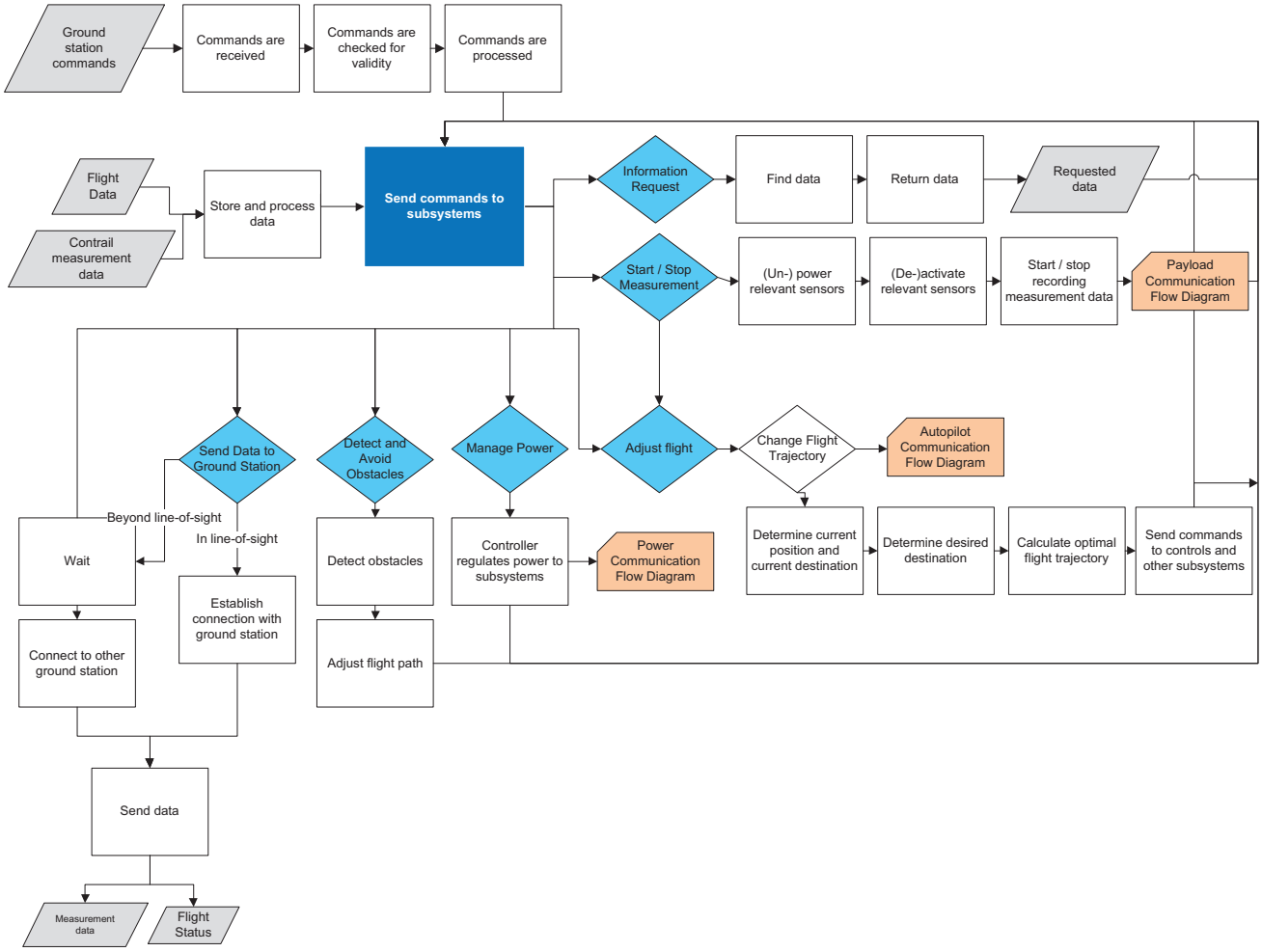

Figure 10.1: Communication flow diagram of the StratoMAV system

Hardware-Software Interaction

StratoMAV should fly autonomous, which is accomplished by using software programs. This section analyses the interaction between the software and hardware components. In figure 10.2, StratoMAV's Hardware/Software block diagram can be found. The software is grouped together in blocks related to their corresponding processors. The arrowed lines indicate the physical connections, while the lighter

lines without arrows show data relations. For example, the Data Manager stores data from the spectrometers in the data storage, but the data storage is not physically connected to the spectrometers. Not all physical connections are shown (such as the power connection from the batteries to all subsystems) to ensure clarity and to only show the connections relevant to the data processing. More

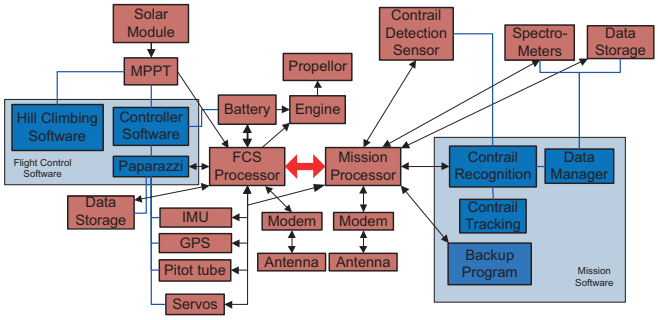

Figure 10.2: Hardware & Software block diagram

information about the power operations and chosen hardware can be found in chapter 7.The Flight Control System(FCS) controls the avionics and is operated by Paparazzi. More information about the autopilot operations and the related hardware can be found in the autopilot section 9.2. The FCS is linked to the mission processor. The mission processor is used to operate the payload system and telemetry. The mission processor also is a backup processor which can take over in case the FCS fails. The backup process is controlled by a backup program, which is connected between the FCS and the mission processor. The mission processor processes the spectrometer data and stores it on a data storage device. The data processing software is in charge of incoming and sent data. It calculates how much data has to be sent and how much can be received. More about the payload operations and the chosen hardware can be found in the payload chapter 8.

Measures and Redundancy

The impact of electronics failure can easily be reduced by adding redundant components, backups and debugging features. For this reason the critical electronic components have backups, these are: the RF module and antenna, the data storage and most importantly, a second processor. Because the autopilot processor has complete control over the UAV, its failure would be desastrous. This failure impact is greatly reduced by the dual processor architecture in which the connection between the two processors is of key importance. Each processor will check continuously whether the other processor is still working. If one of the two fails or is unresponsive, the other takes over all the main tasks, resets the other processor (possibly debugs it) and restores the programs that were originally in the processor. This process is known as a ”watchdog timer” and is software implemented in StratoMAV. All the programs used in StratoMAV are stored at multiple locations such that recovery is always possible if either a processor or data storage device fails. These locations are: the two data storage devices and the flash memory in each processor, which makes four locations in total. The mission processor also has an integrated watchdog procedure, error-correcting code and a dual CPU architecture which even further reduces the risk of failure of this processor (see the Payload chapter, chapter 8. Each processor is connected to its own data storage device, RF module and antenna. During normal operation the antennas can both be used in an array to improve gain and directivity.

10.4.2 Data Handling

Data handling involves the data transfer between hardware components. These are shown in figure 10.3. It shows how the components of the data handling system receive and send data, as well as properties of the components such as the clocking frequency in MHz or the data storage capacity. When information had been given about the data handling properties in the specifications sheets of the components it was included in the diagram. Between the Flight Control System(FCS) processor and the mission

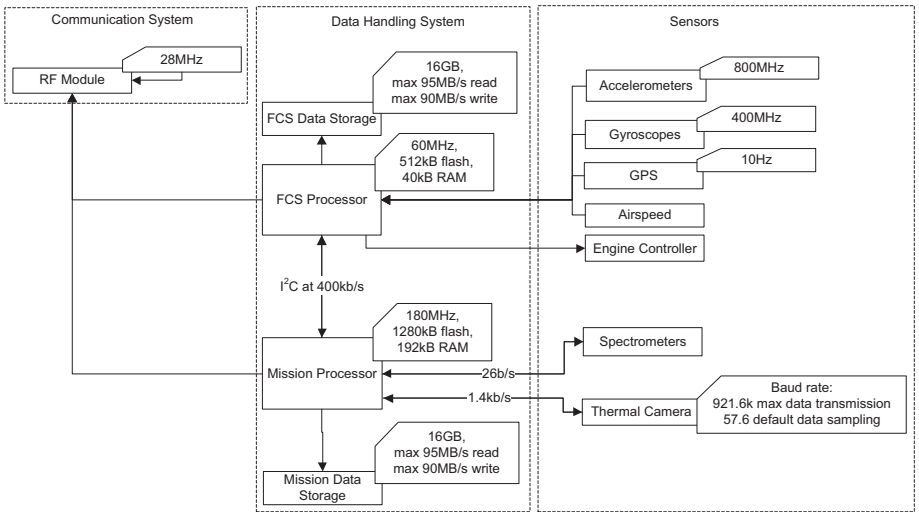

Figure 10.3: Data handling block diagram

processor a I^2C (Inter-Integrated Circuit) serial communication link was chosen with a maximum data rate of 400 kb/s, because the connection is required for the backup program. The sensors will have to be connected to the processors on a custom designed board. All the components should be together as close as possible to reduce losses in wiring and increase data rates. Of the spectrometers and the thermal camera the output data rate to the mission processor is given, as calculated in chapter 9.1. In the specifications of the thermal camera the baud rate was given [66], which is the symbols per second, or pulses per second(uncompressed data).

10.5 RAMS and Technical Risk

RAMS characteristics describe how the UAV has been designed in terms of reliability, availability, maintainability and safety (RAMS). This is partly done by comparing elements from StratoMAV's design to existing UAVs. From the RAMS characteristics, a risk map is constructed.

10.5.1 Reliability

Reliability is the ability of a system to operate correctly for a given time under specified environmental conditions. StratoMAV has to perform its mission for at least a year, during which no maintenance can be carried out. This means that all components have to function for at least a year under the stratospheric conditions. For the most important aircraft subsystems, the expected reliability will be discussed.

Payload

The sensors are sensitive to vibrations, power overload and extreme temperatures. While they are important for the scientific mission, the sensors do not have an influence on the UAV's ability to sustain flight. Cameras have been carried on board of UAVs before, as for example the intelligence and surveillance UAVs used by the American military. The chosen sensors have been tested in laboratories and operating temperatures are given in the specification sheets. It is unknown what the long term effects due to the low density, low temperature and ozone have on the sensors.

The possible failure modes of the payload are:

- High vibrations applied to the sensors causing failure
- Short circuiting
- Structural damage
- Environmental damage
- Software failure

Effects. Any damage to the sensors will affect the quality of the collected scientific data, if the sensors still work at all. Payload failure will mean the end of the scientific mission but the UAV will still be able to land, so the payload could be replaced or repaired and the mission can be resumed. The UAV must be able to send a message to the ground station about the status of its sensors.

Criticality. Failure of the payload will not lead to a crash of the UAV. However, the mission must be aborted if failure occurs. Therefore, the criticality is *medium*.

Redundancy. The payload consists of two pairs of two spectrometers, one contrail detection sensor, one processor and one memory card. One pair of spectrometers measures the contrail, and the other pair measures next to the contrail. If one spectrometer fails, the other of the pair can continue measuring. If a pair fails, the UAV must fly in a pattern to measure above and next to the contrail. This requires more power for propulsion. If the contrail detection sensor fails, this task could be continued by the ground station which detects contrails from the ground, sends the UAV to the right location and sends a command to perform measurements. This requires more communication and man power at the ground station. If the processor fails, the measured data can be stored and downlinked, but the ground station must process the contrail detection data and send the UAV to the right location.

Structures

The structural design is conventional, with a wing consisting of skin, one spar and ribs. A load factor of 2 is taken and the weight of subsystems in the wing are not taken into account in the loading scenario. The structures are designed to meet the deflection requirements. The material used is a combination CFRP and balsa wood, which is a proven concept.

Possible failure modes of the structure are:

- Fatigue of a structural part
- Buckling
- Delamination
- Cracks and fractures
- Environmental damage (e.g. from thermal stress, chemical reactions or gusts)
- Collision damage (e.g. during ascent and landing)

Effects. Structural damage can have different levels of severity. It might be possible for the UAV to fly with minor structural damage such as scratches. Critical structural damage would include major damage to the wing spars, ribs or skin, to the propulsion subsystem or to the protection of the other subsystems.

Criticality. As minor damage will not crash the UAV, but more severe damage will, the criticality is estimated at *low to high*.

Redundancy. Redundancy has not been applied, as it is not possible to include multiple structural elements as a back-up due to the weight restriction. However, the structure has been designed for certain deflection requirements, which means that higher loads than the one designed for will not directly result in failure of the structure.

Propulsion

The propulsion design consists of one propeller driven by an electric motor. It has two blades, a fixed pitch and a gearbox. Main risks for the propeller and the electric motor are fatigue of the moving parts and structural failure. Electric motors also have risk of overheating.

The possible failure modes of the propulsion system are:

- Overheating of the motor
- Obstruction of the motor or propeller
- Structural damage to the motor or propeller
- Excessive wear (e.g. bearings which increase the power)

Effects. A damaged propulsion subsystem means that StratoMAV can no longer sustain flight and needs to abort its mission. However, a broken propulsion system does influence other systems. Therefore, a message about the damaged propulsion system can be sent to the ground station, which can give the command to glide to the ground.

Criticality. The criticality of a propulsion system failure is *high*, as the mission needs to be aborted.

Redundancy. It has been decided to use one propeller to reduce weight, while two or more propellers would have been better for redundancy. The propeller is slightly over-designed, such that it is more likely to cope with fatigue and unsuspected loads.

Power

The power subsystem consists of solar cells, batteries, MPPT and converters. They have been designed such that during the worst case scenario (day with least amount of sunlight), StratoMAV can still operate. It has been proven that solar cells can operate for a long time (for example in spacecraft), but degradation does occur. Regarding the batteries, Lithium-ion batteries are a proven concept, but as the batteries have a new electrolyte design, their reliability is unknown.

The possible failure modes of the power system are:

- Critical solar cell degradation
- End of battery life (too low capacity)
- Battery leakage

- Overheated or under-cooled batteries
- Short circuiting
- Damaged MPPT
- Damaged converters

Effects. A permanent failure of the entire power subsystem will result in a crash, as the UAV will become uncontrollable and will not be able to land safely. If the power level is too low to perform its mission, but the rest of the power systems still works, the UAV may glide to the ground and use its last energy to stay controllable and land safely. In such a case the UAV could be recovered and repaired or parts could be reused. If the batteries fail, the UAV may be able to land on solar power only; however, if they fail during the night, the UAV will have to glide uncontrollably. The possibility of a crash is high in that case.

Criticality. The criticality of power system failure is *very high*, as it will lead to a crash in most cases.

Redundancy. Battery cycles and solar cell degradation have been taken into account such that the power subsystem can operate for a year. The storage system and solar cells have been designed to deliver enough energy with a safety margin of 5%. For the MPPT no redundancy has been applied. As three MPPTs are used, this would have a significant effect on the weight. Only the lightweight converters are made redundant. StratoMAV uses two converters, which are connected between the batteries and subsystems. For each converter an extra converter is added: in total StratoMAV will have 4 converters. A thermal control system is also included in the design. Short circuiting can be avoided by correct circuitry design and protection of the battery is provided to avoid structural damage (puncture for example).

Telemetry

The importance of the telemetry subsystem is not so much related to the UAVs flight but to the task to communicate any error messages, to receive commands from the ground station and to send the collected scientific data. The telemetry subsystem is sensitive to the same factors as the payload. Transceivers and communication parts such as antennas and receivers have been tested on many aircraft and spacecraft flights of aircraft and spacecraft. It has been proven that they can operate at high altitudes.

Possible failure modes of the telemetry subsytem are:

- Short circuiting
- Structural damage
- Environmental damage
- Software failure

Effects. Damage to the telemetry subsystem will endanger the UAVs flight, but failure will make any communication between the UAV and ground station impossible. This will cause any errors on board of the UAV to be unknown to the ground station and the UAV cannot receive commands any more, such as where to measure or to land. In this case, the UAV is preprogrammed to land at the ground station location once it detects failure of the telemetry subsystem or is not able to establish a connection with the ground station for more than 12 h. Then the UAV can be retrieved and repaired.

Criticality. Failure of the telemetry subsystem will not cause major problems for the UAV. However, the science mission cannot be carried out properly any more. Therefore, the criticality is *medium*.

Redundancy. Data storage makes it possible to store error data and measurement data while communications are not possible. When the communications link is restored, the data can be sent anyway. All other permanent failure will mean that the communication link is lost. It is not possible to have a second telemetry system on board due to the weight constraint. However, an extra modem is added, which can take over if the main modem fails. The system must be aptly protected to avoid structural damage or environmental damage, and designed such that risks of short circuiting and software failure are minimized.

Autopilot

The autopilot system is crucial for sustaining flight, but also for performing the science mission. The autopilot must be programmed with precision and thoroughly tested to minimize the chance of failures. The sensors of the autopilot can survive lower temperatures than their operating temperature, but might not work until they are up on the correct temperature. Power overload is a risk for the autopilot system.

Possible failure modes of the autopilot are:

- Short circuiting
- Environmental damage
- Power overload
- Temperature shocks
- Vibrations

Effects. Any damage to the autopilot will cause problems in controlling the aircraft. A failure in the processor can be resolved by using the payload processor as a back-up, but processing the payload data would be slower. Failure of one of the sensors will mean that the autopilot controls the aircraft with a reduced accuracy. Failure of all sensors will leave the aircraft uncontrollable, which means it will probably no longer be able to make a safe landing and will crash.

Criticality. Failure of the entire autopilot system will cause the aircraft to be uncontrollable. Failure of the controller and of one sensor will only reduce the accuracy of control of the aircraft, or the processing speed of the payload data. Failure of all sensors would crash the aircraft. Therefore, the criticality is *medium to high*.

Redundancy. The processor of the payload will be programmed such that it can replace the autopilot's processor if the latter fails. This means that processing the payload data will be slower, so the UAV will no longer be able to track the fastest contrails. However, most contrails will still be measurable and the aircraft will still be controllable. Moreover, multiple sensors are installed, including an additional airspeed sensor. This sensor can be used to calculate the position of the aircraft and as an altitude indicator. If a sensor of the autopilot fails, the processor lacks information but can still control the aircraft. If all sensors fail, which is unlikely, the aircraft will become uncontrollable, cannot land any more and will crash.

Ascent and Landing

The UAV will ascend to mission altitude assisted by another vehicle. The loads from the assisted ascent have not yet been be taken into account in the structural design. However, this needs to be considered

for an improved design, as the UAV should perform at least five ascents in its lifetime. Additional loads from a controlled landing or an emergency landing have been taken into account in the design.

Possible failure modes for ascent and landing are:

- Control failure
- Structural failure
- Power failure
- Electrical failure
- Software failure

Effects. Damage occurring during the ascent would ruin the entire UAV's mission from the start and the UAV should immediately be sent back to the ground again. Damage from the landing would be less critical as it can be repaired before it is sent back up again. However, it reduces the UAV's lifetime and requires more repairs and maintenance.

Criticality. A failure during both ascent and landing can have a *high* criticality, as the vehicle might crash. However, minor failures can also occur, which will only require repairs. This would mean a *low* criticality.

Redundancy. Sufficient tests, proper maintenance and check ups should be carried out before launch and ascent. Before the ascent it should be checked whether the power subsystem works, the control subsystem works, the communications subsystem works, etcetera. Then the ascent can be carried out safely, but the ascent time and location should be chosen carefully to reduce the risk of damage to the UAV during ascent. The structural design should be able to cope with the additional loads from ascent and landing into account.

10.5.2 Availability

Availability is defined by the time that subsystems are able to operate and perform their task sufficiently. It is guaranteed through high reliability. In case of no failures, the availability of the subsystems is largely dependent on the available power. At night, less power is available to carry out long measurements, as a large part of the power goes to telemetry and propulsion. During day, the amount of power consuming tasks that can be carried out at the same time are limited as well. If not enough power is available, it might be possible that measurement taking, complicated flight patterns and data tranmission cannot be carried out simultaneously and must be postponed.

10.5.3 Maintainability

Since maintenance can only be carried out on the ground, it can be done after a year of flight. As described in section 11.1, the UAV is transported to a base where maintenance can be carried out after it has landed. All the parts that should be replaced after a landing are those that have an expected lifetime of less than two years, since it cannot be guaranteed that they will survive the next flight. All the other crucial parts should be checked before the next flight and any anomalies that occurred during the flight should be analysed before the next flight. In case of an emergency landing, the subsystem that caused the problem should be checked thoroughly such that a subsequent failure of the same subsystem can be avoided.

Parts that are most likely to be maintained or replaced after every flight are parts of the battery and the solar cells, since their efficiency degrades over time. To meet the strict weight restriction the batteries

and solar cells have to operate at peak efficiency. Next, the structural parts should be checked for signs of fatigue or possible failure locations. Since most of the used parts are off-the-shelf products, those can easily be acquired and replaced. In the future after several years of flight, even better off-the-shelf components could be chosen to replace the older components. This is less easily done for custom manufactured carbon fibre structures and custom assembled electronics parts.

10.5.4 Safety

During its operations, StratoMAV will pose little danger in the stratosphere to other vehicles or humans. Only if it crosses commercial airspace it will have to deal with air control and collision avoidance. Dangerous situations could be created when the UAV becomes uncontrollable by one of the previously mentioned failures in the subsystems. The UAV could crash at a disadvantageous landing site or it could collide with other airborne objects. Since the UAV does not carry fuel aboard, explosions are not likely to happen except if the batteries are suffering damage or overheating. Small amounts of hazardous materials are contained in the sensors. The solar cells and composite structure do not pose a direct threat to humans.

10.5.5 Technical Risk

In table 10.2, the values of the technical risk of each subsystem are found. These values are plotted in figure 10.4. The upper right subsystem has the most risk and impact. It can be seen in figure 10.4 that this is the power system. Therefore, the power system has been designed with wider margins and safety factors. For the batteries, it is assumed that all systems are active during night, while this is not the case. Also, a safety factor of 5% is used.

Subsystem	Probability	Impact
Payload	2	2
Structure	1	5
Propulsion	2	3
Power	2	5
Telemetry	2	2
Autopilot	1	5
Landing	1	1

Table 10.2: Risk assessment of subsystems

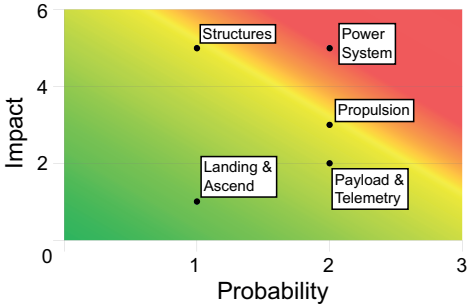

Figure 10.4: Risk map of the subsystems

10.6 Compliance Matrix

The compliance matrix is a table with tick marks for all the requirements that have been met, shown in table 10.3. If a requirement has not been (fully) met or an explanatory note is required, an explanation is given below.

- **Minimum life time of 5 years**: While it is expected that some parts will have to be replaced during maintenance after a year, it can not be said for sure that StratoMAV will have a life time of 5 years. Where information was available, components where chosen with a life time of at least 5 years. Additional calculations would have to be performed on the fatigue properties of the structure and the effects of the stratosphere on the used materials, as well as tests.

- **Measurements on net photon flux from Sun and Earth**: It was chosen to only measure the solar and terrestrial radiation coming from the Earth towards StratoMAV. The solar radiation from the Sun to StratoMAV is not measured, because it can easily and reliably be modelled with existing data packages from satellites. This design choice saved weight and reduced the necessary power consumption.

Table 10.3: Compliance matrix of StratoMAV, showing the requirements that have been met $\surd = achieved$, $\tilde{} = partiallyachieved$, $- = notachieved$, $? = unknownyet$

Requirement	Achieved	Chapter
Minimum cruising altitude of $15,000m$	$\surd$	Section 4.1
Minimum loiter time $365days$	$\surd$	Chapter 7
Station keeping in wind up to $15m/s$	$\surd$	Section 4.1
Autonomously fly an optimal trajectory for science observations	$\surd$	Section 9.2.7
Autonomous precision landing on a predefined area	$\surd$	Section 9.5
Minimum life time $5years$	?	Section 10.6
Able to take measurements on the net photon flux received from Sun and Earth	$\surd$	Chapter 8
Spatial and spectral resolution sufficient to distinguish between natural reflectance sources and contrails	$\surd$	Chapter 8
Sufficient pointing accuracy to make simultaneous measurements on light coming from above and below	not relevant	Section 10.6
Measure in $400nm - 750nm$ and $750nm - 1000nm$ ranges	$\surd$	Chapter 8, Section 10.6
Obtained data is transmitted to a mobile base station	$\surd$	Section 9.1
StratoMAV operations should not interfere with commercial airline operations	$\surd$	Section 10.6
StratoMAV failure should not interfere with commercial airline operations	?	Section 10.5, Section 10.6
Reliable operation time of $365days$	$\surd$	Chapter 7
Solar powered	$\surd$	Chapter 7
Lost StratoMAV does not pose an environmental threat	$\sim$	Section 10.6
Maximum weight $5kg$	$\surd$	Table 10.1
Data transmission is sufficient for near real-time transmission of sensor data	$\surd$	Section 9.1
Data transmission signal gain is sufficient to receive data from a road-worthy mobile ground station	$\surd$	Section 9.1
StratoMAV's mission profile is designed	$\surd$	Subsection 3.1.2, Chapter 8, Chapter 7
StratoMAV's maximum turnaround time $1day$	?	Section 10.6
StratoMAV's maximum cost €$50,000$	$\surd$	Section 10.1

- **Sufficient pointing accuracy to make simultaneous measurements on light coming from above and below**: As just mentioned previously, the light from above will not be measured. Also, the payload sensors are not actively pointed, because that would require a much more complex system. Contrail measurements are taken by flying horizontally straight above a contrail.
- **Measure in** $400nm - 750nm$ **and** $750nm - 1000nm$ **ranges**: The payload sensors measure in the specified ranges and more. First of all, the chosen spectrometers measure in $340nm - 750nm$ and $640nm - 1050nm$, which means that more wavelengths are covered at the beginning and end of the ranges and there is a small overlap around $700nm$. Secondly a thermal camera was deemed necessary to measure the terrestrial radiation at night. It measures in the $7.5\mu m - 13.5\mu m$ range.
- **StratoMAV operations should not interfere with commercial airline operations**: During cruise StratoMAV will be operating above commercial airspace. As a launch system a balloon was chosen in chapter 9.4. There it is determined that the total time to ascend from ground level to $15km$ altitude is about $47min$, so about half that time is spent in commercial airspace. The launch and landing times can be chosen by the ground station to avoid or minimize interference with commercial airline operations.
- **StratoMAV failure should not interfere with commercial airline operations**: Wherever possible safety measures and redundancy have been applied in the design. This means that a total system failure is highly unlikely, in case of failure StratoMAV will operate with reduced functionalities. In most cases it is still able to carry out a controlled glide, unless structural failure to the wing occurs. An overview of StratoMAV's risks and safety measures is given in chapter 10.5, the detailed safety measures taken per subsystem can be found in their respective design chapters.
- **Reliable operation time of** $365days$: As for the life time of 5 years, the reliable operation time of $365days$ can not be guaranteed without further calculations and testing, but StratoMAV has been designed to operate for one year continuously.
- **Lost StratoMAV does not pose an environmental threat**: The most environmentally hazardous material is contained within the lithium-ion batteries, which was necessary to make StratoMAV solar powered and sustainable. In case of a crash, battery leakage should be prevented by its encapsulation. Next to the batteries, traces of heavy metals are contained in the electronics.
- **Data transmission signal gain is sufficient to receive data from a road-worthy mobile ground station**: The uplink calculations have not been performed, but it is assumed to be sufficient.
- **StratoMAV's maximum turnaround time** $1day$: The required turnaround time should be determined from a maintenance simulation in real life, trying different scenarios. At the moment a turnaround time of $1day$ has been assumed, but the precise turnaround time is unknown.
- **Maximum cost** €$50,000$: A resource allocation has been made including the costs of all components. However, since not all costs not were known some costs were estimated. The total cost is about €$50,000$, not including development and manufacturing cost.

Chapter 11

Design Implementation

This chapter describes how the design of the UAV is implemented. It includes a description of the operations and logistics of StratoMAV, a market analysis and a cost analysis. Moreover, the sustainable development strategy is presented. Finally, the implementation plan is described, which includes a production plan, the project design and development logic and a post-DSE, project Gantt chart.

11.1 Operations and Logistics

This chapter discusses the logistical and operational matters of StratoMAV's mission. First, the logistics of the ground station will be elaborated upon. After this, the maintenance plans for the UAV will be described. Finally, the transport issues for StratoMAV are discussed.

11.1.1 Ground Station

As one of the requirements for StratoMAV's mission is to have a mobile ground station, the logistics of this station must be looked into. The UAV has a limited range in which it can transmit and receive information, which is determined to be 50 km (see section 9.1) from the ground station. It must be placed such that the multipath loss is limited, so preferably in an open field. Furthermore the ground station must be roadworthy.

The UAV will be taking measurements between 0° and 52° latitude, above Europe. This means that the ground station will not encounter any extreme environments. However, it must be able to relocate itself from 0° to 52° latitude (or the other way around) in one week (see section 7.3). Preferably, the ground station can also follow the UAV and establish a data link as it flies from one location to another.

Moreover, the ground station must be able to carry the receiver antenna and all other equipment. As can be found in section 9.1, the receiver antenna has a diameter of 2.5 m. This puts a constraint on the size of the ground station.

Taking the requirements described above into account, it is decided to use a ground station in the form of a truck. This truck should be large enough to carry the antenna, and it must be able to move fast enough to cover a 52° latitude change in one week. Using a truck makes it possible to follow the UAV and communicate with it while it relocates. However, the equipment can be designed in such that it can be easy to detach from the truck. In that way, it can be placed on another vehicle, if a truck is not able to reach the new mission location.

11.1.2 Maintenance

When StratoMAV lands after a mission, it will require maintenance. As the UAV has a large span and is delicate, the maintenance location needs to be chosen carefully; it needs to be spacious enough and the UAV should not be in danger of being damaged. It would also be very efficient to maintain the vehicle in a location where engineers of all the different fields (solar cells, structures, power supply etc.) are nearby, or a location that is easy to travel to.

For the logistics of maintenance, the following should be considered. The first thing, after the UAV has arrived in the workshop, must be to inspect the UAV for apparent damage. This needs to be documented well and repaired. Next, the vehicle must be more closely inspected by engineers of each field of expertise, for less apparent damage. The maintenance issues must be placed in an order of importance, after which the maintenance on the UAV can start.

When all issues have been solved, the UAV must be thoroughly tested to ensure that all damage has been fixed. When this is done, the UAV is ready for its next mission. All of the previous stated issues have to be performed within at most one day since this is a top level requirement. Hence, all tools and specific replacement parts have to be at the maintenance location before the StratoMAV is landed.

11.1.3 Transport

Transporting StratoMAV is an important issue, as there is a chance that the UAV is not able to land or ascend near its maintenance location and will have to be repositioned by another vehicle. The UAV has a large span, which makes this a logistical challenge. A large span means that a large truck must be used to move StratoMAV. A large truck will not be able to reach very remote areas. The ascend and landing spots must therefore be chosen such that they are well accessible by road. As StratoMAV is a very lightweight UAV, it is possible to have people carry it to a truck, for example when it has landed in a field.

If the UAV lands overseas from its maintenance location, the UAV must be transported by an aircraft, as a boat will be too slow due to its turnaround time of one day. This will only happen if the UAV needs to make an emergency landing; otherwise, it will receive commands to fly to a convenient location.

11.1.4 Storage

When StratoMAV is stored, it must be carefully placed in a location where it cannot be damaged. Ideally, the UAV is placed on a rack above the ground. This will reduce the probability of being damaged, and it easier to access the vehicle for maintenance.

11.1.5 Conclusion

It can be concluded that the ground station must be able to reach a location from where it will possible to establish a data link of sufficient quality. This is done with the help of an external mobile vehicle: a truck. Furthermore, all issues involved in the maintenance must be performed in one day. This requires a maintenance location that provides the ability to store all tools and specific replacement parts. Moreover, ascend and landing spots must be accessible by large road vehicles. Finally, the UAV must be safely stored on a rack above the ground.

11.2 Cost Analysis

In this section, first the costs for each subsystem are listed in the Cost Breakdown Structure and it is discussed whether the costs could be reduced. Moreover, the return on investment of StratoMAV is reported.

11.2.1 Cost Breakdown Structure

In table 10.1 in chapter 10.1, the costs of each subsystem is listed. StratoMAV has a financial cost budget of €50,000 and a mass budget of 5 kg. The price of the materials for building StratoMAV is €47,200. Approximately 89 % of the financial budget is spent on the solar cells and contrail detection sensor. The remaining is spent on the structure, propulsion system, avionics and telemetry. The production costs, development costs and ground station costs are not included in the cost breakdown structure.

The total costs could be reduced in a redesign of StratoMAV. The chosen solar cells are particularly expensive. In the future batteries with higher specific density will be available. This will reduce the weight of the battery system, which will mean more solar cells could be installed. Heavier but cheaper solar cells can be used with the same efficiency and cell area. A possibility is the Conrad solar cell, which is approximately 30 times less expensive than the s-32 solar cells. This could decrease the current solar module cost of €35,000 to €1,200. Note that using this solar cell will require a redesign of the the power system.

The contrail detection sensor is relatively expensive compared to the other subsystems. The main reason is that there is no competition on the market for lightweight UAV sensors. The company selling the thermal sensors can set the price as high as they desire. In the future, micro UAV development is expected to increase. The demand for lightweight sensors will increase, which will give rise to more competition on the sensor market. As a consequence, the sensor prices will drop.

Also, the thermal sensor cost is related to the number of sensors requested. If many thermal sensors are purchased, the price per unit is reduced to €4,000.

11.2.2 Return on Investment

Any return on investments, as the word implies, require numbers on the expected returns and the expected investments.

Investments

The StratoMAV construction comprises more than solely material costs. In order to get all proposed tasks done, as the post-DSE Gantt chart shows. A 10-headed team of engineers is required up till April. Based on an avarage salary of €4,000 a month, the further concept development would cost $(2 * 10 * 4000 =)$ €80,000. Extended testing and hiring a 10-headed team of engineers for another half a year would cost an additional €240,000. Third party advices, prototype production facilities, prototype testing plants, and patent requests are expected to take another million euros. Please bear in mind that the total ground station development and production is estimated at at least a million euros. A single StratoMAV would cost €47,200 based on material costs. Assuming 100 labour hours (cheap labour forces are available for €20 per hour) and another $\frac{1}{5}^{th}$ of material costs are accounted

for tool costs per unit cost. A total StratoMAV would have a cost price of €59,000. Applying a 40 percent margin, StratoMAV will be a bargain for low cost earth observing applicancies, costing only €82,600.

Returns

Subtracting the production costs from the selling price, one can deduct a €24,000 profit per unit. It is expected that the first year, one StratoMAV is sold. This will prove its specific financial superiority, and will subsequently conquer the low end earth observation industry. Second year, 10 StratoMAVs are expected to be sold. In the next year 25 unit are expected to be sold. Because different payload sensors can be used the market is fairly high. It is therefore expected that in the following years 25, 35 and in the fifth year 40 units will be sold.

The StratoMAV development costs is estimated to be 2.32 million euros. This would imply that in the fifth year, the project would reach break-even. Following the expected selling rates the revenue over the first 5 years would be €9,168,000. The total investments up until the fifth year are €8,829,000. The profit is then€339,000.The return of investment computation can be calculated using equation 11.1. In the next 5 years 50 units per year are expected to be sold.

$$ROI_{5years} = \frac{Profit}{Investments} \approx 3.8\% ROI_{10years} = \frac{Profit}{Investments} \approx 26.9\% \tag{11.1}$$

Which indicates that this project is expected to break even in the fifth year and long term the project is a good investment.

11.3 Market Analysis

A market analysis is based on comparable products in terms of application, requirements and product cost range. This chapter describes the market analysis carried out for StratoMAV's mission. It was discovered that there are no other products that completely meet its requirements. Nevertheless, there are products on the market that are comparable and meet some of the requirements of the current project. These are first discussed below, after which the competitors of StratoMAV can be identified and StratoMAV's competitive position is determined. Finally, spin-off markets for StratoMAV are discussed.

11.3.1 Satellites

Satellites have been widely used to monitor locations for a long time. The number of launches of Earth observation satellites is expected to double between 2010 and 2019 from 135 to 280. These include both commercial and civil Earth observation satellites. The revenue generated from this growth is expected to be 26 billion U.S. dollars for the satellite manufacturing sector in the coming decade [85]. StratoMAV would be able to tap into this growth and take a share of it for its account. For Earth observation missions, satellites stay in orbits ranging from 180 to 2000 km [86]. Therefore, they are not able to measure contrails with the same level of detail as StratoMAV.

11.3.2 Unmanned Aircraft

Unmanned aircraft are categorised based on mission, endurance and altitude. The unmanned aircraft that resemble StratoMAV, are High Altitude Long Endurance (HALE) unmanned vehicles. The world-wide UAV market expenses, for all types of UAVs, are around 6.6 billion U.S. dollars per year in 2012. It is expected that in the next decade it will increase to 11.4 billions U.S. dollars [87].

The existing HALE UAVs that come closest to our objective are NASA's Pathfinder, Pathfinder Plus and Helios. These aircraft were developed by AeroVironment, Inc., for NASA's Environmental Research Aircraft and Sensor Technology Program. Pathfinder and Pathfinder Plus were solar powered, remotely piloted aircraft, the first designed to perform high altitude surveillance missions and the second to validate new technologies for solar aircraft [50]. Helios was developed to demonstrate sustained flight at high altitude (30 km) and non-stop flight for at least 24 hours. Unfortunately, it deteriorated in mid-air during testing [88]. Unit costs for these aircraft are unknown.

Another similar concept is Sky-Sailor, a concept designed to autonomously explore a section of Mars, completely powered by solar energy. This design aims to achieve continuous flight, mainly depending on solar energy and batteries as an energy buffer. The target product speed is about 30-40 m/s, weighing about 2.5 kg [10].

QinetiQ Zephyr can also be considered as a comparable unmanned aircraft. This vehicle had a mass of 40 kg. It has reached a flight time of 82 hrs and used solar energy to power the engines. Zephyr reached a maximum altitude of $62,000$ ft (or about 19 km) [89].

11.3.3 Blimps

Blimps are airships that fly by the lighter-than-air principle and contain helium or hydrogen. They have a non-rigid structure and change shape with changing altitude. Blimps also have a share in the UAV market. The largest development programs in this field received government funding. One of these is the Northrop Grumman's Long Endurance Multi-Intelligence Vehicle (LEMV). It has a long endurance, but it does not operate at the same altitude as StratoMAV. The unit cost of the LEMV is 154 million U.S. dollars [90].

11.3.4 Competitors of StratoMAV

StratoMAV's current mission, to investigate the regional effects of contrails on the ground surface temperature, is a scientific remote sensing mission at high altitude. Looking at other concepts as described above, all concepts except for blimps could perform the same scientific mission. These competitors have advantages and disadvantages when compared to StratoMAV.

Satellites can perform measurements on radiation for a longer time than StratoMAV, but they are located far above commercial airspace. Their resolution will therefore be much lower than the measurements taken by StratoMAV. The unmanned aircraft are most comparable to StratoMAV: they can fly at the same altitude and will thus be able to obtain the same level of detail in their measurements. However, none of the mentioned concepts have ever flown for one year continuously.

Concluding, it can be said that StratoMAV, with its detailed stratospheric measurements, will be able to fill the gap between measurements taken by satellites and from the ground. It can also stay airborne longer than any other solar powered unmanned aircraft or superpressure balloon, which means it is very useful to perform long-term measurements. This gives StratoMAV a very good competitive position in the remote sensing market.

11.3.5 Spin-Off Markets

Next to performing a stratospheric science mission, it is possible to use StratoMAV in more areas. By equipping StratoMAV with another payload, other types of missions could be completed:

- The first area that comes to mind is using StratoMAV for military purposes. The U.S. military defence budget is being cut, calling for smaller, cheaper and less risky solutions. StratoMAV has a relatively low unit cost compared to already existing and comparable UAVs, making it an interesting option for the U.S. military defence [91]. One can think of reconnaissance and espionage.
- Another field of interest is surveillance. Possibilities within this field are spotting forest fires, detecting illegal border crossing and agricultural monitoring.
- A third possible working area for StratoMAV will be navigation. By using the on-board optical sensors, it is possible to very accurately determine position. This data can be send to a user which can then use this to improve its ground position estimation.

11.4 Sustainable Development Strategy

This section elaborates on the sustainability approach which taken into consideration while designing StratoMAV. The focus is on subsystems and transportation of StratoMAV.

11.4.1 Power Sources

Solar energy is recognised as a sustainable power source. However, solar module manufacturing and disposal can damage the environment [92]. The solar panels used on StratoMAV (see section 7) are silicon solar cells. These panels contain materials such as aluminium, silicon, circuit components and coatings, which can be separated and re-used in new solar panels or other products [93]. There are several companies that recycle silicon solar panels, which can recover 84% of the original weight, and 95%[93] of the semiconductors can be used in new panels. Solar cells have an expected lifetime of 20-40 years [94]. Since its minimum life time is five years, solar panels from the old StratoMAV will be recycled to produce new solar panels. During the life time of a solar panel, its material is damaged by photo-disintegration. This will lead to degradation of the solar panel which can be avoided by enriching it. With this strategy, less material is used, which improves the sustainability of the design.

11.4.2 Battery

In the sizing of the energy storage system a lithium ion battery has been chosen. In the case that these batteries overheat or overcharge, they can rupture and may leak lithium, which can also melt. If the molten lithium leaks out of the cell and comes into contact with water, it can start a fire. The battery's electrolyte can also catch fire [95]. All this could damage the environment and imposes hazards for humans, animals and nature.

Lithium-ion batteries can be recycled. If they are completely de-charged at the end of their life, they can be decomposed such that the metal components in their casing, like copper and steel, can be recycled. If the batteries are still charged, they can be frozen in liquid nitrogen. This ensures that the battery components cannot react with each other. Next, the metal components can be separated and recycled. In the recycling process there will always be a material loss. Since lithium is not an abundant material,

its use is not sustainable, which calls for recycling. However, battery recycling is energy-intensive, and it takes 6 to 10 times more energy to reclaim metals from recycled batteries as it does to produce the materials through other means, including mining [96].

11.4.3 Transportation

The aim is to transport the UAV in a sustainable manner. This includes ground transportation from the storage location to the take-off or launch pad and the take-off itself. The UAV is transported on ground with a truck, as described in section 11.1. This truck should operate in a sustainable manner. The power source of the vehicle must be considered, but also the recycling of the vehicle. It would be optimal if the truck could run either on electricity (ideally a sustainable energy source) or biofuel. The UAV is brought to cruise altitude with a helium-filled balloon. This is a sustainable way to do this, as no fuel is used. However, the balloon is made of a material that might not be biodegradable. Therefore, it must be retrieved after the UAV has been released.

11.4.4 Materials

The materials used to build StratoMAV must also be considered when analysing the sustainability. StratoMAV's structure is build out of balsa wood, polyethylene teraphthalate (PET), Duplont Teflon Fluoropolymer (DTF) and carbon fibre reinforced plastic (CFRP).

Balsa wood comes from fast growing trees, which can grow up to 90 m in 10 years. Therefore balsa wood is suitable for a commercial plantation. Ecuador delivers 95 % of the commercially sold balsa wood, from which 60 % is acquired from plantations, making it a sustainable material to a certain level. Balsa wood is also an organic material, which means it is biologically degradable.

CFRP can be retrieved at the end of life of StratoMAV. It can be thermally decomposed through thermal depolymerisation, which can be achieved in refineries. Re-use of carbon and monomers is then possible. CFRP can also be milled, in which it can be retrieved and recycled for other applications. However, the fibres are shortened, decreasing the strength of the recycled CFRP, which could make it useless for aerospace applications.

DTF is used as coating on the solar cell. After the DTF coating is separated from the solar cell it can be recycled. DTF is a thermoplastic, which can be remelted and reused for other applications.

PET is an often used material in bottles. Therefore, there also is a large recycling industry for PET. Since the UAV skin consists primarily of PET, the skin can be recycled with the same process PET bottles undergo.

11.5 Production Plan

Production planning is the acquisition and allocation of all resources needed to accomplice the production of the aircraft within time and budget. Most important is to ensure that the right resources like raw materials and manpower are available at the right moment. This ensures that every part is produced in time to be assembled on a sub-assembly or ultimately on the aircraft.

This analysis will give a first global overview how this should be done for StratoMAV. It should be noted that only the most important steps that should be taken are discussed in a qualitative sense, hence there will be no numbers presented on the actual time needed for every step. This analysis starts

after the moment the whole design is ready for production, that is including all production drawings. The production plan makes a distinction between elements that should be bought and elements that are produced in-house.

The most time consuming elements are the composite parts, reason for this is that these parts are made by hand. These will be build in-house to ensure high quality products. Most critical in this sense is ordering the required moulds, because this generally takes a lot of time. Moulds are needed for the d-boxes of the main wing, tail and for the propeller. Also milling of the ribs and the foam core of the propeller should be done in time to ensure laminating can start at the right moment.

While everything is being arranged to start the composite production, other important items can be ordered. Most important in this are the batteries, solar cells, flight control elements and payload. The first two, because they should be assembled into modulus that fit the aircraft as designed. The latter two, because for example the auto-pilot should be programmed and extensively tested before it can be placed in the aircraft.

The payload consists of off-the-shelf sensors and other electronic parts which only should be assembled properly. However, it is very important to thoroughly test the final payload sub-assembly to learn whether it meets all performance requirements.

After the moulds are delivered, production of the airframe can start. The spar is at this point already pre-assembled from pultruded strips and Rohacell 51. The D-boxes can be moulded now. After curing, the torsion box can be completed by glueing the spar and D-box together. Hereafter the pre-cut ribs and trailing edge strip are connected to the torsion box. Also the ailerons will be mounted in this stage. The tail is produced in parallel and exactly in the same manner as the wing. Because there are no systems in the tail, it can be covered with foil right away.

Before covering the wing with foil and solar cells, all systems should be mounted in the wing. These systems include the batteries, servos, payload, motor and gearbox. Besides placing all components, the wiring harness should also be routed. Also the booms and tail can now be aligned and connected. Now the foil and the solar cells can be applied on the wing. Finally the propeller can be mounted. Now the aircraft is completely assembled, full system tests can be conducted. After all tests are successful and/or all repairs and replacements are done in case of faulty test results, the aircraft can make its first test flight.

11.6 Post-DSE Activities

This section introduces the post-DSE planning. Figure 11.1 shows the activities to be performed for the post-DSE period. The suggested time frame is qualitatively indicated and figure 11.1 should be read from top to bottom. Figure 11.2 introduces the post-DSE planning in the form of a Gantt chart. The activities are based on the project design and development logic.

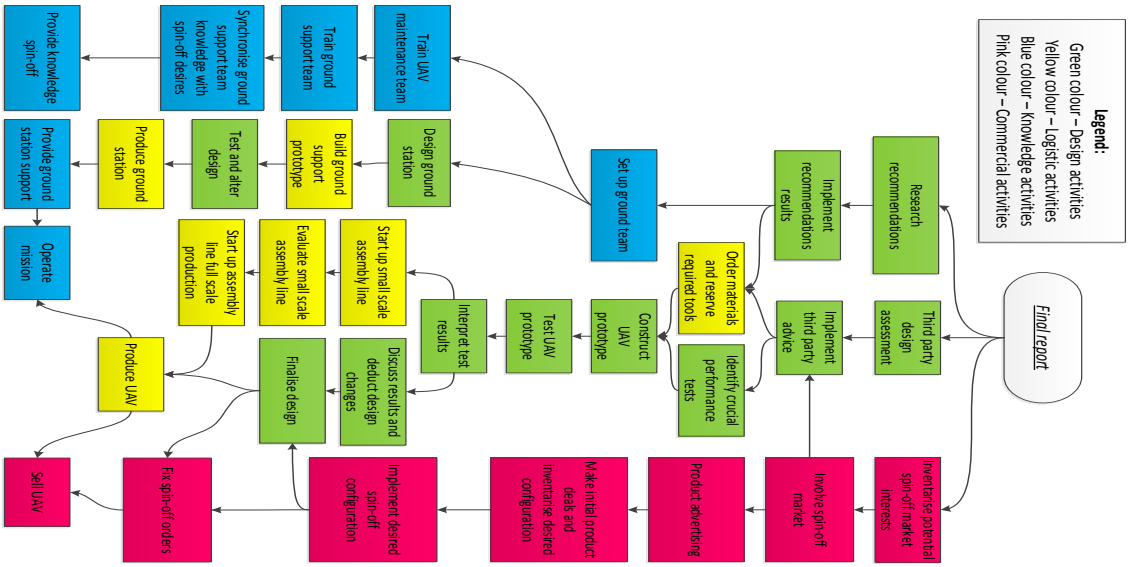

Figure 11.1: Project design and development logic

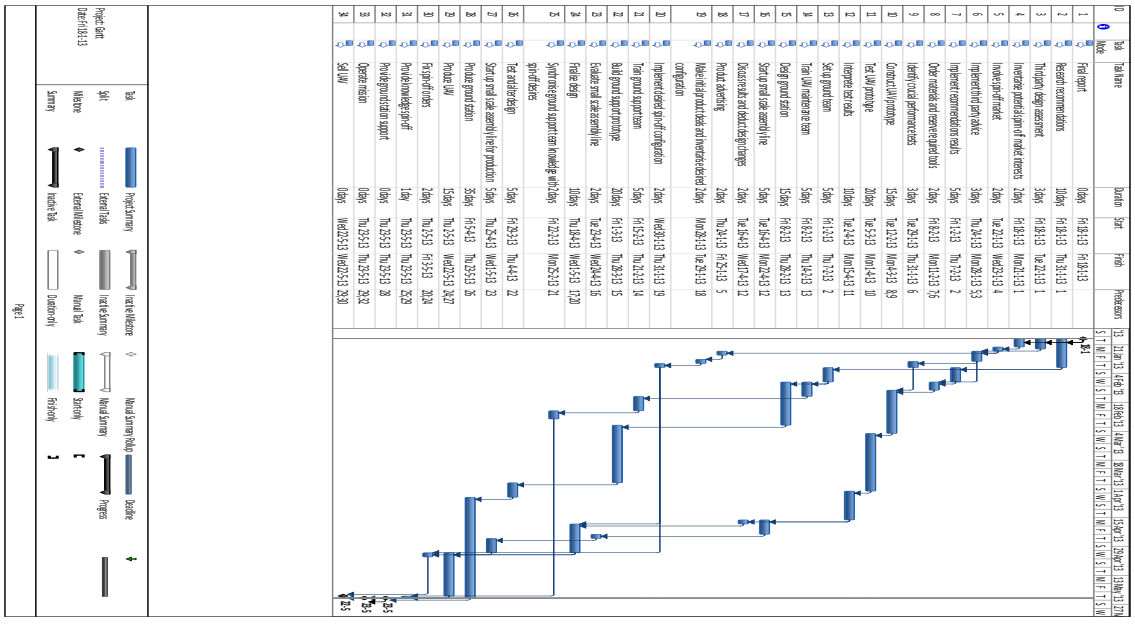

Figure 11.2: Gant chart

Chapter 12

Conclusions

The reader should now understand that a stratospheric long endurance UAV, that can sustain continuous flight for at least a year, is feasible and the conceptual design meets the requirements as described in section 10.6. The design features a low weight, relatively low cost MAV with a low power consumption (see table 10.1). In chapter 8, StratoMAV's unique capabilities, that allow it to collect measurement data, are addressed. Other aircraft and spacecraft currently do not provide this. The science mission will provide valuable knowledge and insight about the effect of the aviation sector on global warming.

Critical factors in the design were quickly identified to be the low air density at 15 km altitude, the energy storage required to fly for one year continuously and the strict weight constraint of 5 kg. Thermal control turned out to be crucial for the mission, because the low stratospheric temperatures could cause components to fail. Appropriate solutions were found for all conditions (chapter 4, chapter 7, section 9.3). Section 9.3 showed how active and passive heating allow components to be kept within an acceptable temperature range. The high aspect ratio wing with a high lift coefficient described in chapter 4, enables a low cruise speed and provides enough lift at the cruise altitude. The power system which operates on solar energy can provide the UAV with sufficient power for at least a year, with the assistance of an optimised route. Since the detailed design of every subsystem showed positive results and the integrated system meets the given requirements referred in section 10.6 and table 10.1, a succesful design for StratoMAV seems plausible.

Chapter 13

Recommendations

Aircraft Design, Stability and Control

First of all, the airfoil of StratoMAV must be analysed using a 2D model in a wind tunnel. The current characteristics of the airfoil have now been determined using XFOIL, which gives inaccurate results at low Reynolds numbers. Moreover, a CFD analysis of the entire UAV can be performed, which will reveal how the airflow behaves around the twin booms and the tail, and how the small bump, which accommodates the gear box of the motor, influences the aerodynamic performance of the wing.

Next, a prototype of the UAV has to be tested in a wind tunnel to examine its aerodynamic performance. After testing the UAV, the design will most likely have to be adjusted and a new prototype can be built. This prototype can be built to scale, and can be used to perform flight tests. This will give even more information about the behaviour of the aircraft, which can be used to fine-tune the design. A final prototype test flight can demonstrate the absolute ceiling and the turning performance of the UAV.

Also the effect of the propeller on the wing aerodynamics has not been analysed yet. It is expected that this will have a significant influence, as the propeller is large in comparison to the wing. Possible effects are that the air is accelerated behind the propeller, which would increase lift but also drag. Moreover, the flow might become more turbulent, which would decrease the performance of the wing. The airspeed at the tail might be influenced as well, which would change the performance of the tail. The effect of the propeller can be examined by either CFD analysis or wind tunnel tests.

Furthermore, the stability and control derivatives must be determined more precisely. In the current design, they were estimated using empirical relations and assumptions, based on old (but still used) methods. Moreover, they were determined using four different references, which has probably resulted in inaccuracies. A prototype could be used to determine all derivatives experimentally.

Finally, the flight dynamics analysis can be improved by using non-linear instead of linear equations of motion. However, it is not expected that this will change the eigenmotions by a lot, as the assumptions made for the linear simulation are valid for almost all aircraft. Moreover, the model could be adjusted by using equations for a V-tail with ruddervators, instead of separate horizontal and vertical tail surfaces.

Structural Design

It is recommended to research the yield load factor, in order to provide insight into the impact of high gust occurrence during the landing phase.

Preliminary FEM-analysis performed with Abaqus show that the spar deflection is larger than predicted by the design computations (see appendix D). As shown, finite element method analysis predict a 35 cm vertical deflection, which is two times higher than the computed 18 cm.

Any combination of rib spacing and rib thickness resulting in less weight and acceptable skin sag would improve the design. A second recommendation is to research the optimum rib internal truss structure in order to save more weight using cut outs.

The wing should be analysed for flutter in order to make sure this phenomenom does not occur within the flight envelope. This analysis will couple an analysis on the aerodynamics with an analysis on the eigenmodes of the wing. Several subsystem synergic benefits should be researched.

- The most significant weight saving option would be to make the solar cell array foil load carrying.
- The proposed thermal control isolation might be combined with load carrying components.
- The batteries could be applied as structural component. It is however expected that this will induce great risks. Properly integrating the batteries would however require connections, making it heavy. A better recommendation would therefore be to invest effort in the battery casing weight reduction.

For most computations, simplifying assumptions are used. It is recommended to review these assumptions and check their validity.

- Sections are assumed doubly symmetric, where shear centres are assumed to coincide with centre of gravity
- The loads are assumed to occur exactly in line with the spar
- The torsion box is assumed to solely absorb torque
- The spar is assumed to be fully clamped at the root

Propulsion System

The propeller is designed for a power of 50 W. The final design of StratoMAV only requires 36 W to propel itself. It is recommended to redo the propeller calculations for a power of 36 W although the gain would not be very large (figure 6.4). Finding an airfoil for the propeller that suits the mission of StratoMAV best is the next recommendation. For this study, an airfoil that has a lot of test data was chosen. This allowed us to compare data from the model with actual test data. The Blade Element Model can be improved by applying the Prandtl tip loss correction. Incorporating non-axial flows can give some knowledge about the influence of the propeller on the stability of the aircraft (for example the P-factor). Performing a Finite Element Analysis of the entire propeller is recommended for the structural design of the propeller.

For the gearbox it is recommended to further check the effect of wear on the aluminium gear teeth at the mission altitude.

Power

The route, as it is planned now, involves a drastic increase in the latitude. This could be reduced if the energy left would be taken into account in the optimization problem. A recommendation for a

more thorough design of the route is that the energy left should be treated as a constrain function in the optimization problem. Furthermore, an analysis on active solar panel control could be performed to investigate whether it is beneficial, in terms of battery mass, to actively control the orientation of the solar panels. The orientation of the solar panels could be controlled in such a way that the power output of the solar panels is increased. This results in a lower battery mass as the solar panels can take over earlier from the batteries. Finally, a simulation of the power system could be made in for example Simulink to validate the design. From the simulation it also becomes clear at what times and with which frequency measurements, downlinks and uplinks can be performed. A final recommendation is to decrease the ideal cruise power. As already mentioned in section 7.2, reducing the ideal cruise power can significantly reduce the mass of the batteries. However, it requires to redesign the entire UAV which is time-intensive. This could be done in further studies on StratoMAV.

Payload

It was quite a challenge to find small and light weight spectrometers that suited StratoMAV's purpose. It is suggested to develop custom designed sensors for the mission, to optimize the weight and data quality. Custom designed sensors also make integration with the rest of the UAV's design easier. Also, laboratory tests are suggested to determine whether they are able to measure contrails sufficiently with a 4 km altitude difference. The costs of the spectrometers, the performance information about the FLIR thermal camera core and the amount of bits stored per pixel in the spectrometers (which is required for the data rate calculation) are still unknown and need to be found out.

At the moment, the existing version of the contrail detection is only able to distinguish linear contrails from background sources. It is suggested that for the StratoMAV the algorithm is expanded to be able to recognise spreading contrails and to track their movements. Previous applications of the algorithm were based on satellite imagery. Real-time use on board of a UAV means that processing time will have to be optimized. A record of contrail detections in the previous frames can be used to create new functions.

Support systems

The design of the thermal control system should include more detailed information about the thermal performance of all components present in the StratoMAV. Furthermore, the cost of the thermal system must be analysed in detail to constrain the design space.

It is recommended that, when the telemetry subsystem is integrated into the UAV, the antenna is shielded from electromagnetic interference resulting from electronics on board. Similarly, the payload sensors should not receive interference from the antenna. A better antenna could be designed, by optimizing the weight of the substrate related to the required area for a certain frequency. Using a substrate with a higher dielectric would lower the gain and directivity, but decrease the required size. Another frequency could be chosen, for example 2.4 GHz if more data could be obtained about 2.4 GHz radio modems from a manufacturer, or through testing. Operating at a higher frequency decreases the antenna size and multiple antenna patches could be then be arranged on the UAV in an array to optimize the gain and receive sensitivty.

For now the autopilot is stable, but that is with the assumption of a normal inverted T-tail. With the correct stability derivatives that follow from actual testflights and windtunnel experiments the autopilot can will be better in actual flight. Tuning will then be harder as the ruddervator deflection

has significant influence on the pitch, roll and yawing moment. Also an autothrottle function has to be build so StratoMAV can accelerate or climb to a desired altitude if wanted. If it follows that the control surfaces needs upgrading the servos will have to be redesigned too. Finally the JSBSim model has to be implemented in Paparazzi to couple both the autopilot and the automatic navigation. Also all sensors have to be tested to ensure their accuracy is enough. If a GPS with better accuracy can be found and it is proven it can work properly for a year the airspeed sensor might be redundant.

Bibliography Scientific Sources

[1] H. von Storch. Climate research and policy advice: Scientific and cultural constructions of knowledge. November 2009.

[2] S.S.C. Ou and K.N. Liou. Subject specific white paper on contrail/cirrus optics and radiation. 2008.

[3] D.J. Travis, A.M. Carleton, and R.G. Lauritsen. Contrails reduce daily temperature range. *Nature*, 2002.

[4] J. Everaerts. Pegasus: Design of a stratospheric long endurance uav system for remote sensing. Technical report, Vito, Flemish Institude for Technological Research, 2004?

[5] Steiner R. Coleman, T.L. Atmospheric turbulence measurements obtained from airplane operations at altitudes between 20,000 and 75,000 feet for several areas in the northern hemisphere. Technical report, 1960.

[6] Aircraft Contrails Factsheet. Technical report, United States Environmental Protection Agency (EPA), 2000.

[7] R. Wendling P. Mannstein, H. Meyer. Operational detection of contrails from noaa-avhrr-data. *International Journal of Remote Sensing*, 20(8):p.1641–1660, 1999.

[8] F. Schroder. On the Transition of Contrails into Cirrus Clouds. *Journal of the Atmospheric Sciences*, 57:464–480, 2000.

[9] S. Solomon, D. Qin, M. Manning, Z. Chen, M. Marquis, K.B. Averyt, M. Tignor, and H.L. Miller. Contribution of Working Group I to the Fourth Assessment Report of the Intergovernmental Panel on Climate Change. Technical report, Intergovernmental Panel on Climate Change, 2007.

[10] A. Noth. *Design of Solar Powered Airplanes for Continuous Flight*. PhD thesis, ETH Zürich, 2008.

[11] J.D. Anderson and J. Anderson. *Fundamentals of Aerodynamics*. McGraw-Hill Education - Europe, 2006.

[12] G. La Rocca. AE3-021 Aircraft Design Lecture Notes. TU Delft, Faculty of Aerospace Engineering, 2010-2011.

[13] D.P. Raymer, editor. *Aircraft Design: A conceptual Approach*. American Institute of Aeronautics and Astronautics, Inc., 3rd ed. edition, 1999.

[14] M.A. Rong, Z.H.O.N.G. Bowen, and Liu PeiQing. Optimization design study of low-reynolds-number high-lift airfoils for the high-efficiency propeller of low-dynamic vehicles in stratosphere. 2009.

[15] M.S. Selig and J. Guglielmo. High-lift low reynolds number airfoil design. 1997.

[16] M. Rong and P. Liu. Numerical simulation of low-reynolds-number and high-lift airfoil s1223. 2009.

[17] B. Dunbar. Helios Prototype: The forerunner of 21st century solar-powered atmospheric satellites. http://www.nasa.gov/centers/dryden/news/FactSheets/FS-068-DFRC.html. Retrieved on 15-01-2013.

[18] M.S. Selig. Low reynolds number airfoil design. 2003.

[19] J.D. Anderson, Jr. *Introduction to Flight*. McGraw-Hill Education - Europe, sixth ed. edition, 2008.

[20] Flight dynamics lecture notes. TU Delft. Faculty of Aerospace Engineering, March 2011.

[21] DSE Group 11. Stratomav. Technical report, TU Delft, Faculty of Aerospace Engineering, Januari 2013.

[22] J. Roskam, editor. *Airplane Design, Part V: Component Weight Estimation*. DARcorporation, third printing edition, 2003.

[23] S. Neumark. Analysis of Short-period Longitudinal Oscillations of an Aircraft – Interpretation of Flight Tests. Technical report, Aeronautical Research Council, 1956.

[24] Michael F. Ashby, editor. *Materials Selection in Mechanical Design*. Butterworth-Heinemann, 3th ed. edition, 2004.

[25] Duffie and W.A.Beckman. Solar engineering of thermal processes. Technical report, 1991.

[26] *Calculus, Early transcendentals, 6th edition*, chapter 14.4. Bob Pirtle, 2008.

[27] *Calculus, Early transcendentals, 6th edition*, chapter 14.3. Bob Pirtle, 2008.

[28] A. Noth.

[29] Breed, G. The Fundamentals of Patch Antenna Design and Performance. Technical report, Summit Technical Media, 2009.

[30] T. R. Harris. The design process of a rectangular microstrip antenna. Technical report, North Carolina State University.

[31] Maral, G. and Bousquet, M., editor. *Satellite Communications Systems*. John Wiley and Sons, LTD, 4th ed. edition, 2002.

[32] J. R. Wertz and W. J. Larson, editors. *Space Mission Analysis and Design*. Microcosm Press, 3rd ed. edition, 1999.

[33] Example of technical characteristics for unmanned aircraft control and non-payload communications links. Technical report, International Telecommunication Union (ITU), 11 2011.

[34] R. L. Freeman, editor. *Fundamentals of Telecommunications*. John Wiley and Sons, Inc., 2nd ed. edition, 2005.

[35] NPX. Lpc2114/2124 single-chip 16/32-bit microcontrollers; 128/256 kb isp/iap flash with 10-bit adc.

[36] Analog devices. Digital accelrometer adxl345-ep.

[37] Ublox. gyroa, author = "invensense", title = ITG-3200 Product Specification Revision 1.7,.

[38] *Space Mission Analysis and Design, Third Edition*, chapter 11.5 page 428. Microcosm Press and Kluwer Academic Publishers, 1999.

[39] A. Ph.D. Klenke. Development of a novel, two-processor architecture for a small uav autopilot system. Technical report, Virginia Commonwealth University, July 2006.

[40] J. Roskam, editor. *Airplane Design, Part VI: Preliminary Calculation of Aerodynamic, Thrust and Power Characteristics*. DARcorporation, third printing edition, 2000.

[41] E.P. Hartman and D. Biermann. The aerodynamic characteristics of full-scale propellers having 2, 3, and 4 blades of clark y and r.a.f. 6 airfoil sections. Technical report, National Advisory Committee for Aeronautics (NACA), 1938.

[42] W.F. Hosford, editor. *Mechanical Behavior of Materials*. Cambridge University Press, 2005.

[43] T.H.G. Megson, editor. *Aircraft Structures for engineering students*. Butterworth-Heinemann, 4th ed. edition, 2007.

Website References

[44] ABOUT 9/11. http://web.archive.org/web/20110722151526/http://www.biography.com/profiles-of-9-11/about911.jsp. Retrieved on 17-01-2013.

[45] M. Velasquez-Manoff. Airplane Contrails and their Effect on Temperatures. http://www.csmonitor.com/Environment/Bright-Green/2010/0201/Airplane-contrails-and-their-effect-on-temperatures, February 2010. Retrieved on 16-11-2012.

[46] Frierson D.M.W. Elliott, W. P. Atmospheric structure. http://courses.washington.edu/pcc587/readings/atmosphericstructure.pdf, 2009. Retrieved on 27-11-2012.

[47] Cirrus Clouds: Thin and Wispy. http://ww2010.atmos.uiuc.edu/%28Gh%29/guides/mtr/cld/cldtyp/hgh/crs.rxml. Retrieved on 19-11-2012.

[48] Efficiency of solar panels. http://www.energybandgap.com/power-generation/efficiency-of-solar-panels/, February 2011. Retrieved on 10-12-2012.

[49] B. Dunbar. Helios Prototype: The forerunner of 21st century solar-powered atmospheric satellites. http://www.nasa.gov/centers/dryden/news/FactSheets/FS-068-DFRC.html. Retrieved on 15-01-2013.

[50] B. Dunbar. NASA Dryden Fact Sheet - Pathfinder Solar-Powered Aircraft. http://www.nasa.gov/centers/dryden/news/FactSheets/FS-034-DFRC.html. Retrieved on 15-01-2013.

[51] R&G Faserverbundwerkstoffe GmbH. http://www.r-g.de/de/, January 2013. Retrieved on 17-01-2013.

[52] Quartel Modelbouw BV. http://www.quartel.nl/webshop, January 2013. Retrieved on 17-01-2013.

[53] Technical data sheet Oracover. http://www.oracover.de, January 2013. Retrieved on 11-01-2013.

[54] Hansen, B. http://www.coilgun.info/theory/numberofturns.htm. Retrieved on 28-01-2013.

[55] KISSsoft AG. KISSsoft. http://www.kisssoft.ch/english/products/kisssoft.php. Retrieved on 15-01-2013.

[56] Stanford University. The world record energy density of 400 Wh/kg is achieved by Envia. http://aero.stanford.edu/stdatm.html. Retrieved on 08-01-2013.

[57] E. Wesoff. Intersolar: Solexel Unstealths With Thin Silicon Solar. http://www.marketresearchmedia.com/?p=509, May 2012. Retrieved on 08-01-2013.

[58] E. Wesoff. Stion is having a CIGS solar sale. http://www.firstsolar.com/Innovation/Advanced-Thin-Film-Modules, May 2012. Retrieved on 08-01-2013.

[59] Industry benchmark thin film modules. http://www.firstsolar.com/Innovation/Advanced-Thin-Film-Modules. Retrieved on 08-1-2013.

[60] http://www.azurspace.com/images/pdfs/HNR_0002162-00-02.pdf, December 2006. Retrieved on 17-01-2013.

[61] Du Pont. Lightweight, Long Lasting, Flexible Films Offer Greater Power Output. http://www2.dupont.com/Teflon_Industrial/en_US/assets/downloads/k15778.pdfs. Retrieved on 15-01-2013.

[62] Tony Sample. Failure modes and degradation rates from field-aged crystalline silicon modules . http://www1.eere.energy.gov/solar/pdfs/pvmrw2011_28_csi_sample.pdf, February 2011. Retrieved on 25-01-2013.

[63] Wire gauge and current limits including skin depth and strength. http://www.powerstream.com/Wire_Size.htm. Retrieved on 21-01-2013.

[64] Aircraft wire pvc nylon unshielded awg22. http://ghcable.en.alibaba.com/product/427709664-213821707/Aircraft_Wire_PVC_Nylon_Unshielded_AWG22_Nylon_Insulation.html. Retrieved on 21-01-2013.

[65] solarVSterrestial.jpg. http://clasfaculty.ucdenver.edu/callen/1202/Climate/EarthTempClim/solarVSterrestrial.jpg. Retrieved on 6-01-2013.

[66] FLIR Systems. Quark LWIR Camera Cores - Specifications | FLIR Systems. http://www.flir.com/cvs/cores/view/?id=51266&collectionid=549&col=51275. Retrieved on 10-12-2012.

[67] T. Anderson, N Erdogan. Spectral Modeling in Fluorescence Microscopy. http://www.semrock.com/Data/Sites/1/semrockpdfs/whitepaper_spectralmodelinginfluorescencemicroscopy.pdf. Retrieved on 05-01-2013.

[68] Texas Instruments. Hercules^TM ARM©Safety MCUs - TMS570LS ARM Cortex-R4F Series - TMS570LS1224 - TI.com. http://www.ti.com/product/tms570ls1224. Retrieved on 15-01-2013.

[69] FLIR. Quark Product Specification. http://www.flir.com/uploadedFiles/CVS_Americas/Cores_and_Components_NEW/Resources/QuarkProductSpec_Rev100.pdf, November 2011. Retrieved on 10-12-2013.

[70] FLIR. Quark Electrical Interface Description. http://www.flir.com/uploadedFiles/CVS_Americas/Cores_and_Components_NEW/Products/Uncooled_Cores/Quark/FLIR-Quark-Electrical-IDD.pdf, July 2012. Retrieved on 10-12-2013.

[71] Antenna-Theory.com - Small Loop Antenna. http://www.antenna-theory.com/antennas/smallLoop.php. Retrieved on 07-01-2013.

[72] Digi. Xbee-pro 900hp - digi international. http://www.digi.com/products/wireless-wired-embedded-solutions/zigbee-rf-modules/point-multipoint-rfmodules/xbee-pro-900hp#specs. Retrieved on 08-01-2013.

[73] T. Cutler. Unlicensed Wireless Data Communications, Part II: Specifying RF Parameters. http://www.ce-mag.com/archive/02/Spring/cutler2.html. Retrieved on 18-01-2013.

[74] http://paparazzi.enac.fr/wiki/Hardware. Retrieved on 13-01-2013.

[75] PPZUAVG. Umarim lite V2. https://store.ppzuav.com/osc/product_info.php?products_id=142&osCsid=dkctppvdt2brelj617qijv3s24. Retrieved on 07-01-2013.

[76] Eagle Tree. Dual Mode Microsensors. http://www.eagletreesystems.com/Standalone/standalone.htm. Retrieved on 07-01-2013.

[77] Craig Tenney. Servo Torque Calculator. http://www.geistware.com/rcmodeling/calculators.htm. Retrieved on 9-01-2013.

[78] Dymond. Dymond D47. http://www.modellhobby.de/Electronic/Servos/DYMOND/DYMOND-D-47-Servo.htm?shop=k_staufenb_e&SessionId=&a=article&ProdNr=03111701&t=9&c=75&p=75. Retrieved on 9-01-2013.

[79] Hobbyking. Turnigy Teflon Coated Wire 36AWG (1mtr) Black. http://www.hobbyking.com/hobbyking/store/__11850__Turnigy_Teflon_Coated_Wire_36AWG_1mtr_Black.html. Retrieved on 9-01-2013.

[80] Multi-layer insulation for satellites and other spacecraft. http://www.rossie.com/mli.htm. Retrieved on 21-01-2013.

[81] Kaymont Consolidated Industries. Balloons used in Near Space Photography. http://kaymontballoons.com/Near_Space_Photography.html, 2013. Retrieved on 16-01-2013.

[82] Mulroy, J. [Space] Balloon Prices. https://www.noisebridge.net/pipermail/space/2011-October/001002.html, October 2011. Retrieved on 16-01-2013.

[83] Johnson, N. . Weather balloons: What goes up must come down. http://www.wral.com/weather/blogpost/11310455/, 2012. Retrieved on 16-01-2013.

[84] Rocketman. High Altitude Balloon Payload Recovery Parachutes. http://www.the-rocketman.com/recovery.html. Retrieved on 16-01-2013.

[85] A. Keith. Earth Observation: Emerging Markets, Partnerships Set to Fuel Global Growth. http://eijournal.com/2011/earth-observation-emerging-markets-partnerships-set-to-fuel-global-growth-2, February 2011. Retrieved on 20-11-2012.

[86] H. Riebeek. Catalog of Earth Satellite Orbits. http://earthobservatory.nasa.gov/Features/OrbitsCatalog/, September 2009. Retrieved on 20-11-2012.

[87] TEAL Group Corporation. Predicts Worldwide UAV Market. http://tealgroup.com/index.php/about-teal/teal-group-in-the-media/3/79-teal-group-predicts-worldwide-uav-market-will-total-89-billion-in-its-2012-uav-market-prof April 2012. Retrieved on 20-11-2012.

[88] B. Dunbar. Helios Prototype: The forerunner of 21st century solar-powered atmospheric satellites. http://www.nasa.gov/centers/dryden/news/FactSheets/FS-068-DFRC.html. Retrieved on 15-01-2013.

[89] It's official: Zephyr Takes UAV Endurance Record. http://www.flightglobal.com/news/articles/its-official-zephyr-takes-uav-endurance-record-351216, December 2010. Retrieved on 21-11-2012.

[90] Northrop Grumman. Long Endurance Multi-Intelligence Vehicle. http://www.as.northropgrumman.com/products/lemv/, May 2012. Retrieved on 20-11-2012.

[91] M. Uncinus. U.S. Military Unmanned Aerial Vehicles UAV Market Forecast. http://www.marketresearchmedia.com/?p=509, October 2012. Retrieved on 22-11-2012.

[92] Towards a Just and Sustainable Solar Industry. http://svtc.org/our-work/solar/. Retrieved on 10-12-2012.

[93] Larsen, K. End-of-life PV: then what? - Recycling solar PV Panels. http://www.renewableenergyfocus.com/view/3005/end-of-life-pv-then-what-recycling-solar-pv-panels/, August 2009. Retrieved on 10-12-2012.

[94] Goodall, K. How long do solar panels last? http://www.renewableenergyfocus.com/view/3005/end-of-life-pv-then-what-recycling-solar-pv-panels/, August 2009. Retrieved on 10-12-2012.

[95] Revisiting Lithium-Sulfur Batteries. Retrieved on 10-12-2012.

[96] http://batteryuniversity.com/learn/article/recycling_batteries. Retrieved on 17-01-2013.

Appendix A

Functional Flow Diagram

This appendix displays the Functional Flow Diagram for StratoMAV, as described in subsection 3.

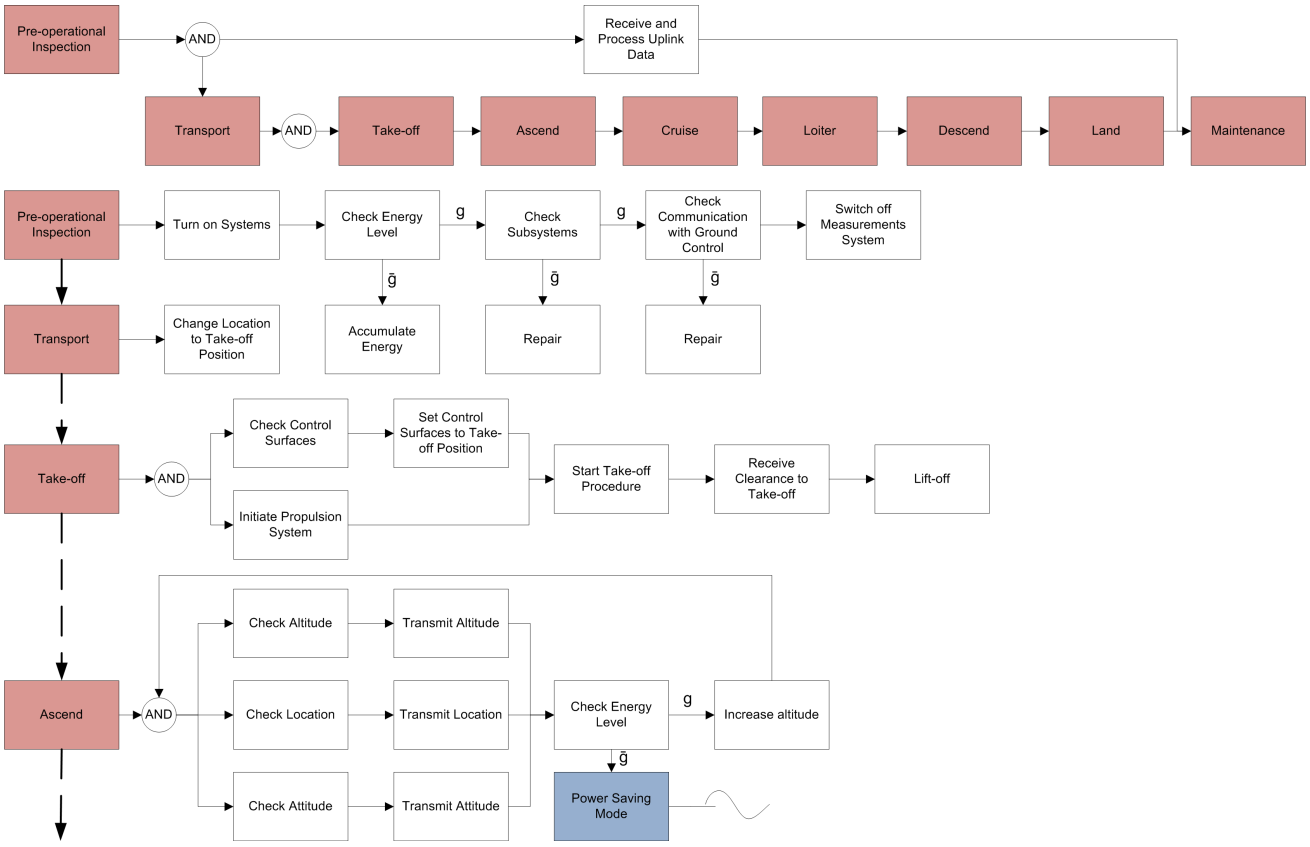

Figure A.1: Functional Flow Diagram part 1

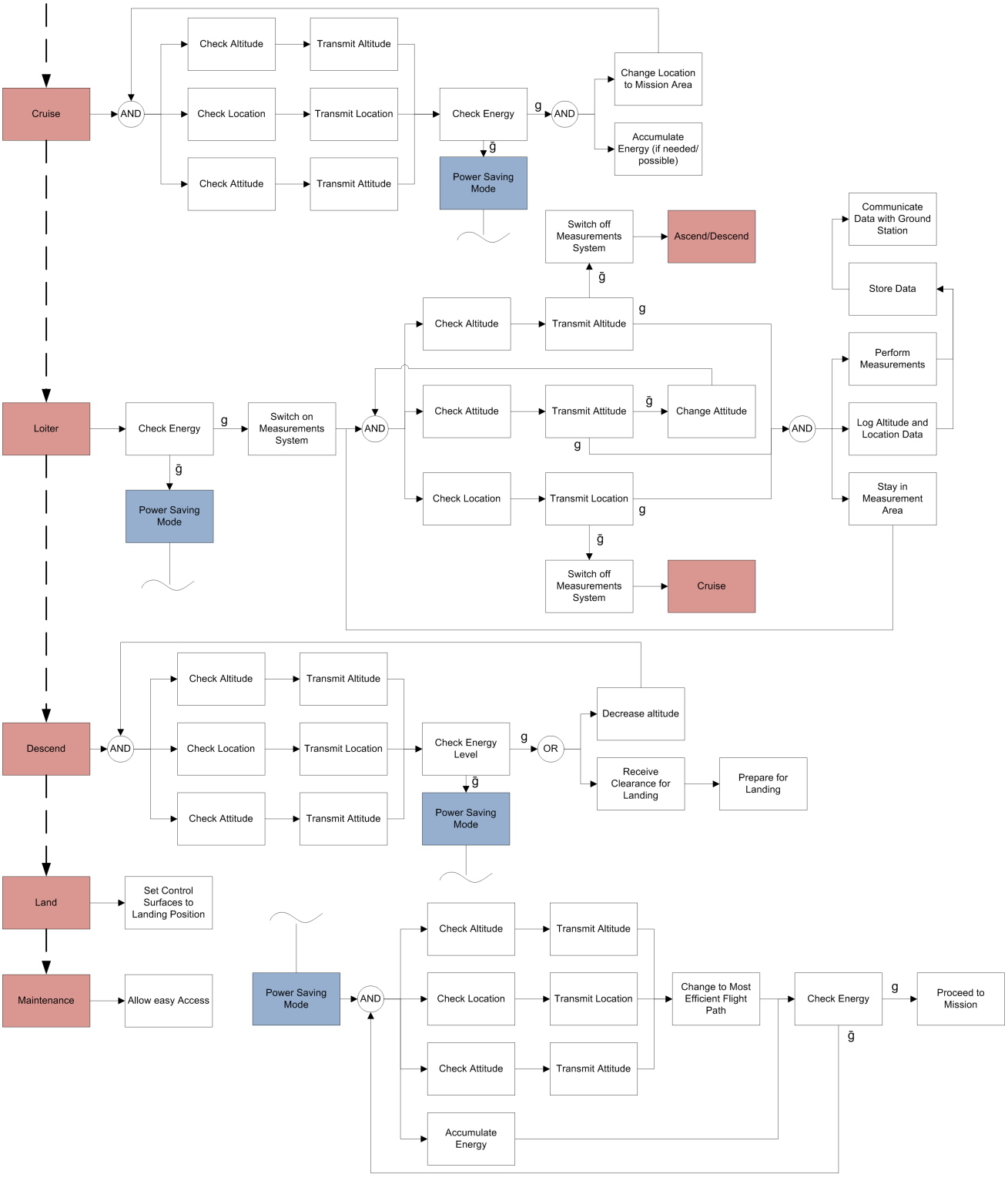

Figure A.2: Functional Flow Diagram part 2

Appendix B

Functional Breakdown Structure

This appendix displays the Functional Breakdown Structure, as described in subsection 3.

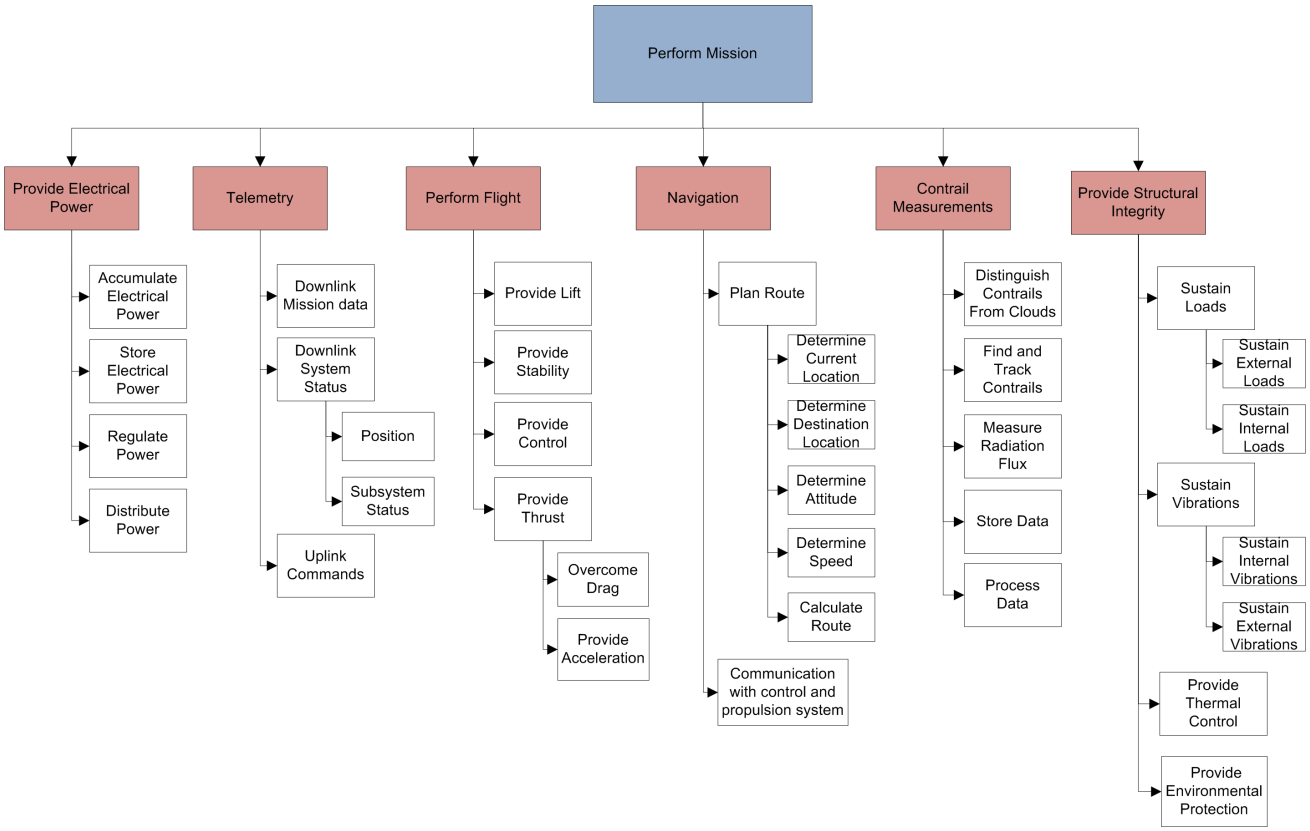

Figure B.1: Functional Breakdown Structure

Appendix C

Calculation of Stability and Control Derivatives

C.1 Stability Derivatives

This section shows how the stability derivatives of the aircraft were found.

C.1.1 Derivatives for Steady Flight Condition

First, the stability derivatives for steady flight condition are calculated. C_{X_0} and C_{Z_0}can be determined using the flight dynamics reader ([20], p. 82), and depend on the weight, the pitch angle, the density, the velocity and the wing surface.

C.1.2 Longitudinal Stability Derivatives

Next, the stability derivatives in longitudinal direction are determined.

Derivatives with Respect to Airspeed
The calculations start with the stability derivatives with respect to the airspeed in the direction of the X_s-axis and thus in longitudinal direction: C_{X_u}, C_{Z_u} and C_{m_u}. These values have to be calculated using a wind tunnel and a actual model of the StratoMAV (Flight Dynamics Reader [20], p. 152). Therefore, these values are taken from the model made in XFLR5.

Derivatives with Respect to Angle of Attack
Next, the derivatives with respect to α are calculated. These are obtained by varying the speed along the Z_s axis, as shown in figure C.1 [20]. The derivatives in question are C_{X_α}, C_{Z_α}, C_{m_α} and $C_{m_{\dot{\alpha}}}$. The value for C_{X_α} can be estimated using the lift coefficient, lift gradient, aspect ratio and Oswald factor ([20], p. 160). It is chosen to determine this derivative only for the trim angle of attack, since this is the α at which the aircraft will fly for most of the mission.

C_{Z_α} is estimated using the wing normal force slope, stabiliser normal force slope, downwash gradient, horizontal tail efficiency, wing surface area and the horizontal tail surface area ([20], p. 161).

Hereafter, the value for C_{m_α} can be estimated. It depends on the wing normal force slope, the stabilizer normal force slope, downwash gradient, horizontal tail efficiency, horizontal tail area, horizontal tail position, wing area and the mean aerodynamic chord. The position of the centre of gravity of the wing

with respect to the centre of gravity of the aircraft also influences C_{m_α} ([20], p. 161). However, it is assumed that they coincide.

$C_{m_{\dot{\alpha}}}$ can be calculated using the Flight Dynamics Reader ([20], p. 176). It depends on the downwash gradient, the horizontal tail surface, the position of the aerodynamic centre of the horizontal tail, the mean aerodynamic chord and the wing surface.

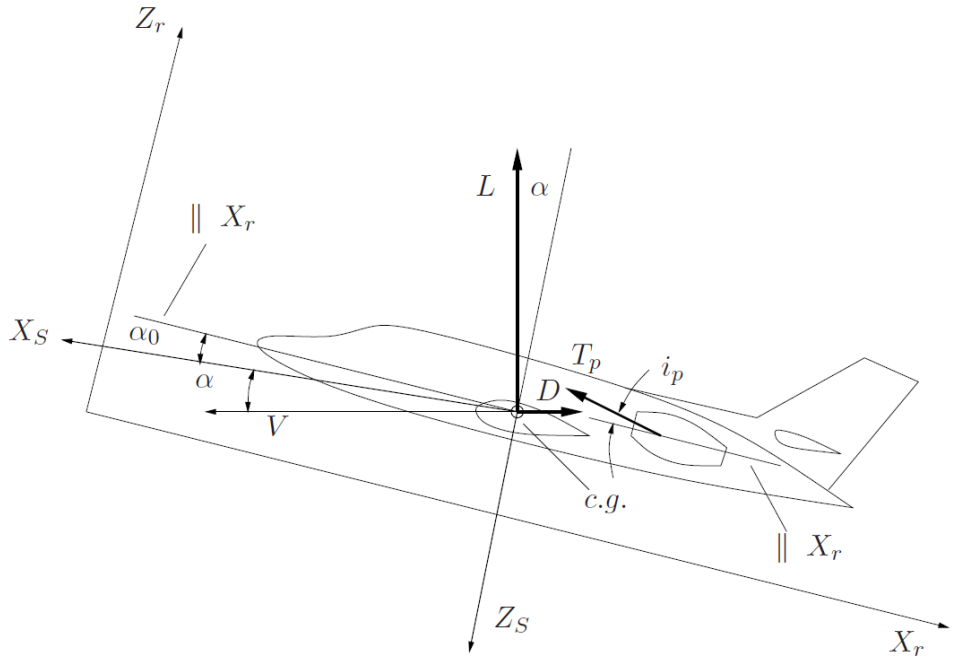

Figure C.1: The attitude of the stability reference frame relative to the X_r - and Z_r-axis, after a disturbance from the equilibrium flight condition

Derivatives with Respect to Pitch Rate
The derivatives with respect to pitch rate are C_{X_q}, C_{Z_q} and C_{m_q}. The change in X is assumed to be zero, such that $C_{X_q} = 0$. Hence, this component can be neglected. C_{Z_q} and C_{m_q} are dependent on the same variables as C_{Z_α} and C_{m_α} respectively ([20] ,p. 172). Only the wing normal force slope and the centre of gravity components do not have a contribution in this calculation.

Derivatives with Respect to Acceleration along the Top Axis
These derivatives are given by $C_{X_{\dot{\alpha}}}$ and $C_{Z_{\dot{\alpha}}}$. They depend on the same variables as C_{Z_q} and C_{m_q}([20], p. 172).

C.1.3 Lateral Stability Derivatives

Now the lateral stability derivatives are determined. The angles used are shown in figure C.2 [20].

Derivatives with Respect to Sideslip Angle
The three derivatives with respect to β are C_{Y_β}, C_{l_β}, C_{n_β}, $C_{Y_{\dot{\beta}}}$ and $C_{n_{\dot{\beta}}}$. C_{Y_β} depends on contributions of the wing, the fuselage and the vertical tail (Roskam [40], p. 383). Since StratoMAV does not have a fuselage, this term is neglected. The contribution of the wing is small, and only dependent of the dihedral angle. The contribution of the vertical tail is determined by an empirical factor, the vertical tail lift gradient, sidewash factor, vertical tail efficiency, vertical tail surface area and the wing area. For the empirical factor, it is assumed that $B_v/2r_1$ is infinite, which means that the factor becomes 1.

The vertical tail lift gradient is determined using Roskam ([40], p. 249). It is also assumed that the inverted V-tail of the StratoMAV, can be approximated by a single vertical tail, since the $b'v$ value can not be determined for a V-tail.

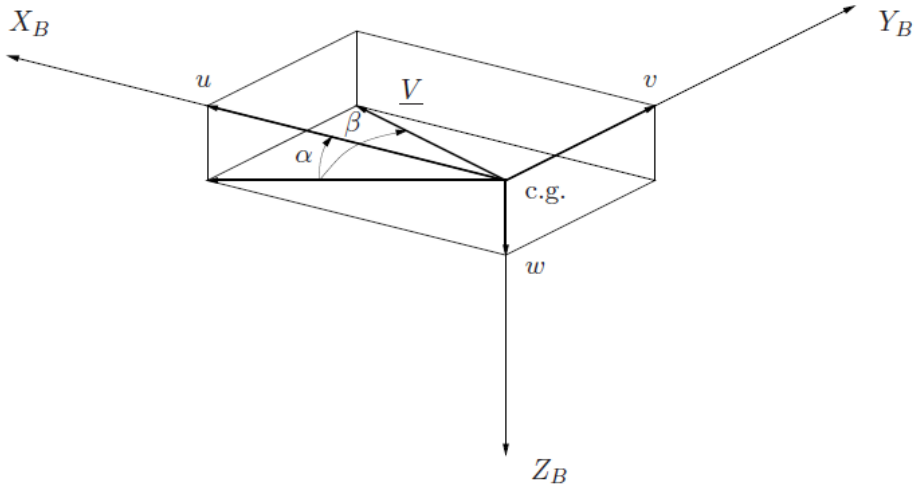

Figure C.2: Definition of the angle of attack α and sideslip angle β

C_{l_β} is influenced by the wing and the vertical tail. The contribution of the vertical tail is usually not large [20] and thus neglected. The effect of the wing depends on the sweep, the aspect ratio, the lift coefficient and the dihedral angle. This is based on Raymer ([13], p.512).

The final stability derivative with respect to the sideslip is C_{n_β}. The wing, the fuselage and the vertical tail contribute to this derivative. The wing contribution can be neglected, due to the fact that it is only important at high angle of attack ([40], p.398). The fuselage contribution is neglected. Hence, only the vertical tail contributes to C_{n_β}. It depends on $C_{Y_{\beta_v}}$, which is determined previously, the position of the aerodynamic centre of the vertical tail, the wing span and the angle of attack. This is based on Roskam ([40], p.398).

$C_{Y_{\dot\beta}}$ and $C_{n_{\dot\beta}}$ can be neglected and thus are assumed to be zero (Flight Dynamics Reader [20], p. 130 and p. 210).

Derivatives with Respect to Roll Rate

C_{Y_p}, C_{l_p} and C_{n_p} are the derivatives in question. C_{Y_p} is determined using Roskam)[40], p. 417). This factor is mainly influenced by the vertical tail, but also by some parameters of the main wing, like the sweep angle.

The roll damping derivative (C_{l_p}) is determined using the Flight Dynamics Reader ([20], p. 215), where it can be found that this derivative depends on the wing sweep, the aspect ratio and the taper ratio.

The final roll rate derivative (C_{n_p}) is determined using Roskam ([40], p. 421). The wing and the vertical tail have a contribution to this derivative. The wing contribution depends on empirical relations and the flap deflection. Since the StratoMAV does not have flaps, this part of the equation is neglected. Also the contribution of the wing twist can be neglected, due to the fact that the wing twist is determined to be zero. For the vertical tail contribution, the variables are the location of the aerodynamic centre of the vertical tail, the wing span, the angle of attack and the sideslip-due-to-sideforce of the vertical tail.

Derivatives with Respect to Yaw Rate

Hereafter, the derivatives with respect to the yaw rate are determined. These derivatives are C_{Y_r},

C_{l_r} and C_{n_r}. The side-force-due-to-yaw-rate derivative (C_{Y_r}) is mostly influenced by the vertical tail (Roskam [40], p. 428) and is determined by the location of the aerodynamic centre of the vertical tail, the wing span, the angle of attack and the sideforce-due-to-sideslip of the vertical tail.

The wing and the vertical tail have a contribution to the C_{l_r} derivative. The wing contribution is determined by empirical data, the dihedral angle and the aileron deflection. The vertical tail contribution is depended on the location of the aerodynamic centre of the vertical tail, the angle of attack, the wing span and the sideforce-due-to-sideslip of the vertical tail. This is the method as described in Roskam ([40], p. 428).

The C_{n_r} derivative is also influenced by the wing and the vertical tail. The wing contribution is found from empirical data from Roskam ([40], p. 432) and from the zero lift drag coefficient which has been determined in chapter 4. The vertical tail contribution is again determined from the location of the aerodynamic centre of the vertical tail, the angle of attack, the wing span and the sideforce-due-to-sideslip derivative of the vertical tail, as stated in Roskam ([40], p. 432).

All the important input variables are shown in table C.1. The stability derivatives are shown in table 4.5.

C.2 Control Derivatives

The control derivatives are divided into 3 groups, namely with respect to the elevator deflection, the aileron deflection and the rudder deflection.

C.2.1 Derivatives with Respect to Elevator Deflection

The derivatives with respect to δ_e are $C_{X_{\delta_e}}$, $C_{Z_{\delta_e}}$ and $C_{m_{\delta_e}}$. The control derivative $C_{X_{\delta_e}}$ can be neglected. This is due to the fact that the variation in aircraft drag with the elevator angle is very small.

$C_{Z_{\delta_e}}$ is determined using the method described in ([40], p. 438), which is based on the lift-due-to-stabilizer-incidence derivative and the flap effectiveness. However, this method uses $C_{L_{\delta_e}}$, which is defined in another axis system than used for the StratoMAV simulation. According to Roskam ([40], p. 372, eq. 10.1) $C_{Z_{\delta_e}} = -C_{L_{\delta_e}}$.

The control derivative $C_{m_{\delta_e}}$ is determined using Roskam ([40], p. 438). This derivative is also dependent on the flap effectiveness, but now uses the pitching-moment-due-to-stabilizer-incidence derivative.

C.2.2 Derivatives with Respect to Aileron Deflection

The derivatives with respect to δ_a are $C_{Y_{\delta_a}}$, $C_{l_{\delta_a}}$ and $C_{n_{\delta_a}}$. For most conventional aileron arrangements, such as the one for the StratoMAV, the side-force-due-to-aileron-deflection can be neglected (Roskam [40], p. 442). Hence, $C_{Y_{\delta_a}} = 0$.

$C_{l_{\delta_a}}$ can be determined using the size of the ailerons and empirical relations (Raymer [13], p. 512).

$C_{n_{\delta_a}}$ is determined using Raymer ([13], p. 512), and is based on the previous derivative and the lift coefficient.

C.2.3 Derivatives with Respect to Rudder Deflection

Finally, the control derivatives of the rudder are determined ($C_{Y_{\delta_r}}$, $C_{l_{\delta_r}}$ and $C_{n_{\delta_r}}$). $C_{Y_{\delta_r}}$ depends on empirical relations, the wing surface and the vertical tail surface. It is again assumed that the V-tail can be approximated by a normal single vertical tail (Roskam [40], p.461).

$C_{l_{\delta_r}}$ and $C_{n_{\delta_r}}$ are based on the location of the aerodynamic centre of the vertical tail, the angle of attack, the wing span and the side-force-due-to-rudder derivative.

All the important input parameters are shown in table C.2. The control derivatives are shown in table 4.6.

Table C.1: Input values for the stability derivatives

Parameter	Value	Unit
C_L	0.6065	[-]
C_{L_α}	5.96	[1/rad]
A	20	[-]
e	0.8	[-]
$C_{N_{w\alpha}}$	5.96	[-]
$C_{N_{h\alpha}}$	5.2382	[-]
$\frac{d\epsilon}{d\alpha}$	0.1818	[-]
$\frac{V_h}{V}^2$	0.9	[-]
S_h	0.2366	$[m^2]$
l_h	1.5	[m]
S	2.3655	$[m^2]$
$\bar{c}$	0.357	[m]
Γ	0.0542	[rad]
k_v	1	[-]
$C_{L_{\alpha_v}}$	0.1063	[1/rad]
S_v	0.1419	$[m^2]$
$C_{l_{\beta_w}}$	-0.0572	[1/rad]
λ	0.5	[-]
$C_{Y_{\beta_v}}$	-0.005	[1/rad]
l_v	1.5	[m]
z_v	0.3841	[m]
α	-0.054	[rad]
b	6.878	[m]
z	0	[m]
Λ	0	[rad]

Table C.2: Input values of the control derivatives

Parameter	Value	Unit
$C_{L_{i_h}}$	0.4455	[-]
$C_{L_{\alpha_v}}$	0.0830	[1/rad]
k'	0.58	[-]
K_b	0.92	[-]
z_v	0.3841	[m]
l_v	1.5	[m]
α	-0.054	[rad]
b	6.8782	[m]

Appendix D

Abaqus Wing Model

To get a better insight in the actual stresses and strains in the wing, an Abaqus model was created of the main structural elements of the wing, namely the spar and the torsion box. Abaqus CAE is a software package which can read Catia files and use them as input in a Finite Element Analysis (FEA). The reason to use this approach is that the analytical method using basic mechanics of materials, as used in the structures chapter (chapter 5) does not take into account many secondary effects which influence the structure in reality. One can think of the coupling between the spar and the torsion box or the deformation of the web due to shear stresses. The ribs are not taken into account in this model because they are less important for the complete performance of the wing since they only carry very local stresses. Figure D.1 shows the model and the applied loading.

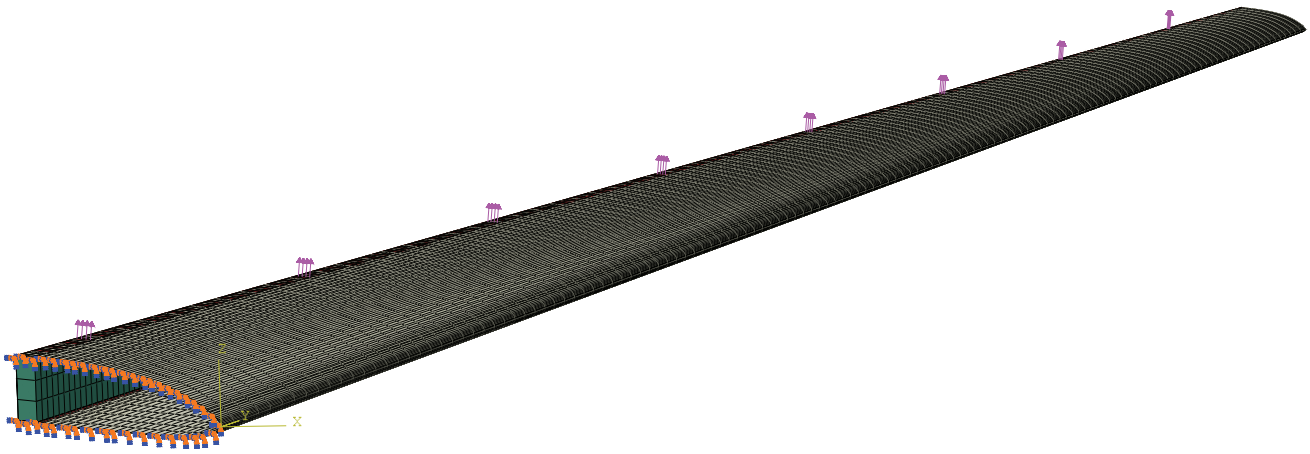

Figure D.1: Abaqus model

The flange and web of the spar are both modelled as solid elements. The torsion box consists of shell elements on which the composite layup is defined. Only half of the wing is modelled, this half is clamped in the centre in order to simulate the symmetry of the wing. The wing loading is simulated by a linear decaying line load at the rear edge of the torsion box. This line load roughly resembles an elliptical wing loading at a load factor of 2.

Figure D.2 shows a rear view of the spar in its deformed shape. The colors represent the local deflection in mm. The maximum tip deflection is 342 mm. This is less then 500 mm thus this requirement is met.

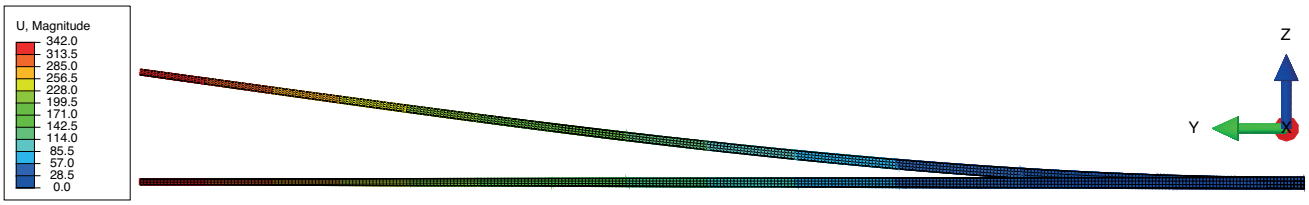

Figure D.2: Deflection of the spar

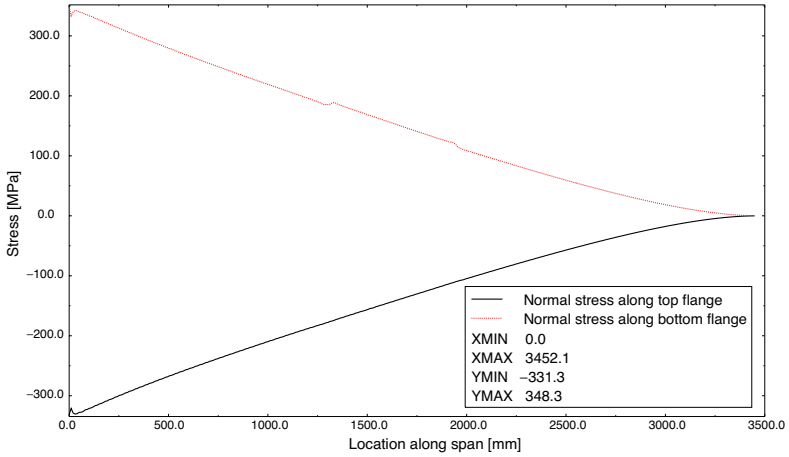

Figure D.3: Normal stress in top and bottom flange

Figure D.3 shows the normal stress in both the bottom and top flange. Both the maximum compressive stress (in the top flange) and the maximum tensile stress (in the bottom flange) are around 340 MPa. This is well under the allowable stress of $1,500$ MPa (which is the strength in compression, in tension the material is even stronger). Therefore, the design is assumed to be strong enough.

The difference with the analytical model will be discussed now. The maximum stress, that can be found in chapter 5, is 220 MPa, and the maximum deflection is 120 mm. The bending stiffness that the torsion box adds to the wing is assumed to be very small because its fibres are oriented at $\pm$ 45^{circ}. What probably does make a difference is the fact that the web of the spar deforms due to shear strain which is not taken into account in the analytical model. It makes sense to assume that this is the main reason for the much bigger deflection in the FEA model. It can thus be concluded that including the shear deflection of the web, reduces the overall stiffness of the wing. Because of the higher strains in the FEA model, the resulting stresses are also higher, this explain the difference in stress with the analytical model.

In all, it can be noted that setting up the model in Abaqus gave a lot of valuable information. Furthermore, it gave more confidence in the structural design of the wing.

Appendix E

Turbulator Placement

Because of the low Reynolds number condition, it was investigated whether the use of a turbulator would be beneficial. The reasoning behind using a turbulator is found when looking at the boundary layer around an airfoil. A laminar boundary layer induces less friction, but a turbulent boundary layer is much less prone to separate from the airfoil. Therefore, it can be beneficial to 'force' the flow to become turbulent to stay attached, at the expense of more skin friction. This can be done with a turbulator: a simple device that trips the boundary layer. Examples of turbulators are a thin wire glued to the wing surface or a zig-zag tape, which induce small vortices that make the boundary layer turbulent.

Figure E.1 shows the skin friction on the top side of the airfoil for an angle of attack of 0°. This plot is very useful in predicting separation. Separated areas show a negative friction coefficient (C_f) because of flow reversal. Separation occurs just behind the 60% mark. Placing a turbulator at 60% increases the skin friction but also prohibits separation. This same effect can also be seen in the figure E.2 which shows the pressure coefficient (C_p). In the original case, the pressure coefficient drops near 60% due to laminar separation. Around 90% the flow transitions, but this is too much aft for reattachment. In turbulent flow, the pressure does not change as much. The change in pressure gradient at 60% is caused by the transition of the boundary layer.

Now it is known that a turbulator can be beneficial, it should be decided what the most optimal location is. This is done by plotting the $C_l - C_d$ polar for the airfoil with different turbulator locations as shown in figure E.2. Too much forward does not improve the separation performance any more, but adds additional skin friction drag. This can be seen by comparing the 50% location with the 40% location. It can also be seen that a turbulator located too close to the trailing edge will be less efficient, because at higher angles of attack the flow can already separate in front of the turbulator. This can be seen in the plot for the 70% location near a C_l of 1.2. Overall, a tripped location of 60% of the chord gives the best aerodynamic performance.

It takes some distance behind the turbulator for the flow to become fully turbulent. In other words, XFOIL forces an instant transition while this in reality is a gradual process. Therefore, the turbulator will be placed 10% in front of the tripping location that is optimum according to the analysis, thus 50%. It is hard to predict the exact distance required to become fully turbulent but because a turbulent location of 70% also yields reasonable results, the proposed location is assumed to be on the safe side. The turbulator will thus be placed at 50% to ensure that the flow is turbulent at 60% of the wing chord.

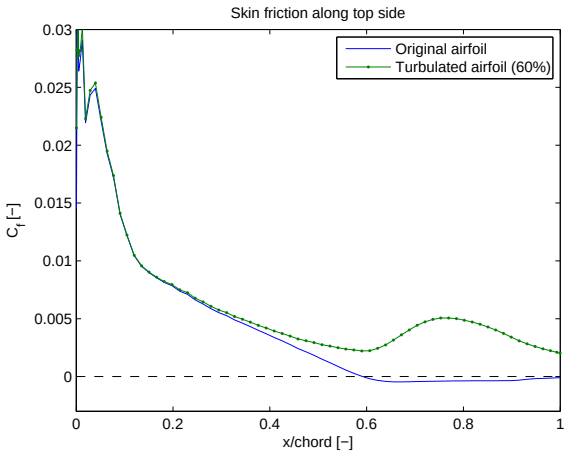

Figure E.1: Skin friction along top side

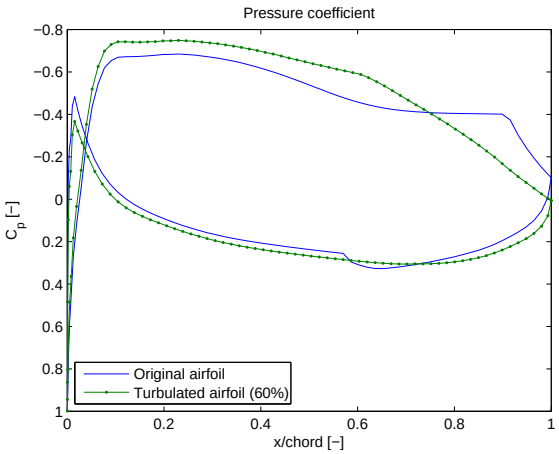

Figure E.2: Pressure coefficient

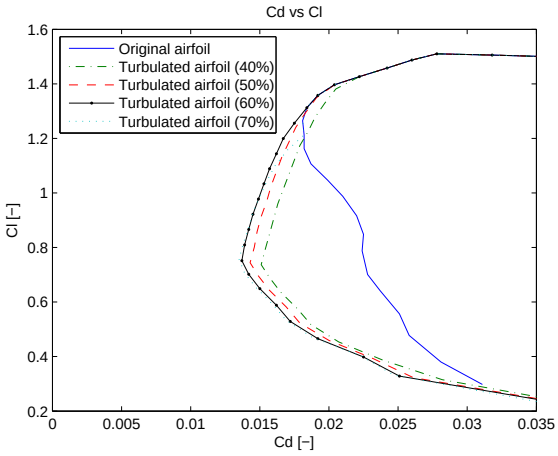

Figure E.3: Cd vs Cl

Appendix F

Propeller Model Validation

It is hard to rely on statistical data or on database programs like 'Drivecalc' for determining propeller parameters. These programs rely on data from propellers designed for completely different regimes. Furthermore, it is hard to find trends in the influence of different parameters on the performance because it is not possible to just vary one parameter. Therefore, a simulation of the propeller in Matlab was written which applies the blade element momentum theory. This analysis refers to the division in spanwise direction of the propeller geometry in small elements. For every element the program calculates the force in flight direction (thrust) and the force counteracting the rotational motion of the propeller (multiplied by the radial position of the element gives the moment contribution of this element). For the calculation of these forces, the software takes into account both the aerodynamic forces of the element (lift and drag) and the change in momentum through the propeller disk (caused by the propeller induced velocity change and swirl). C_l vs α and C_d vs α data of the used airfoil at a wide range of Reynolds numbers was obtained from XFOIL analyses. Summing all these forces over the propeller blade and multiplying with the number of propeller blades gives the total thrust provided per propeller and also the moment required to drive it.

The assumptions corresponding to this method are:

- There is no interaction between the different elements and blades
- There is no radial flow
- The propeller does not deform
- The propeller disk is perpendicular to the airflow

To find out how usable the model is, it is very important to validate it. Validation is basically comparing the numerical results with actual test data. Test data was found in NACA Report No. 640 "The Aerodynamic Characteristics of Full-Scale Propellers Having 2, 3, and 4 Blades of Clark Y and R.A.F. 6 Airfoil Sections [41]. The good thing of this report is that the complete geometry of multiple propellers is specified. That is, the chord distribution, the twist distribution, the diameter, the airfoils, and the set pitch angle. Defining this geometry in the model, allowed to compare the numerical data to actual test data. These results for a 2 bladed propeller with a diameter of 3.05 m, using a Clark Y airfoil can be seen in figure F.1.

The numerical data for the thrust produced by every blade element was multiplied with 0.95 in order to lower these values since the used method is generally overestimating the thrust and thus the overall efficiency. As can be seen in the graph, the curves of the numerical analysis and the corresponding test data are quite similar.

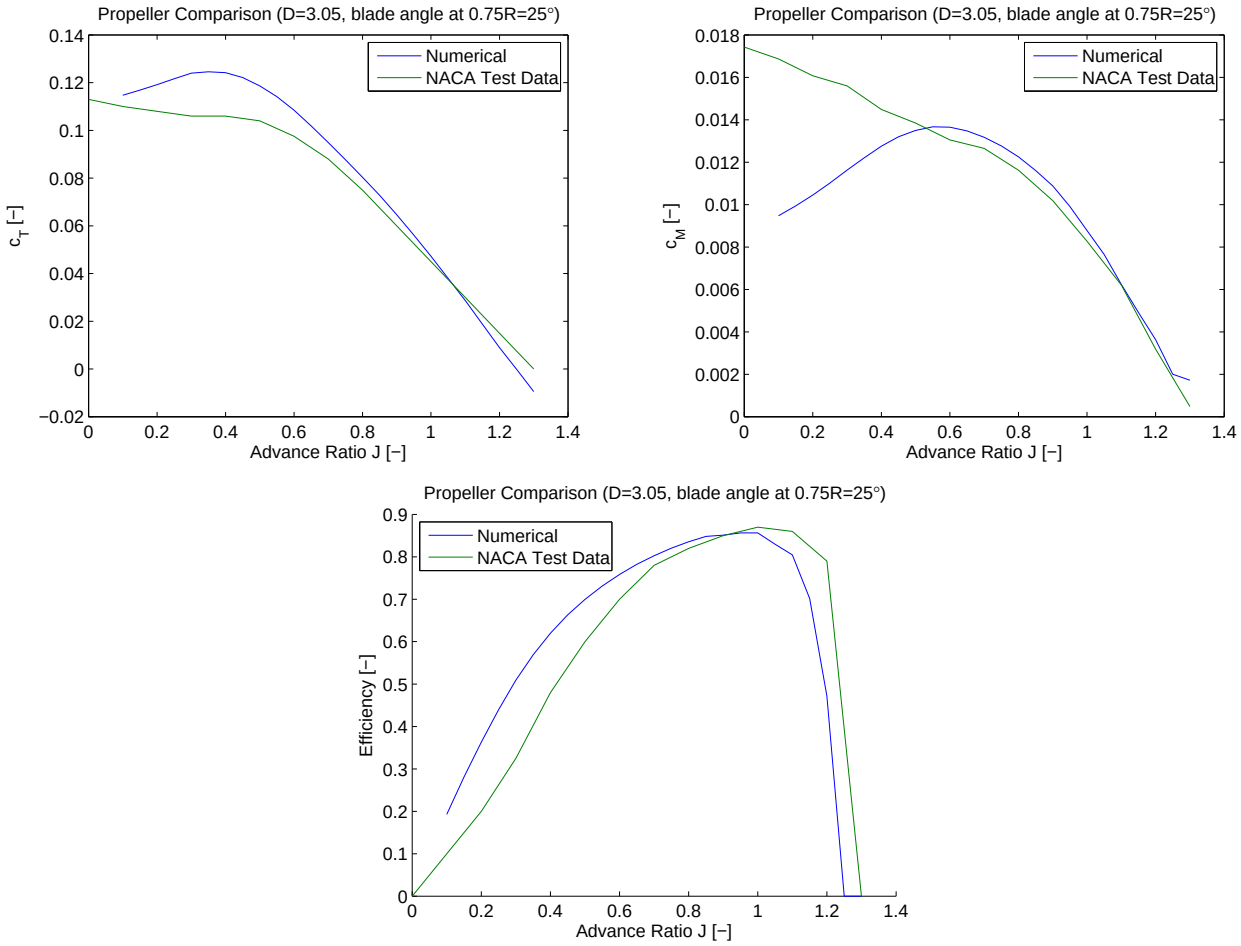

Figure F.1: Validation of the model with actual test data from the Clark Y airfoil in terms of c_T, c_m and η

Appendix G

Material Selection

This appendix provides a concise explaination of how the different materials are selected. For all parts, all materials in a large database were rated based on the criteria as explained below.

The material for the spar flanges is chosen based on its specific stiffness.

The material selection for the spar web, is based on Tresca's criteria [42]. Therefore the material strength is divided by two in order to obtain the material shear strength.

The material selection for the D-box is based on the specific shear modulus as obtained by equation G.1 [43]. The shear modulus is represented by G, Young's modulus by E and the Poisson's ratio by ν.

$$\frac{G}{\rho} = \frac{\frac{E}{2\cdot(\nu+1)}}{\rho} \tag{G.1}$$

As derived in chapter 5.4.1 the buckling performance of a material is defined by E/ρ^2. Please refer to figure G.1 to see that balsa wood has the best performance.

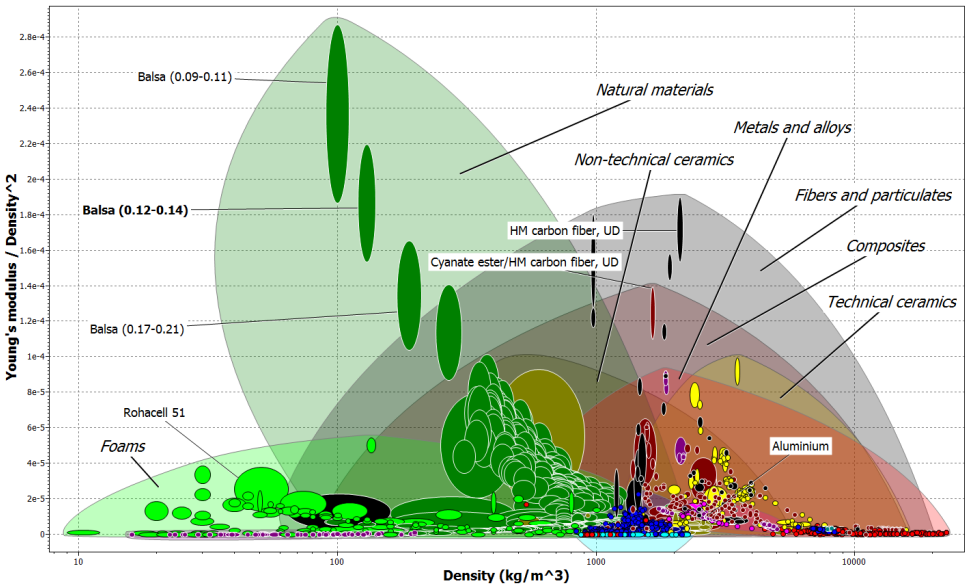

Figure G.1: Specific buckling performance versus density

Appendix H

System Engineering Flowchart

This appendix shows the flowchart as used for the system engineering process. It connects all design choices to the subsystems that are influenced.

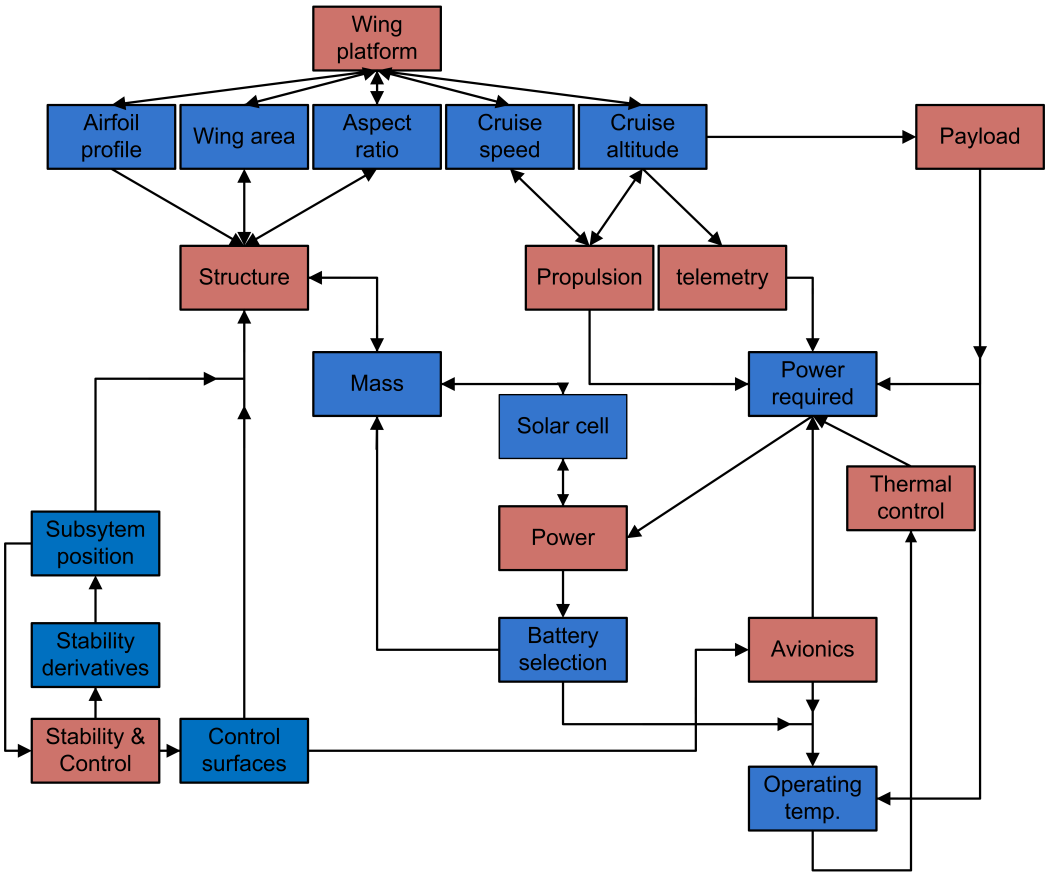

Figure H.1: Design parameters influence on subsystems

Appendix I

Communication Flow Diagrams of Subsystems

In this appendix, the communication flow diagrams of the power, the payload and the autopilot subsystem are given.

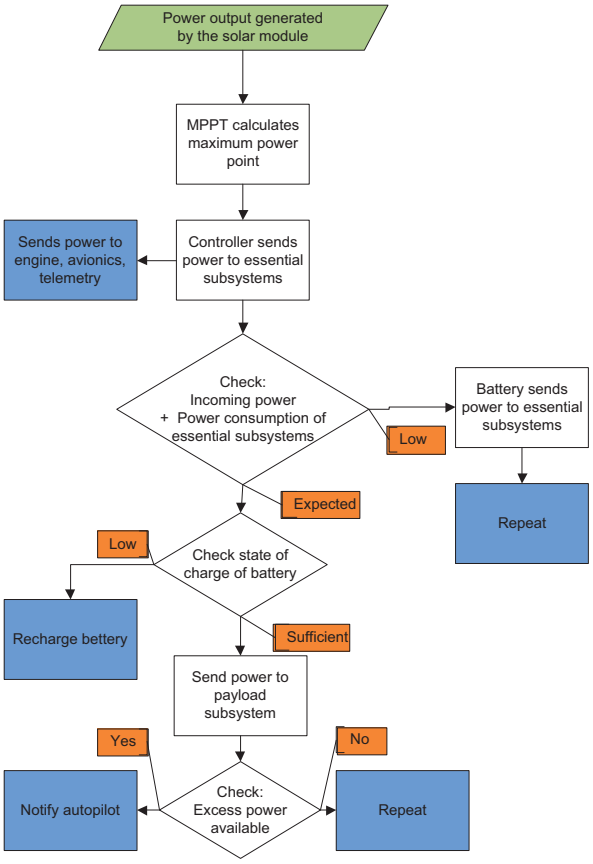

Figure I.1: Communication Flow Diagram of the Power Subsystem

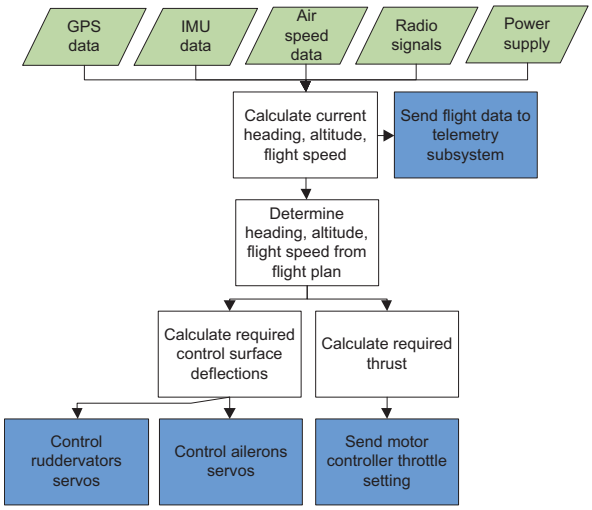

Figure I.2: Communication Flow Diagram of the Autopilot Subsystem

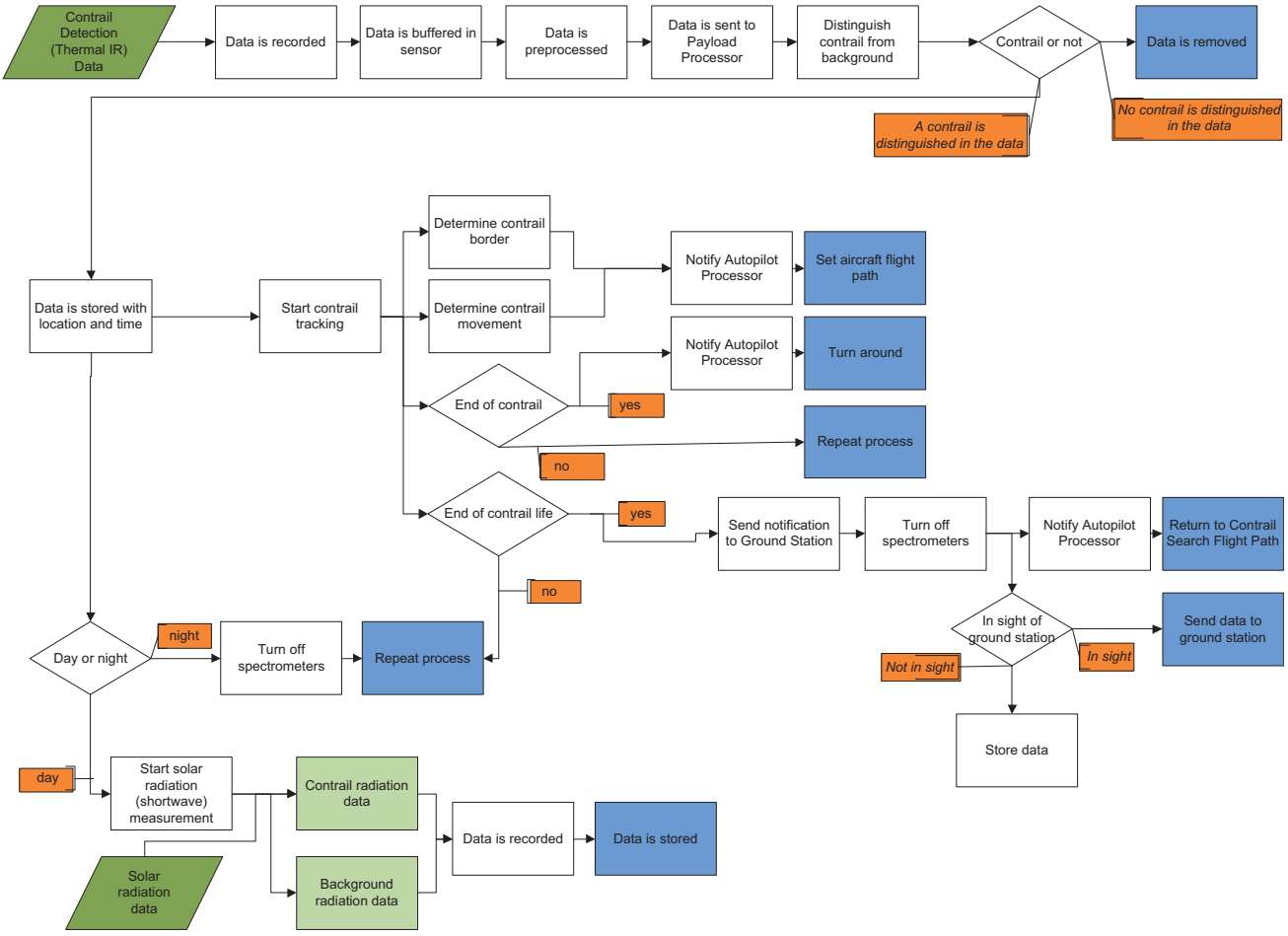

Figure I.3: Communication Flow Diagram of the Payload Subsystem

Appendix J

System Integration and Wing Layout

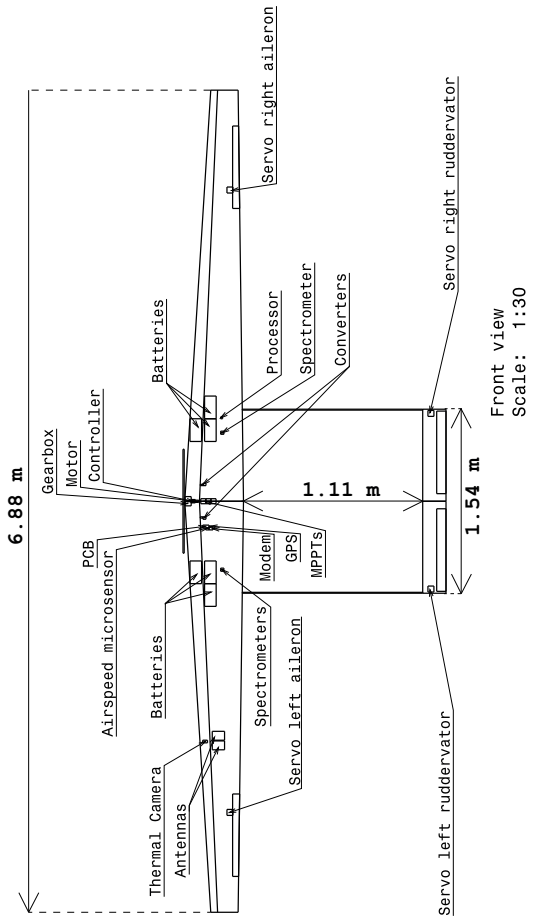

Figure J.1: Integration of subsystems and internal layout of the wing - top view

Table J.1: Centre of gravity and moments of inertia of the system

x_{cg} $[mm]$	y_{cg} $[mm]$	$I_x \cdot x$ $[kg \cdot m^3]$	$I_y \cdot y$ $[kg \cdot m^3]$	$I_z \cdot z$ $[kg \cdot m^3]$
192	-17	7.5902	0.2340	5.1270

Appendix K

Final Design Illustrations

Figure K.1 shows the final StratoMAV design.

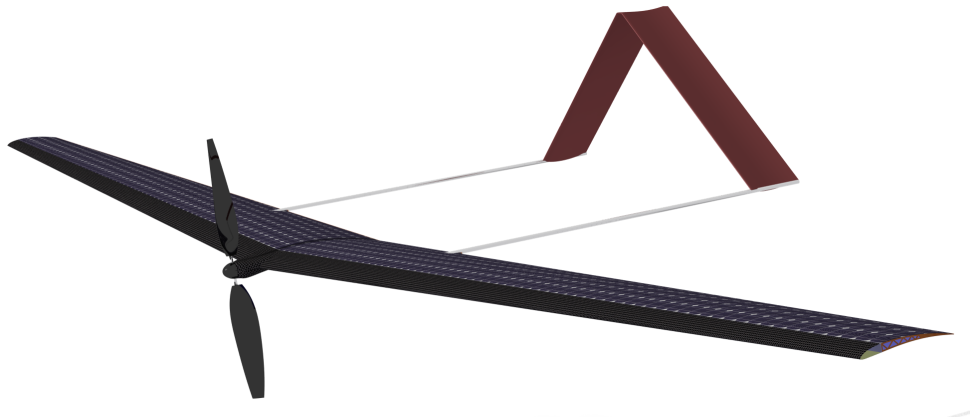

Figure K.1: Final StratoMAV design

Figure K.2 shows the final propeller design.

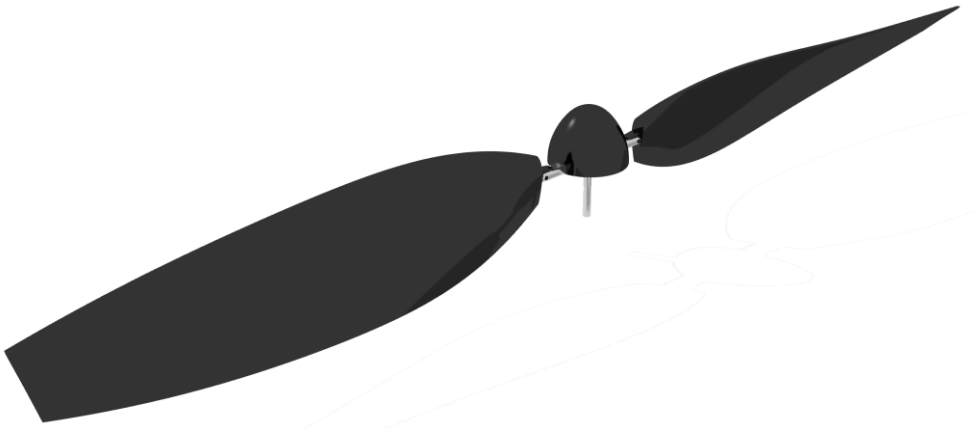

Figure K.2: Final propeller design